Dynamic optical spectroscopy and pyrometry of static targets under optical and x-ray laser heating at the European XFEL

Author(s):
Ball, Orianne; Prescher, Clemens; Appel, Karen; Baehtz, Carsten; Baron, Marzena Anna; Briggs, Richard; Cerantola, Valerio; Chantel, Julien; Chariton, Stella; Coleman, Amy L.; Cynn, Hyunchae; Damker, H.; Dattelbaum, Dana; Dresselhaus-Marais, Leora E.; Eggert, Jon H.; Ehm, Lars; Evans, William J.; Fiquet, Guillaume; Frost, Mungo; Glazyrin, Konstantin; Goncharov, Alexander F.; Husband, Rachel J.; Hwang, Huijeong; Jaisle, Nicolas; Jenei, Zsolt; Kim, J.-Y.; Lee, Yongjae; Liermann, Hanns-Peter; Mainberger, J.; Makita, Mikako; Marquardt, Hauke; McBride, Emma Elizabeth; McHardy, James; McMahon, Malcolm I.; Merkel, Sébastien; Morard, Guillaume; O'Bannon III, E.F.; Otzen, Christoph; Pace, Edward J.; Pelka, A.; Pépin, Charles M.; Pigott, Jeffrey S.; Plückthun, Christian; Prakapenka, Vitali B.; Redmer, Ronald; Speziale, Sergio; Spiekermann, Georg; Strohm, Cornelius; Sturtevant, Blake T.; Talkovski, P.; Wollenweber, Lennart; Zastrau, Ulf; Konôpková, Zuzana

Publication date:
2023-08-07

Permanent link:
https://doi.org/10.3929/ethz-b-000628458

Originally published in:
Journal of Applied Physics 134(5), https://doi.org/10.1063/5.0142196

Journal of Applied Physics ARTICLE scitation.org/journal/jap

Dynamic optical spectroscopy and pyrometry of static targets under optical and x-ray laser heating at the European XFEL

Cite as: J. Appl. Phys. **134**, 055901 (2023); doi: 10.1063/5.0142196
Submitted: 12 January 2023 · Accepted: 21 April 2023 ·
Published Online: 2 August 2023

O. B. Ball,[1] C. Prescher,[2,3] K. Appel,[4] C. Baehtz,[5] M. A. Baron,[6,7] R. Briggs,[8] V. Cerantola,[4] J. Chantel,[7] S. Chariton,[9] A. L. Coleman,[8] H. Cynn,[8] H. Damker,[2] D. Dattelbaum,[10] L. E. Dresselhaus-Marais,[8,11,12] J. H. Eggert,[8] L. Ehm,[13] W. J. Evans,[8] G. Fiquet,[6] M. Frost,[12] K. Glazyrin,[2] A. F. Goncharov,[14] R. J. Husband,[2] H. Hwang,[15,16] N. Jaisle,[17] Zs. Jenei,[8] J.-Y. Kim,[18] Y. Lee,[15] H. P. Liermann,[2] J. Mainberger,[2] M. Makita,[4] H. Marquardt,[19] E. E. McBride,[12,20] J. D. McHardy,[1] M. I. McMahon,[1] S. Merkel,[7] G. Morard,[6,17] E. F. O'Bannon III,[8] C. Otzen,[2,21] E. J. Pace,[1] A. Pelka,[5] C. M. Pépin,[22] J. S. Pigott,[10,23] C. Plückthun,[4,24] V. B. Prakapenka,[9] R. Redmer,[24] S. Speziale,[25] G. Spiekermann,[26] C. Strohm,[2] B. T. Sturtevant,[10] P. Talkovski,[2] L. Wollenweber,[4] U. Zastrau,[4] R. S. McWilliams,[1,a)] and Z. Konôpková (EuXFEL Community Proposal No. 2292)[4,a)]

AFFILIATIONS

[1]The School of Physics and Astronomy, Centre for Science at Extreme Conditions, and SUPA, University of Edinburgh, Peter Guthrie Tait Road, Edinburgh EH9 3FD, United Kingdom
[2]Deutsches Elektronen-Synchrotron DESY, Notkestr. 85, 22607 Hamburg, Germany
[3]Institute of Earth and Environmental Sciences - Geomaterials and Crystalline Materials, Albert-Ludwigs Universität Freiburg, Hermann-Herder Str. 5, 79104 Freiburg, Germany
[4]European XFEL GmbH, Holzkoppel 4, 22869 Schenefeld, Germany
[5]Institute of Radiation Physics, Helmholtz-Zentrum Dresden-Rossendorf, Bautzner Landstraße 400, 01328 Dresden, Germany
[6]Inst. Minéralogie, de Physique des Matériaux et de Cosmochimie (IMPMC), Sorbonne Université, UMR CNRS 7590, Museum National d'Histoire Naturelle, 4 Place Jussieu, Paris, France
[7]Univ. Lille, CNRS, INRAE, Centrale Lille, UMR 8207 - UMET - Unité Matériaux et Transformations, F-59000 Lille, France
[8]Lawrence Livermore National Laboratory, 7000 East Avenue, Livermore, California 94550, USA
[9]Center for Advanced Radiation Sources, University of Chicago, Chicago, Illinois 60637, USA
[10]Los Alamos National Laboratory, Los Alamos, New Mexico 87545, USA
[11]Department of Materials Science & Engineering, Stanford University, Stanford, California 94305, USA
[12]SLAC National Accelerator Laboratory, 2575 Sand Hill Road, Menlo Park, California 94025, USA
[13]Mineral Physics Institute, Stony Brook University, Stony Brook, New York 11794, USA
[14]Carnegie Science, Earth and Planets Laboratory, 5241 Broad Branch Road, NW, Washington, DC 20015, USA
[15]Earth System Sciences, Yonsei University, 50 Yonsei-ro, Seodaemun-gu, Seoul 03722, Republic of Korea
[16]School of Earth Sciences and Environmental Engineering, Gwangju Institute of Science and Technology, 123 Cheomdan-Gwagiro, Gwangju 61005, Republic of Korea
[17]Université Grenoble Alpes, Université Savoie Mont Blanc, CNRS, IRD, IFSTTAR, ISTerre, 38000 Grenoble, France
[18]Department of Physics, Research Institute for High Pressure, Hanyang University, 222 Wangsimni-ro, Seoul 04763, Republic of Korea
[19]Department of Earth Sciences, University of Oxford, South Parks Road, OX1 3AN Oxford, United Kingdom
[20]School of Mathematics and Physics, Queen's University Belfast, University Road, Belfast BT7 1NN, United Kingdom
[21]Institute of Geosciences, Friedrich Schiller University Jena, Carl-Zeiss-Promenade 10, 07745 Jena, Germany

[22]CEA, DAM, DIF, F-91297 Arpajon, France and Université Paris-Saclay, CEA, Laboratoire Matière en Conditions Extrêmes, 91680 Bruyères-le-Châtel, France
[23]School of Engineering, Case Western Reserve University, 10900 Euclid Ave, Cleveland, Ohio 44106, USA
[24]Institut für Physik, Universität Rostock, D-18051 Rostock, Germany
[25]GFZ German Research Centre for Geosciences, Telegrafenberg, 14473 Potsdam, Germany
[26]ETH Zürich, Rämistrasse 101, 8092 Zürich, Switzerland

[a)]**Authors to whom correspondence should be addressed:** rs.mcwilliams@ed.ac.uk and zuzana.konopkova@xfel.eu

ABSTRACT

Experiments accessing extreme conditions at x-ray free electron lasers (XFELs) involve rapidly evolving conditions of temperature. Here, we report time-resolved, direct measurements of temperature using spectral streaked optical pyrometry of x-ray and optical laser-heated states at the High Energy Density instrument of the European XFEL. This collection of typical experiments, coupled with numerical models, outlines the reliability, precision, and meaning of time dependent temperature measurements using optical emission at XFEL sources. Dynamic temperatures above 1500 K are measured continuously from spectrally- and temporally-resolved thermal emission at 450–850 nm, with time resolution down to 10–100 ns for 1–200 μs streak camera windows, using single shot and integrated modes. Targets include zero-pressure foils free-standing in air and *in vacuo*, and high-pressure samples compressed in diamond anvil cell multi-layer targets. Radiation sources used are 20-fs hard x-ray laser pulses at 17.8 keV, in single pulses or 2.26 MHz pulse trains of up to 30 pulses, and 250-ns infrared laser single pulses. A range of further possibilities for optical measurements of visible light in x-ray laser experiments using streak optical spectroscopy are also explored, including for the study of x-ray induced optical fluorescence, which often appears as background in thermal radiation measurements. We establish several scenarios where combined emissions from multiple sources are observed and discuss their interpretation. Challenges posed by using x-ray lasers as non-invasive probes of the sample state are addressed.

 https://doi.org/10.1063/5.0142196

I. INTRODUCTION

The study of warm dense matter (WDM) and high pressure-temperature states of condensed matter is vital to understanding complex physical systems that exist in nature, such as planetary interiors,[1,2] and in technologies, such as internal confinement fusion.[3] The description of WDM is also a challenge for theory because strong correlations and quantum effects have to be treated consistently beyond perturbative methods by using, e.g., *ab initio* simulations.[4–6]

Laboratory experiments are, therefore, central to characterizing WDM behavior. The creation of high pressure (millions of atmospheres) and temperature (thousands of degrees Kelvin or higher) conditions are required to study these fundamental systems.[7–16] Traditionally, these are created through intense irradiation,[17–21] dynamic shock compression,[22–25] or a combination of static compression with these techniques, often using a diamond anvil pressure cell (DAC).[7–16,26] However, these techniques are often constrained by short experimental lifetimes due to loss of high-density conditions. Damage to samples can also occur over longer periods through sample contamination from chemical reactions with surrounding material (e.g., diamond anvils) or cumulative thermal or mechanical damage. This can then lead to discrepancies between various experimental results.[9,14,27–29] At the boundary between traditionally fast and slow measurements, a variety of experiments are possible which address common challenges of WDM experiments; however, novel measurement techniques and diagnostics are often needed for such regimes.[11,13,30]

X-ray Free Electron Lasers (XFELs) present a new frontier for intermediate timescale extreme conditions studies. Excited states following femtosecond pulsed irradiation can persist for beyond microsecond timescales on XFELs, for example, due to volumetric heating of massive objects.[31] Meanwhile, pulse repetition rates in the MHz range, such as that currently available at the European X-ray Free Electron Laser (EuXFEL),[32,33] offer opportunities for serial probing and excitation on similar, microsecond timescales.

Controlling samples subjected to WDM extremes over such experimental lifetimes as well as defining the pressure-density conditions reached is made possible using DACs to contain and pressurize samples of interest.[31] This configuration is ideal to study WDM as it is possible to use pulsed x-ray heating to heat targets to tens of thousands of Kelvin.[29,31,34–37] In this scenario, hard x-ray energies greater than 10 keV have long absorption lengths (~millimeters) for light elements (i.e., carbon), allowing penetration of millimeter thick diamonds, while absorption lengths in the micrometer range for high atomic number elements enable localized energy deposition within micrometer thick samples. XFELs are ideally suited to this type of experiment because they are able to produce short (femtosecond pulse length), high-power ($\sim 10^{12}$ photons per pulse), hard x-ray (>10 keV) pulses. These pulses also provide a fast and high power probe to observe the sample conditions[29,37–39] and are often available in a pair or train. This, therefore, naturally leads to the ability to perform serial pump–probe experiments.[17,40]

A number of diagnostics can be employed to measure the conditions in such experiments, including temperature, many using the pulsed x-ray source itself. If the pump is also an x-ray pulse, the pump and probe are automatically spatially aligned, which is ideal for sampling the heated volume. X-ray diffraction (XRD)[18] can determine sample conditions through measurements of sample volume and phase transformations, but is complicated by the difficulty in discriminating between the effects of pressure and temperature changes. Likewise, x-ray Thomson scattering, often used in conjunction with x-ray heating, can estimate electron temperature via detailed balance in the collective scattering regime inspecting the height of the up- and down-shifted plasmons,[41] with temperature uncertainties often on the order of a few eV,[41–46] but requires high quality information on the source and instrument function.[46] Such x-ray snapshots of temperature can be further limited when observing continuously changing sample conditions, e.g., due to insufficient time sampling.[29]

An ideal temperature diagnostic will continuously determine sample temperature through a period of interest with high time resolution and small uncertainty independent of assumptions and the detailed sample conditions. Pyrometry provides such a method, inferring sample temperature from optical emission released from heated samples. As opposed to active x-ray probing, pyrometry is passive so can inherently provide a continuous record of temperature. Pyrometric measurements have long been used to estimate the temperature reached in static compression (i.e., laser-heated diamond anvil cell, LHDAC),[7–16,47] shock compression,[22–25] and fast radiative (i.e., isochoric) heating studies,[48,49] though while proposed[35] its application to XFEL heating has not been demonstrated. Pyrometry determines temperatures reached[12] usually by the sole assumption that emission follows the behavior of a gray-body radiator, as defined by Planck's law.[22,50]

Streaked optical pyrometry (SOP) provides one method to measure *in situ* sample temperatures with high time resolution in the picosecond to microsecond range. Streak camera images record emission over a pre-determined time window denoted the streak window. Changes in emission brightness as a function of time are recorded on the image as changes in intensity along the time axis.[51,52] The spatial, spectral, and temporal shape of optical emission from any heated sample is difficult to obtain simultaneously,[22] thus the orthogonal axis of the streak image will resolve the emission either spatially or spectrally (i.e., a linear position vs time broadband intensity map, or a wavelength vs time spectrogram from a particular position). Each approach has advantages that depend on the sample properties, temperature range, target design, spatial scale of the event, and other factors. For example, the presence of optical windows in targets, such as those used when observing statically compressed samples or a shocked interface, adds complications such as the requirement that any optical emission pass through layers of other material, potentially affecting the final collected emission.[53,54] In many cases, the use of spectrally (as opposed to spatially) resolved detection is advantageous as it is less sensitive to emissivity, target transmission, other complex optical properties of targets, temperature inhomogeneity, or time dependence of these factors, within certain limits.[55,56] The measured spectral shape also allows an independent verification that emission adheres to the predictions of the Planck model and thus provides a final test of whether the measured temperature can be valid, by resolving obvious distortions in thermal emission or nonthermal contributions to signal. For these reasons, spectrally resolved temperature determination is generally considered more reliable in complex sample environments, such as those using tight focused radiative heating similar to the x-ray and optical heating employed in this study (e.g., in traditional laser heated DAC experiments).

The detection limit of SOP is predicated on the temperature, sweep window, number of events (shots) integrated, size of heated and observed areas, event duration, sample optical characteristics, spectral range detected, and spectrometer dispersion, and varies significantly depending on these factors for different applications. Lower detection limits for SOP fall in the range of 400–4000 K in typical single shot applications[11,48,51,57,58] and is observed to be 1500–3000 K for the system described here. Fundamentally, this is limited by the rapid reduction in emission with decreasing temperature (i.e., the Stefan–Boltzmann law). While there is no upper limit on detectable temperature, spectral form becomes insensitive to the temperature where the Planck distribution peaks well below the observed wavelength band (i.e., Wien's law), which occurs, e.g., in the electron volt range for visible diagnostics; in such cases, absolute emission intensity would be a reliable—and possibly superior—indicator of temperature in certain circumstances.[51]

Here, we report the design and performance of an SOP diagnostic implemented at the High Energy Density (HED) instrument of the EuXFEL. The system measures optical signals in the visible spectral range, in spectral-temporal space and can be deployed in a range of sample environments and extreme conditions scenarios. A selection of common applications are evaluated here. The diagnostic was specifically designed and tested to work in conjunction with DAC static compression techniques. The equipment for the system was provided to the HED instrument by the HIBEF user consortium, and the design and implementation was performed in collaboration between EuXFEL, Deutsches Elektronen-Synchrotron (DESY), and University of Edinburgh. Basic design parameters are discussed in Sec. II, the experimental procedure in Sec. III, samples in Sec. IV, and results in Sec. V. The system was developed at DESY, with first experiments using laser heating only (Sec. V A). It was moved to EuXFEL for the first online measurements with x-rays only, in association with the first User Community Assisted Commissioning Experiment, Proposal No. 2292[38,39,59] (Secs. V B–V F). Laser heating and x-ray heating together were subsequently performed in further commissioning work in Proposal No. 2731 (Secs. V G and V H). Numerical modeling of experiments and comparison to the measurements are included in Sec. VI, while a discussion of the findings and conclusions for future work using the diagnostic are given in Sec. VII.

II. EXPERIMENT SETUP

A. Sources

European XFEL offers three self-amplified spontaneous emission (SASE1, SASE2, SASE3) sections that produce x-ray photons at

wavelengths varying from 0.1 to 1.6 nm. The HED experimental hutch is located at the end of the SASE2, which produces photons in the hard x-ray regime between 0.1 and 0.25 nm.[60] X-ray pulses are grouped into trains of up to 2700 pulses, with a train repetition rate of 10 Hz and intra-train pulse repetition rate of fractions of 4.5 MHz, giving pulse separation of 221.5 ns (or 443, 886, etc.). Pulse intensity monitors are placed upstream and downstream of the experimental vacuum chamber (Interaction Chamber 2, IC2) in order to measure beam intensity and pulse-to-pulse fluctuations in intensity.[39] Energy on target was ~30% of the measured upstream beam intensity on the absolutely-calibrated x-ray intensity gas monitor (XGM) in the SASE2 beamline (SASE XGM),[39,61,62] and could be further reduced through user selected attenuation of the beam. Downstream energy intensity monitors are placed in the beamstop after the experimental chamber (Fig. 1). The XFEL heating (XH) due to individual pulses and pulse trains are examined here. The XFEL beam is focused onto the target using several sets of on-axis chromatic compound refractive lenses (CRLs), with spot sizes in the range of 5–20 μm (FWHM) on target used in the described experiments (Table I).

Single or double-sided pulsed or continuous optical heating (LH) of targets is made possible using a near-infrared (NIR) laser (Model SP-100P-A_EP_Z, 1070 nm, 1.2 eV) which was integrated with the SOP optical system [Figs. 1(b) and 2(c)]. The NIR laser has a repetition rate of up to 1 MHz, standard pulse lengths ranging from 20 to 420 ns, and a collimated beam diameter of 10 mm. Focusing creates a spot size on the sample of 11 × 14 μm (FWHM). Some laser waveforms possible are shown in Fig. 3. The maximum pulse energy is 1 mJ (depending on the waveform and repetition rate), and peak power of 10 kW. Incident laser power is attenuated from 100% to 0% by a combination of polarizing beam splitting cubes and rotating quartz waveplates in the laser beam path [Fig. 1(b)]. The upstream and downstream laser powers are controlled separately.

B. Optical configuration

The SOP experiments at the HED instrument are designed to take place in IC2. Figures 1 and 2 show the optical configuration used during these experiments. Further details about the experimental setup of IC2 can be found in Refs. 39 and 63–66.

Optical access to the sample is possible from both upstream and downstream sides, relative to the XFEL beampath (see Sec. II A). The near-sample optics consist of turning mirrors at 45 degrees relative to the XFEL beam, and objectives (AdlOptica geoHEAT-60-NIR) with 60 mm focal length focusing through the mirrors onto the sample plane. The mirror-objective system can be retracted when not in use in order to completely clear the x-ray beampath. The optical beampaths are guided through the chamber window to the custom-built exterior optical table [Fig. 1(b)] where the rest of the optical components are placed.

The upstream turning mirror was initially a dielectric coated glass mirror (Semrock MGP01-650-1300) with a 300 μm diameter hole drilled in the center to allow the x-ray beam to pass through. The downstream turning mirror was a custom-made glassy carbon plate coated with Ag. Both the upstream and downstream mirrors were later replaced by 1 mm thick Ag-coated silica glass mirrors

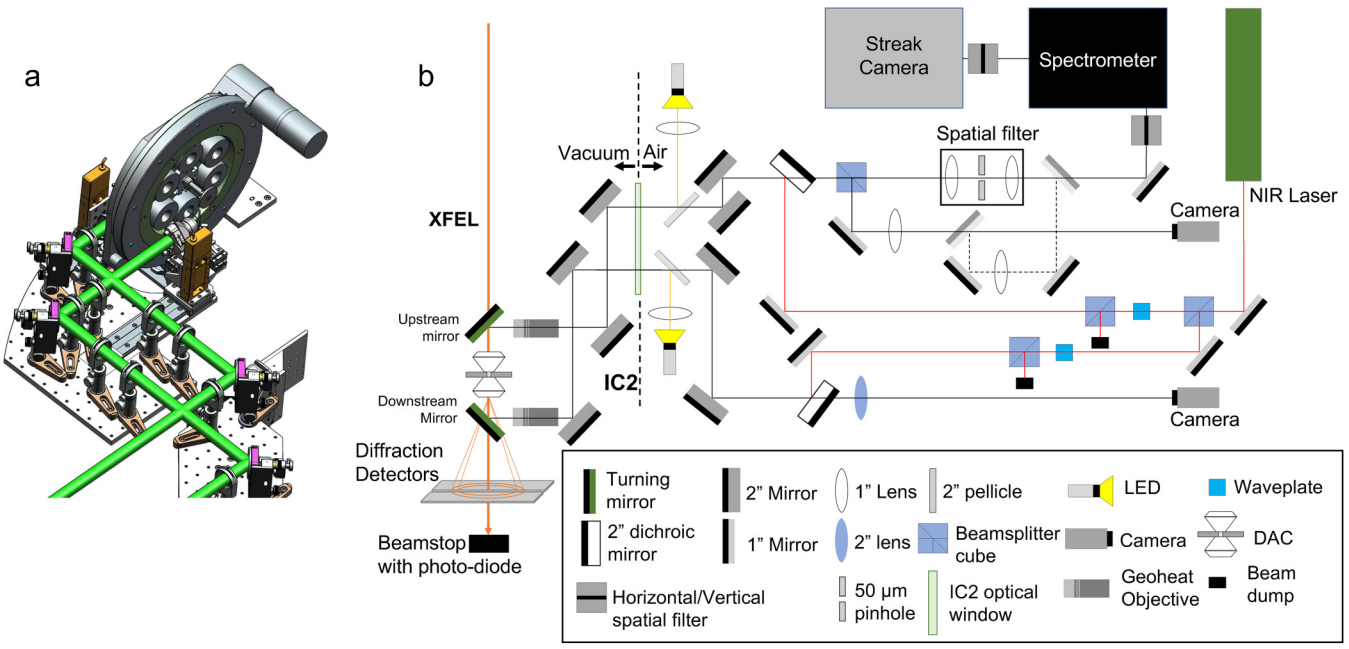

FIG. 1. Schematic of the optical system at the HED instrument for standard DAC experiments. (a) Layout of the immediate area surrounding the sample environment inside IC2. Upstream and downstream optical beam paths are shown in green. (b) Schematic of optics table layout showing the upstream and downstream optical paths from the sample inside IC2 to either a microscope or the spectrometer and streak camera (black lines). NIR laser heating pathway is shown in red lines.

TABLE I. XFEL parameters used during the experiments discussed here.

	XFEL beam parameters					
Experiment	XFEL beam energy (keV)	XFEL Energy per pulse (uJ)	Spot size (FWHM) (μm)	Number of pulses	Intra-train repetition rate	NIR laser
1						ON
2	17.8	21–240	10–20	1–20	1.13–2.26 MHz	OFF
3	17.8	15–63	5.0	10–30	2.26 MHz	ON

(from AHF) with holes drilled for x-ray direct beam transmission. The hole diameter is 1 mm downstream and 300 μm upstream.

The downstream and upstream optical paths each include microscopic imaging of samples (with recording), illumination of the sample, and heating with the NIR laser. Optical emission for pyrometry is acquired from the upstream side of the sample, by passing light through to the spectrometer and steak camera system. Online microscopy is achieved using long focal length lenses (f = 750 mm upstream, f = 1000 mm downstream) to image onto Basler CCD cameras, to provide sample viewing and alignment at high image magnification. Illumination from both sides of the sample is achieved by inserting pellicle beamsplitters in front of the viewport chamber window on the optical paths to deliver a red LED light source to the sample. Alignments are made using direct imaging of the NIR laser at low laser power and localized effects of x-ray irradiation, including target fluorescence or damage imprinting.

The optical path of the pyrometric signal includes an optional spatial filter consisting of a 50 μm diameter pinhole and two 60 mm focal length lenses (~1 : 1 magnification) designed to exclude non-sample emissions and other background light (such as x-ray fluorescence from diamonds above and below the focal plane in DAC targets). The light is focused onto the spectrograph entrance slit by a f = 150 mm lens for an effective magnification of ~2.5. The numerical aperture is ~0.16 at the imaging objective and spatial filter segments, and less at the spectrometer. Additional details on the optical configuration of the SOP can be found in Refs. 11, 47, and 67.

C. Detector configuration

In order to acquire time- and spectrally-resolved information on the emitted light, an optical spectrometer (IsoPlane 160, Princeton Instruments) is coupled to the front slit of the streak camera. The vertical slit of the spectrograph restricts input emission in the spectral direction. The spectrometer has a 203 mm focal length and f/3.88 aperture ratio.

The streak camera is a Hamamatsu with S-20 photocathode (model C13410-01A) with spectral response in the region of 200–850 nm and a horizontal slit which restricts the input emission in the time axis direction, affecting the time resolution and point spread function (PSF). The microchannel plate (MCP) intensifier gain of the streak camera can be varied from 0 to 60. The gain corresponds to varying the voltage on the MCP electrodes; higher gain increases the signal and also the noise. The sweep windows for the streak camera range between 0.5 ns and 1 ms. The streak tube is coupled to an ORCA-Flash 4.0 V2 Digital CMOS camera with 1344 (wavelength) × 1016 (time) pixels in the working area and 6.5 μm pixel size; sometimes, this is binned 2 × 2, i.e., 672 × 508 pixels to improve data handling. The readout speed of the camera is >100 frames/s. Two different collection modes, enclosing trigger and sequential mode, are used. In sequential mode, exposure to the CMOS only occurs during a single sweep regardless of how many events are incident, meaning that the visible signal from the interaction of each NIR or XFEL pulse is recorded on the final spectrogram, separated in the time domain by their intrinsic pulse separation (see Sec. II A). In most cases, the experimental data is taken using this mode. For data collected in the enclosing trigger

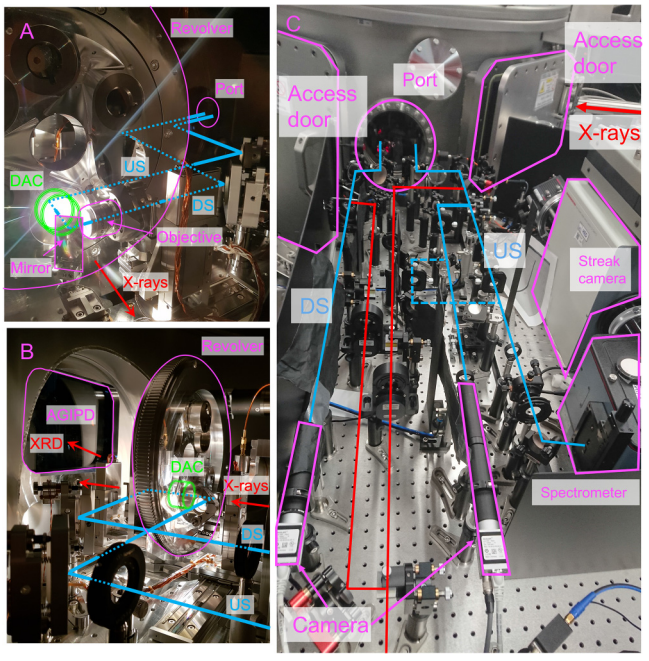

FIG. 2. Photographs showing the optical setup inside IC2 and on the adjoining optical bench. (a) Sample stage inside IC2, including six-chamber sample revolver, viewed from the downstream. (b) Sample stage inside IC2, viewed from the upstream. (c) Optics table layout showing the upstream and downstream optical paths to microscopy cameras and the spectrometer and streak camera. Upstream (US) and downstream (DS) optical paths are shown in blue, and the laser heating pathway is shown in red. Key experimental components are highlighted in pink. The AGIPD (adaptive gain integrating pixel detector) is used for time resolved x-ray diffraction (XRD) measurements.[39]

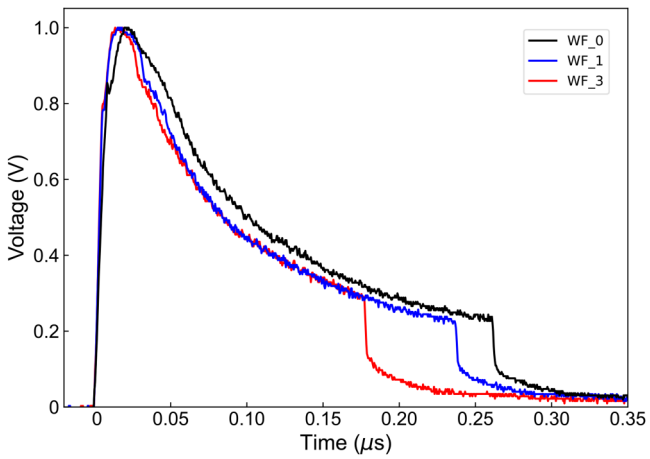

FIG. 3. Example of measured pulse waveforms for the NIR pump laser (in this study, we make use of WF_0). Y-axis indicates normalized oscilloscope voltage.

mode, the spectrogram shows emission that has been integrated over many sweeps at a repetition rate of up to 1 kHz, with varying total integration time. Thereby, increasing integration time increases the number of exposures that are accumulated per spectrogram image, each sweep acquiring a (presumably identical) repeating event (i.e., heating cycle). This mode is compatible with accumulation over EuXFEL pulse trains repeating at 10 Hz. Figure 4 shows schematically how the two different collection schemes differ.

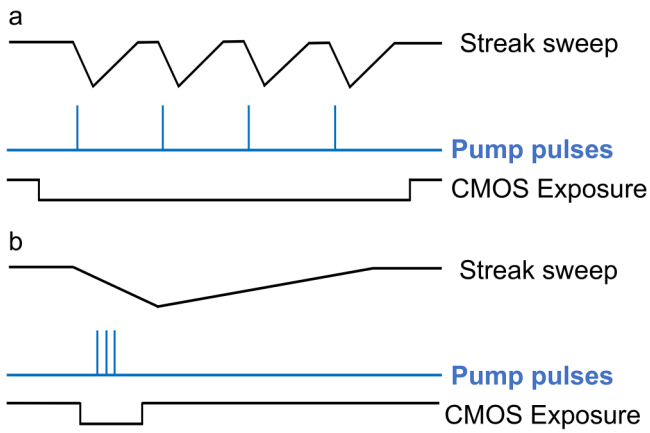

FIG. 4. Schematic of relevant timings of the streak camera and pump pulses. Pump pulses can be either from a laser heating system or XFEL pulses. Streak sweep denotes the voltage applied to the electrode in the streak camera, where time is proportional to the applied voltage; pump pulse denotes the timings of the radiation pulses incident on the sample; CMOS exposure denotes the streak camera detector integration time. (a) Series of pulses are integrated into the enclosing trigger mode, one pulse per sweep. (b) Series of pulses captured in the same streak window in the sequential mode, three pulses in a single sweep.

The wavelength axis of spectrograms is calibrated to the emission from a Ne calibration lamp resulting in a 451–955 nm observable wavelength range in this experiment. The optical response of the SOP system is a combination of the quantum efficiency of the S20 photo-cathode, the reflectivity of the turning mirrors, and the accumulated behavior of other optics (Fig. 5, see Sec. II G). The transmission function $F(\lambda)$ is experimentally measured by imaging a W calibration lamp with a known gray-body Planck distribution and comparing the intensity, as a function of wavelength and time, to the theoretical Planck distribution for the temperature at which the lamp is operating. Figure 5(a) shows that between 575 and 775 nm, the experimentally measured transmission closely agrees with the spectra predicted from the two main optical elements

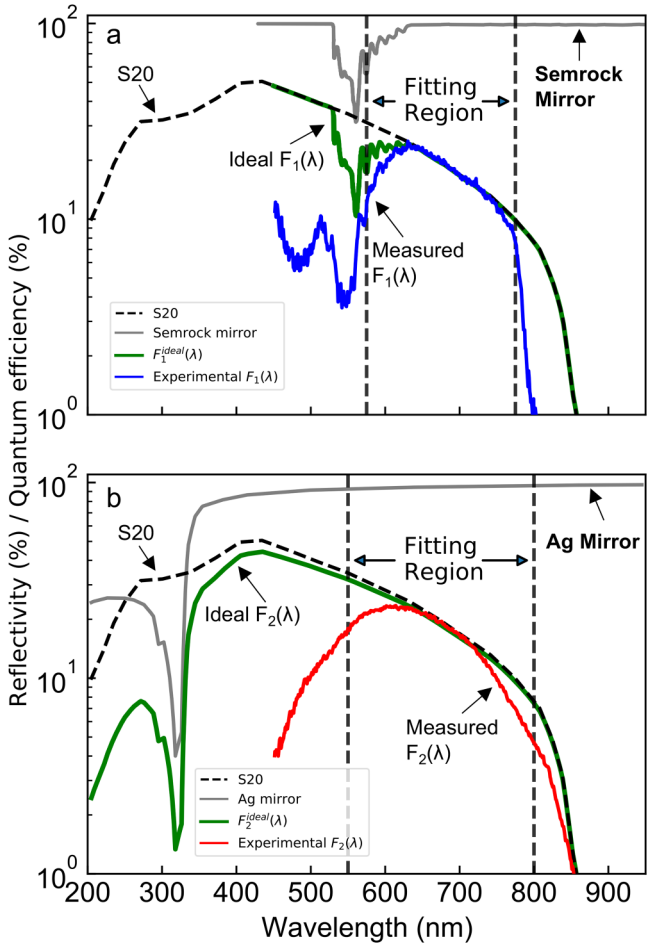

FIG. 5. SOP spectral response when using the initial dielectric (a) and final Ag (b) upstream turning mirrors. Measured time-averaged spectral transmission functions, based on calibration lamp data, are $F_1(\lambda)$, blue, and $F_2(\lambda)$, red, respectively. Expected response is green, with the published reflectivity of the turning mirror, gray, and the quantum efficiency of the S20 photocathode,[69] dashed black. The wavelength region used to determine sample temperature is shown as two vertical dashed lines. The measured transmission function is scaled to agree with the expected transmission function.

discussed above. Most spectral dips and oscillations in this transmission function were later eliminated by replacement of the dielectric turning mirror with the Ag-coated mirror,[68] also enabling a somewhat broader spectral band for detection [Fig. 5(b)].

The combination of horizontal and vertical slits in the streak spectrometer, located at the imaging planes of the sample, also function as vertical and horizontal spatial filters, respectively, and ensure good time and spectral resolution for spatially extended emission sources. Here, we report both slitted and slitless operation, the latter case being required during early EuXFEL experiments where x-ray beam pointing drift and instability precluded reliable alignment to the slits, with the small emitting area on the samples, imaged to the detector, functioning as a point source in the time and space directions, with sufficient (but reduced) temporal and spectral resolution.

An example of the streak camera acquisition of optical light emitted from the W calibration lamp, designed to be a thermal gray-body source at a set temperature, is illustrated in Fig. 6. The horizontal axis represents time (here a 5 μs sweep window), and the vertical axis contains spectral information covering 451–955 nm. Poor optical sensitivity in the intensity measurement at the edges of the spectrogram are observed, so we restrict the wavelength range when fitting temperatures to 575–775 nm. All reference lamp calibrations were obtained with slits and spatial filtering in place, in order to probe the precise optical path from the sample in the respective transmission function.

From spectral features present in the calibration spectrograms, datasets with distinct event timings, and data on spectrally distinct light sources (i.e., laser or LED), some warping of streak images is observed, dependent on the streak window; that is, shear distortions with respect to the wavelength and time axes are identified. We compensate for this warping by applying a shear distortion to both wavelength and time axes unique to each sweep window. The magnitude of the shear, per pixel, in each direction, dependent on the streak window used, is given in Table II.

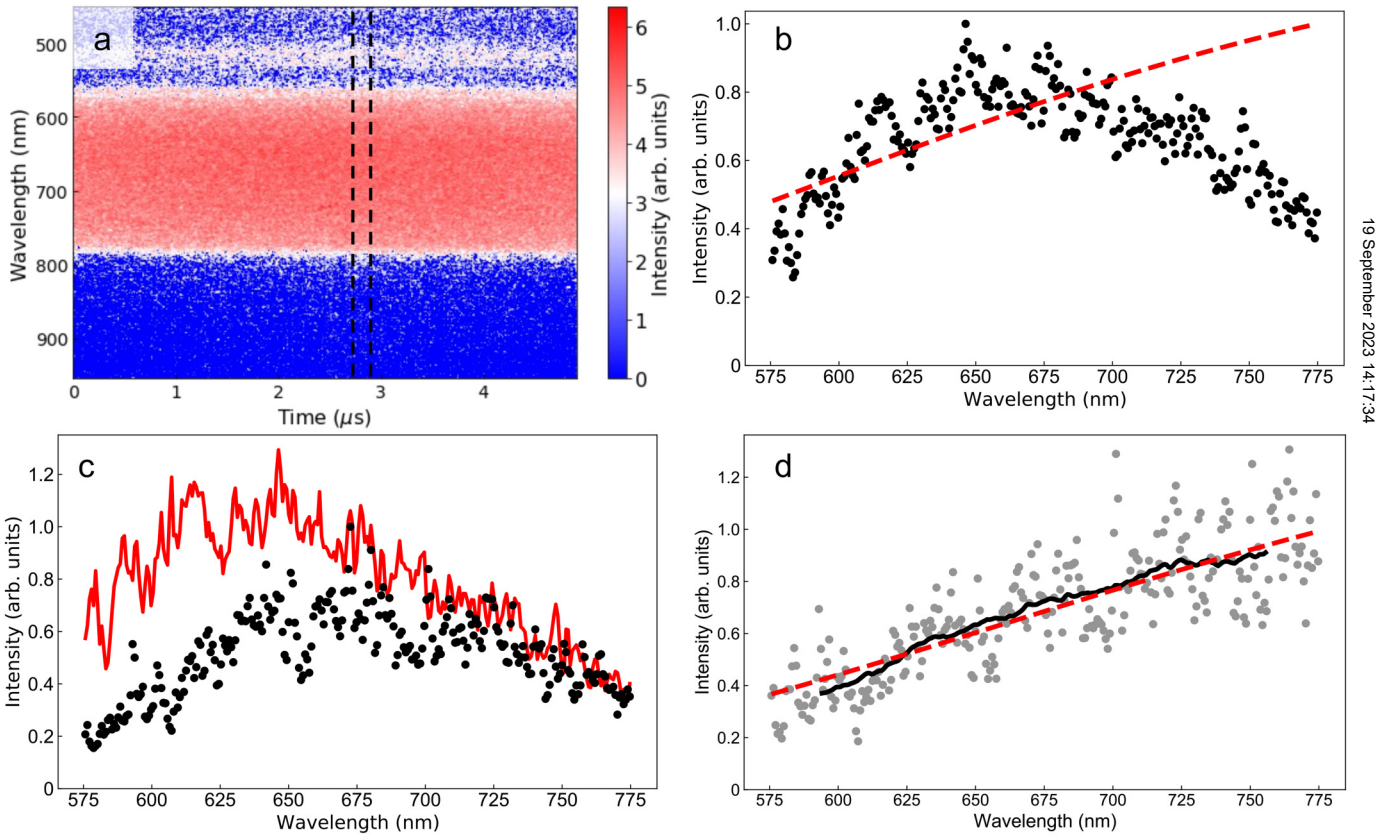

FIG. 6. Optical emission collected from the calibration lamp at 2500 and 2900 K. (a) Spectrogram of optical emission collected from a calibration lamp at 2900 K using a 5 μs streak window, taken using enclosing trigger with a sweep repetition rate of 1 kHz and exposure time of 1 s. Region corresponding to 193 ns section binned at 2.8 μs is shown between two dashed lines. (b) Binned optical emission at time = 2.8 μs of calibration lamp at 2900 K (black markers) and expected optical emission of thermal radiation at 2900 K based on Planck's distribution (red dashed line). (c) Binned optical emission at time = 2.8 μs of calibration lamp at 2500 K, black markers, and transmission function of full optical path at the same time (red solid line) derived from (b). (d) Corrected optical emission of calibration lamp at 2500 K, gray markers, at time = 2.8 μs, with moving average intensity with respect to wavelength shown as a solid black line. The fitted Planck distribution (red dashed) to the corrected emission data at T = 2591 $\pm$ 50 K is also plotted.

TABLE II. Streak window (SW) dependent corrections applied to SOP images. The streak window durations given by factory settings compared to measured streak windows from fluorescence emission are shown. The magnitude of the time and wavelength shear (pixel shift per orthogonal pixel step) applied to images, when using the 1 × 1 un-binned image size, is also given.

Streak window			Shear	
Setting	Factory measured	XFEL measured	Time	Wavelength
1	0.994	…	1/65	1/80
5	4.90	4.73	1/65	1/80
10	9.76	9.27	1/65	1/80
20	19.60	18.57	1/80	1/80
50	49.0	45.64	1/80	1/80
100	97.4	…	1/20	1/80
200	200	…	1/10	1/80

Collected spectrograms are also expected to exhibit "pincushion" flat-field sensitivity variation in both axes, on the order of 10% sensitivity. This is corrected for by calibrating the experimental emission data locally (in time and wavelength) to a spectrogram of a calibration lamp at a set temperature (e.g., Fig. 6), using identical sweep window and gain settings.

D. Fluorescence behavior

Non-thermal luminescence due to x-ray exposure is often observed in targets containing dielectric materials, including YAG:Ce scintillator crystals used as fluorescent screens for beam alignments, and diamond anvil cell targets often comprising multiple layers of dielectrics (Fig. 7). On shorter sweeps, in the 5–50 μs range, this often manifests in SOP images as short pulses of emission, coinciding in time with irradiation from the XFEL pulses, and can be attributed to x-ray fluorescence. Fluorescence emission pulses are thus discriminable from thermal emission as they are usually symmetric in time (unlike heat pulses[31]), appear at lower power (where direct heating is small), and only where transparent dielectrics are present in the beam (which also have low emissivity). X-ray fluorescence also increases quasi-linearly with x-ray fluence (Sec. V D). Since fluorescence appears in the streak images as a symmetric peak in time, in most cases we treat it as instantaneous, with an apparent width due only to the PSF of the combined optical-detector system. That is, the width is not dependent on time since true emission duration is much smaller than the time resolution of the utilized streak windows, and instead the width represents the physical size and distribution of emission arriving on the photo-cathode of the streak camera. Femtosecond-excited fluorescence and decay would normally exhibit asymmetric behavior. Indeed, some minor deviations from symmetric emission are observed but are generally not well resolved in experiments to date. The fluorescence could be examined in more detail using faster sweeps but this was not attempted here. Fluorescence peak profiles are thus well modeled with a Lorentzian function. Peaks can be fit to determine peak location, amplitude, and full width at half maximum (FWHM)—which is also the FWHM of the PSF.

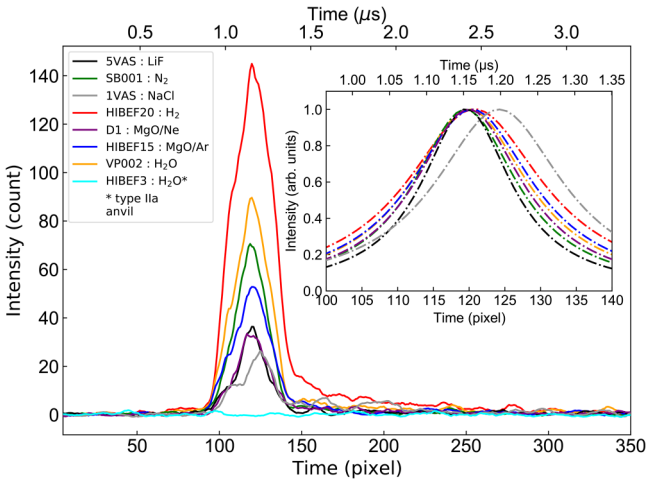

FIG. 7. Fluorescence emission from DAC targets under single XFEL pulse irradiation, at 100% XFEL transmission (see Table III for energy on the target). Emission is averaged in wavelength and plotted against time in pixels, as apparent emission timescale is independent of the sweep rate and represents the detector point spread function in most cases. The targeted materials are low-Z pressure-transmitting media, indicated in the legend, which were usually placed around other samples of interest and which could be independently targeted by the XFEL. These have low degrees of direct heating and low emissivity (and hence, negligible thermal emission). Most DAC targets employ type Ia anvils, with one sample (H_2O medium) with type IIa anvils shown for reference. The inset shows Lorentzian fits to the fluorescence emission (arbitrarily scaled) for each of the emission profiles. All spatial filters and slits were removed during acquisition.

Fluorescence can also be forward modeled if these parameters are known.

Figure 7 shows how fluorescence emission, collected when operating in the slitless configuration, can be commonly observed from DAC targets when irradiated by x-ray pulses (here a single pulse). Emission intensity is pronounced when using type Ia diamond anvils, and may vary with respect to the pressure medium. In contrast, no fluorescence emission is observed from Type IIa diamonds with an H_2O pressure medium. Other experiments targeting an interface of the diamond with a metal have confirmed significant fluorescence from Type I diamonds and total absence of fluorescence from Type II diamonds, limiting the emission to the diamond itself. For almost all of the targets, fluorescence emission follows a similar Lorentzian-like distribution in the time domain. This confirms the timescale of fluorescence emission is instantaneous in comparison to the streak window and so indicates the PSF of the optical system. However, in the case of an NaCl sample, a time delay and asymmetry of the emission peak is observed with the corresponding Lorentzian fit shifted significantly to later times. The results suggest that the fluorescence lifetime of NaCl is longer than other materials, and so can be detected here.

The spectral shape of fluorescence emission from select DAC samples (HIBEF24, HIBEF30, and D1, see Sec. IV) is compared to thermal emission from the calibration lamp in Fig. 8(a). The raw emission spectral shape is determined by summing the emission

TABLE III. Table of target samples and experimental parameters used in the presented datasets. The sample material, sample thickness, location (either free standing, FS, or contained at pressure in a Diamond-Anvil Cell, DAC), pressure, and diamond type are tabulated alongside the source parameters, streak window used and number of integrated sweeps used in each experimental run. Samples (S) or Pressure Medium (M) is either irradiated by the optical laser, operating in either single-sided (SS) or double-sided (DS) mode, the XFEL, or both. Samples are irradiated under vacuum unless indicated. Re or W gaskets are used for DAC samples.

Target/cell	DESY1	SS2	HIBEF3	D1	1VAS	5VAS	SB001	HIBEF20	HIBEF15	VP002	HIBEF30	HIBEF24	XFEL1	XFEL2
Experiment	1	2	2	2	2	2	2	2	2	2	2	2	3	3
Prepared by	EuXFEL	UoE	DESY	LLNL	UoE	UoE	YU	UoE	LLNL	APS	Lille	IMPMC	EuXFEL	EuXFEL
							Sample							
Sample	Pt	Ta	Au	Ta	*Various*	Cu/Mo	Fe	S/Se	Mo	Au	Olivine	Fe	Pt	Pt
Thickness (μm)	5	7	2	5	*Various*	5/5	4	30/20	12	?	20	10	4	4
Location	FS[a]	FS	DAC	DAC	DAC	DAC	DAC	DAC	DAC	DAC	DAC	DAC	DAC	DAC
Pressure medium			H_2O	MgO/Ne	NaCl	LiF	N_2	H_2	MgO/Ar	H_2O/n-Au[b]	Ne	Ne	KCl	KCl
Pressure (GPa)			30.3	12	0.8	5.3	5	0.5	50	14.4	35	60	31	30
Diamond type (US)			IIa	Ia	Ia	Ia	Ia	Ia	Ia	Ia	Ia	Ia	Ia	Ia
Diamond type (DS)			IIa	Ia	Ia	Ia	Ia	Ia	Ia	Ia	IIa	Ia	Ia	Ia
Irradiated material	S	S	S/M	S/M	M	M	M	M	M	M	S/M	S/M	S/M	S/M
							Source							
XFEL														
Photon energy (keV)		17.8	17.8	17.8	17.8	17.8	17.8	17.8	17.8	17.8	17.8	17.8		17.8
Rep. rate (MHz)		1.13	2.26	2.26	2.26	2.26	2.26	2.26	2.26	2.26	2.26	2.26		2.26
Pulses/train		1	1–5	4	1	1	1	1	1	1	20	1		10–30
Energy/pulse (μJ)[c]		293	506	720	413	115	801	483	500	672	567	536–689		420
Filter transmission		0.5	1	1	1	1	1	1	1	1	1	0.1–1		0.12–0.5
Energy on target (μJ)[d]		44	152	216	124	35	240	145	150	202	170	21–161		15–63
Optical laser														
Waveform	WF_0												WF_0	WF_0
Pulse length	250 ns												250 ns	250 ns
Single/double sided	SS												SS	DS
							Streak camera setting							
Streak window	1	5	5	5	5	5	5	5	5	5	200	5	5	5
Integrated sweeps	1000	1	1	1	1	1	1	1	1	1	1	1	1000	1

[a]Experiment conducted in air.
[b]Pressure media contains nanometer sized particles of Au.
[c]SASE XGM (upstream).
[d]Energy/pulse × Filter transmission × Beamline loss factor (0.3).

Journal of Applied Physics ARTICLE scitation.org/journal/jap

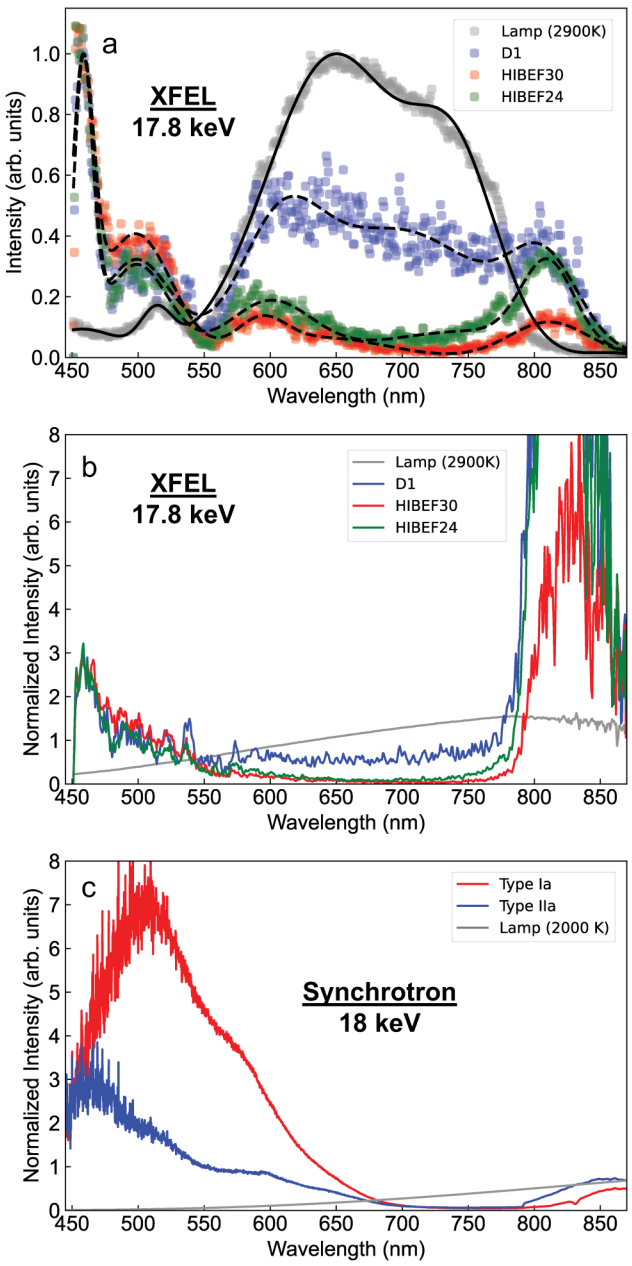

FIG. 8. Wavelength dependence of emission intensity from fluorescent samples compared to thermal emission. (a) Spectral shape of fluorescence emission from D1 (blue), HIBEF24 (green), and HIBEF30 (red) compared to the spectral shape of thermal emission from a calibration lamp (at 2900 K). Fitted emission spectral shape is shown in black. All three samples use Type Ia diamond anvils on the upstream side. (b) Spectral shape of fluorescence emission from D1 (blue), HIBEF24 (green), and HIBEF30 (red) after accounting for the transmission function of the optical system. See Fig. 5(a) for the transmission function of the optical system used. (c) Spectral shape of fluorescence from type Ia and IIa diamond, after accounting for the transmission function of the optical system, measured under 18 keV synchrotron x-ray irradiation at the GSECARS beamline, Advanced Photon Source.

from large numbers of pulses over many spectrograms and within spectrograms, where there is no thermal emission and only fluorescence emission is present at the time of the fluorescence pulse. Strong peaks in fluorescence emission at ∼450 and ∼800 nm, not seen in emission from the calibration lamp and located in lower-sensitivity spectral ranges of the SOP, are characteristic of the XFEL induced fluorescence. Spectral shape is fitted to five super-imposed Gaussian distributions which approximate the distribution shape for fluorescence forward modeling (see Secs. V D–V F). Similarly, after accounting for the transmission function of our optical system, we see that the strong peaks in fluorescence are magnified, while there is minimal emission between 600 and 750 nm, where we observe a strong thermal signal [Fig. 8(b)]. In comparison, Fig. 8(c) shows the spectral shape of the fluorescence emission measured for both Type Ia and IIa diamonds under synchrotron x-ray irradiation at 18 keV. The spectrum for the Type Ia diamond was measured from an upstream diamond anvil of a DAC, with the x-ray beam targeting the Re gasket to exclude emission from the sample and downstream diamond. The Type IIa spectrum was measured from a free-standing diamond.

E. Experimental timing, time resolution, and PSF

The time resolution of temperature measurements is set by the choice of time bin width. The measured PSF establishes the minimum usable time resolution for a certain configuration, below which it is not possible to measure dynamic processes. For example, noisy (e.g. low temperature) data require a larger time resolution, whereas high temperature data with strong signal can be analyzed with a small time resolution, but not smaller than the PSF since this is the intrinsic response time of the detector.

The PSF of the streak images is highly dependent on the optical configuration used, including entrance slit widths. During initial commissioning at EuXFEL, when all spatial filtering and slits were present, the PSF was 15 pixels when the SOP image was binned 2 × 2, i.e., 30 pixels for 1 × 1 binning, which is 140 ns for a 5 μs streak window. When the spatial filter and slits were removed, the PSF widened to 25 pixels FWHM, i.e., 50 pixels for 1 × 1 binning, and 242 ns for a 5 μs streak window. There was also a shift in the peak locations (by ∼2 pixels earlier). Improvements after the experiments reported here further reduced the PSF with spatial filtering and slits to 7 pixels FWHM in 1 × 1 (un-binned) images (i.e., 34 ns for a 5 μs streak window), using an optical configuration similar to experiment 3 (Tables I and III).

Sweep rate, and the associated streak window, of the SOP spectrograms were initially set to factory calibrations.[69] We confirmed streak window lengths by measuring the distance between neighboring pulses of fluorescence emission. XFEL pulses that are incident on target are separated by 443 ns in this study; therefore, we expect that the associated fluorescence emission is also separated by 443 ns across all wavelengths. By comparing the measured pulse separation of XFEL pulses in pixels to the known pulse separation in seconds, the full length of the streak window is calculated. Durations of the 5, 10, 20, and 50 μs streak windows are determined to be 4.73, 9.27, 18.57, and 45.64 μs, respectively (Table II). For streak windows longer than this, we are unable to determine duration as there is insufficient resolution between neighboring

peaks in emission to determine pulse separation. For a 5 μs streak window, we determine that the factory calibration is acceptable, while for longer windows, the discrepancy between our measured values and the factory calibration is such that measured values are recommended. Further measurements are required to determine the absolute timings of the other streak windows. A linear sweep rate approximation is found to be accurate enough for most analyses (including all those presented here), however, non-linear corrections are required in certain scenarios, for example, in modeling fluorescence at smaller PSF where the precise location of the fluorescence peak becomes important.

Fluorescence peak position can also provide absolute information on x-ray timing within the streak window. Thus, where it was possible, the fluorescence of a particular target was used to determine the global timings of streak images collected for that target, i.e., time zero is set to be the time at which the first pulse in any given train reaches the target. If insufficient or indistinct fluorescence emission was present for data on a particular target, then experimental timings were estimated from the timing of separate YAG:Ce screen fluorescence or from the onset of optical emission. Relative timings of the optical laser were estimated using emission observations, and local photo-diodes which observed both radiation sources.

F. Emission spectrogram reduction

During image processing, the background is first removed by subtracting a dark image from the data and is further corrected by subtracting the averaged emission intensity in the spectral "dead" zone (850–955 nm).

Each spectrogram is binned with respect to the time axis, therefore reducing the time axis to discrete time steps at which we determine temperatures. The size of each bin is the time resolution, t_R, of a run and will vary based on the type and quality of emission. The time of each bin is calculated to be the time at the center, with $t = 0$ denoting the time at which the sample is first irradiated. Generally, a t_R comparable to the FWHM of the PSF optimizes the time resolution.

A moving average of the intensity of optical emission with respect to wavelength was also computed in order to visually better compare noisy data with the Planck fit. The spectral intensity distribution is determined by a 50 pixel (or 37.5 nm) wide moving average, regardless of sample or streak window.

G. Temperature measurement

The time-resolved history of sample temperature is determined through a two-parameter least squares fit[70–72] of each time-binned emission spectrum to a modified Planck distribution

$$I_{Planck}(\lambda, T) = \frac{1}{F(\lambda)}\epsilon(\lambda)\frac{2hc^2}{\lambda^5}\frac{1}{\exp\left(\frac{hc}{\lambda k_B T}\right) - 1}, \quad (1)$$

where

$$F(\lambda) = \frac{I_{cal}(\lambda)}{I_{Planck}(\lambda, 2900\text{K})}. \quad (2)$$

Here, $I_{Planck}(\lambda, T)$ is the intensity of emission at a given wavelength, λ, and temperature, T; $\epsilon(\lambda)$ is emissivity (here, in arbitrary units) and $1/F(\lambda)$ accounts for transmission function of the optical system and detector; h, c, and k_B are Planck's constant, the speed of light, and Boltzmann's constant, respectively. We assume a gray-body approximation for emission and, therefore, emissivity is taken to be constant in wavelength ($\epsilon(\lambda) = \epsilon$).[50,73,74] Temperature and emissivity are correlated fit parameters in Eq. (1) as the magnitude of the emission intensity can be increased either by increasing temperature or emissivity. Equation (2) shows how the transmission function is calculated based on the ratio of intensity of thermal emission from a W calibration lamp, $I_{cal}(\lambda)$, to the theoretical gray-body Planck spectrum for the lamp temperature (here, 2900 K, see Fig. 6). All thermal emission recorded is normalized by this function [e.g. Fig. 6(d)]. The transmission function is calculated for each time integration bin and streak window used, so that we account for any sensitivity variance over the streak spectrogram (i.e., flatfield correction). Collection of the calibration spectrogram is made using the enclosing trigger mode to ensure optimum signal; also, proper spatial filtering must be in place during collection of the extended light source from the calibration lamp, and the streak camera must be operated in gated mode to exclude background noise produced during reverse sweep on the CW lightsource.

As discussed above, certain samples may exhibit x-ray fluorescence during XFEL experiments which can overlap with any thermal signal present. In the examples discussed here, fluorescent emission is clearly discriminated from thermal emission. It only occurs during XFEL pulses, often as distinct peaks (or as a continuum where pulses overlap in longer sweep windows), whereas thermal emission often persists after pulses due to the longer relaxation time of thermal processes. Fluorescence is particularly strong in the blue where thermal emission is usually insignificant. Spectra containing high fluorescence also exhibit clearly non-Planckian trends. Here, we explore removal of fluorescence emission to improve temperature analysis by building an empirical model of the fluorescence spectral and temporal shape and fluence dependence, for any given sample. This is based on data where no thermal emission is observed (at low XFEL power), which then establishes fluorescent background for thermal emission data (at higher XFEL power) (Sec. V D). We find that when the fluorescent background is weak compared to thermal signal it has a negligible influence on the assessed temperatures. Additionally, fluorescent emission tends to be temporally localized so that purely thermal emission can be detected at other times (e.g., between or after pulses).

A number of criteria were used for automatic data reliability assessment in temperature measurements. These criteria were based on a careful review of data accuracy and noise performance and exclude spurious data but do not guarantee measurement quality. Data are excluded if

1. There is significant (>30%) signal at or below zero intensity (after background subtraction), within a time bin. This implies insufficient optical emission to determine sample temperature. It should be noted that in high noise datasets the standard deviation of intensity in a binned spectrum can exceed the average intensity even after this exclusion is applied, but there is sufficient signal above zero for reliable fitting.[75]

2. Least-squares fitting returns temperatures below ~1500 K.[11,13,48,51,57,58]
3. The emissivity determined from fitting the data to Eq. (1) (ϵ_{fit}) is 1000 times smaller or 100 times larger than the emissivity determined from fitting the emission spectrum from the calibration lamp (ϵ_{cal}), i.e., $100 \cdot \epsilon_{cal} < \epsilon_{fit} < 0.001 \cdot \epsilon_{cal}$. This criterion accounts for physical limits on emissivity variation and the possibilities for different size emitting areas observed.
4. The magnitude of temperature uncertainty (Sec. II H) obtained from least squares fitting exceeds 50% of the absolute temperature.

Temperature is ideally uniform over the heated area which the measurement is restricted to using the slits and spatial filter. The wavelength dependent emission as a function of time can be used to infer local temperatures reached and the subsequent rate of temperature change unambiguously.[11] However, temperature gradients are expected to be present in the observed surface areas even when using these filters due to (a) imaged beam sizes similar to or smaller than spatial filtering elements, (b) Gaussian (or similar) beam spot profiles, (c) misalignment and beam drift, (d) thermal conduction in targets, (e) overlapping exposures in x-ray pulse trains, and (f) interplay of optical and x-ray beams of different sizes. Spatial filtering elements (slits and spatial filter) were removed in some earlier experiments to address XFEL beam drift, but this should not affect the observed temperature distribution significantly as the optical pathway and observed area is only weakly affected by this. We consider that the observed temperature in SOP represents the maximum achieved on the observed sample surface, considering the strong scaling of emission intensity with temperature in the visible range and findings in comparable offline systems (e.g., the optical laser heated DAC).[55] Our experiments combining large-spot optical radiation and small-spot x rays bears out this expectation, with local hotspots tending to dominate apparent temperatures (see Sec. V).

H. Temperature error

We use two independent ways to calculate the error on the temperature that is determined through least squares fitting: (a) from the in-built error from the *curve_fit* function in the SciPy python package[72] that is used for fitting and (b) from the curvature of χ^2 in temperature-emissivity space.

The built-in Python error estimate, which is based on the minimization of the goodness-of-fit parameter χ^2 and calculated from the square-root of the diagonal of the covariance matrix, is consistently the smaller of the two.

The curvature of χ^2 space is assessed by plotting χ^2, given by

$$\chi^2 = \sum_i \frac{(I(\lambda_i) - I_P(\lambda_i, T))^2}{\sigma_I^2} = \frac{(T - T_{fit})^2}{\sigma_T^2} + \chi^2_{\min} \quad (3)$$

as a surface about the minimum, i.e., as a function of the temperature and emissivity, then assessing the local curvature as[76]

$$\sigma_T^2 = 2\left(\frac{\partial^2 \chi^2}{\partial T^2}\right)^{-1}. \quad (4)$$

In Eq. (3), $I(\lambda)$ is the measured intensity as a function of wavelength where σ_I is the standard deviation of $I(\lambda)$. $I_P(\lambda, T)$ is the ideal Planck intensity for any arbitrary temperature T [Eq. (1)]. We take σ_I as the standard deviation between the measured intensity $I(\lambda)$ and the ideal blackbody intensity $I_P(\lambda, T_{fit})$ at the measured temperature T_{fit}, as determined by the python *curve_fit* routine. The temperature at which χ^2 is a minimum is the best-fit temperature, T_{fit}, with the uncertainty in the measurement given as σ_T.

The second derivative of χ^2 [Eq. (4)] about the minimum determines σ_T. Assuming a quadratic relationship between χ^2 and the temperature of the form $\chi^2 = \alpha \cdot T^2 + \beta \cdot T + \delta$ implies that $\sigma_T = \sqrt{1/\alpha}$.[76] Considering that fit parameters are strongly correlated, we compute the second derivative in χ^2, with respect to temperature, using the minimum magnitude of χ^2 at each temperature, i.e., with emissivity allowed to vary. This is intended to represent a conservative error estimate. The minimum on the contour map slightly differs from the temperature determined from the *curve_fit* fitting routine but only by up to several degrees; the difference is too small to observe in our plots.

Figure 9 shows the χ^2 contour map from least squares fitting of the calibration lamp at 2500 K, calibrated to emission from the same lamp at 2900 K. The standard deviation, σ, in a parameter is defined as the magnitude at which a parameter needs to change from the fitted value, i.e., $\sigma_T = |T - T_{fit}|$, in order to increase χ^2 by 1, i.e., $\chi^2(T) - \chi^2_{\min} = 1$. Figure 9 shows the variation in the goodness-of-fit parameter, χ^2, as a function of temperature and relative emissivity about the minimum, with the 1σ contour shown in black; the inset shows the quadratic fit of χ^2 versus temperature. Both the error determined with this method and that determined

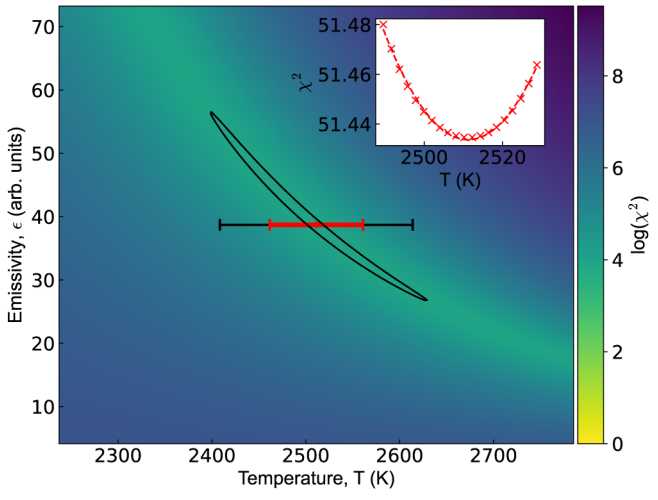

FIG. 9. Example of a χ^2 contour map of the two-parameter least squares fit of wavelength resolved thermal emission from calibration lamp (at 2500 K). A 1 σ_T contour is shown in black about the minimum, with the associated error based on Eq. (4) shown as a black error bar; the error determined from the python *curve_fit* fitting routine is also shown for comparison in red. The inset shows quadratic fit of χ^2 taken along the minimum path across the contour map, used to establish σ_T.

from the fitting routine are shown as temperature error bars for comparison (black and red bar, respectively). We observe that the uncertainty that we obtain using this method regularly exceeds the other estimate.

The uncertainty in a single temperature measurement, from a single bin, is expected to be dependent on both the experimental settings, i.e., streak window or MCP gain, and fitting parameters, i.e., time resolution t_R. To investigate how the fitted temperature and its associated uncertainty is affected by changing parameters, a series of calibration spectrograms were taken, with the lamp temperature set to 2500 or 2900 K, the MCP gain varied from 30 to 60, and using streak windows between 1 and 200 μs. SOP spectrograms of the calibration lamp were collected in gated enclosing trigger mode with either 1, 10, or 100 integrated sweeps. Because each image will measure the same, known temperature at all times, we can examine how measurement accuracy and precision depend on time resolution (bin width), sweep window, gain, and integrated sweeps and, finally, compare uncertainty obtained from individual spectrum fits as discussed above to the statistical error in fitted temperature across the image (i.e., standard deviation of fitted temperatures at many times), which represents the true measurement error (Fig. 10).

Figure 10(a) shows how the fitted lamp temperature at 2900 K, collected from single sweeps with 60 MCP gain and a 5 μs streak window, varies across the time axis with changing time resolution. The scatter in fitted temperature increases as the binning time is reduced from 483 to 96 ns. Figures 10(b) and 10(c) show how the average temperature across the spectrogram and its statistical error (standard deviation, given by the error bars), varies as a function of binning time from multiple calibration runs at both 2500 K, with MCP gain at 60, and 2900 K, with MCP gain at 50. The range of PSF values (PSF_{range}, Sec. II E) is shown for comparison. At both lamp temperatures, we see that by increasing the time bin size we decrease the statistical error in the temperature measurement. Figure 10(d) demonstrates how varying the MCP gain affects average temperature, for time resolution fixed at 198 ns in a 5 μs streak window. Generally, changing the gain has very little effect on the average fitted temperature and the associated statistical error as they remain consistent at all gain values. However, increasing the number of integrated images substantially reduces the statistical error. Therefore, in the single shot mode, which is used in the majority of experimental runs, we can increase the MCP gain in order to improve emission detection without largely affecting the validity of the temperature measurement, which implies that additional noise associated with higher gain modes has no effect on measurements.

In all cases above, the streak window has been fixed at 5 μs as it is the most common streak window used in the experiments discussed here. However, observing emission over a longer time window (i.e., up to 200 μs) is often needed to for longer events, such as irradiation by long XFEL pulse trains. With the lamp temperature fixed at 2900 K, MCP gain at 50, and a fixed time bin of 20 pixels, we are able to determine the effects that increasing streak window from 1 μs to 200 μs has on both fitted lamp temperature and its statistical error [Fig. 10(e)]. The reduction in error as the streak window is increased mirrors the effect of increasing the time resolution [Figs. 10(b) and 10(c)], as by fixing the time bin and increasing the streak window, we are essentially increasing the time resolution. Therefore, at longer streak windows it is possible to bin images by a smaller number of pixels and still maintain sufficient emission per bin in order to measure sample temperature precisely.

It is expected that the statistical error in fitted temperature across the image should be equal to the uncertainty of single fits at a given time. By comparing the individual single fit error either from the least squares python fitting routine or the χ^2 map to the statistical error in each image, we evaluate the two practical estimates for temperature uncertainty. Figures 10(f) and 10(g) show results when the lamp is set to 2500 and 2900 K, respectively. The line at which the single fit error is exactly equal to the statistical error (1:1) is shown for reference. Generally, we see that the least squares fitting underestimates the error by a factor of ~0.5 while the χ^2 map error can overestimate the error by up to five times the statistical error. We, therefore, take the least squares fitting error as the standard estimate for the uncertainty of a single temperature measurement in our analysis; where only a single error bar is shown in a plot, it refers to this estimate.

Regardless of collection parameters, we see that the average of fitted temperatures in a given image are consistent with the known lamp temperature [Figs. 10(b)–10(e)], i.e., the mean temperatures match the known temperature within the statistical error better than 68% of the time, consistent with these error bars having 1-sigma precision. Single fits' least squares errors show generally greater deviations from the known temperature [Fig. 10(a)], consistent with our assessment that these are close to 0.5-sigma equivalent precision, in which case, the single fits are in agreement with the known temperature within 1-sigma error ~ 68% of the time. Thus the measurements exhibit good accuracy for this controlled example.

III. EXPERIMENTAL PROCEDURE

Irradiation of samples was performed during SOP observation using a nanosecond NIR optical laser pulse at 1070 nm (LH) and a femtosecond XFEL pulse train, with one, two, or multiple pulses, at 17.8 keV (XH) (see Sec. II A). Samples were free-standing or confined at high pressure in a DAC (Table III). The streak window was set to cover both sample heating and cooling. Figures 11(a) and 11(b) illustrate the differences between the two different pump scenarios. For LH, a rise in temperature as the sample is irradiated is expected, after which the sample should start to cool. Peak temperatures are expected to be observed after the peak in laser power. For XH, each XFEL pulse incident on the sample will cause its temperature to rapidly increase upon exposure, after which the sample will cool. Subsequent XFEL pulses may lead to further increase in temperature if arriving before cooling is complete. An XFEL pulse train with high repetition rate results in a stepwise, saw-tooth like temperature change with time.[31,36] When LH and XH are combined, the process is considerably more complex, as discussed below. In addition to time variation in temperature, spatial variation (and its time dependence) can be important. Integration of a single sweep of a single heating and cooling event (sequential mode), or integration of many sweeps over repeating, ideally identical events (enclosing trigger mode), is employed in different experiments, with the latter improving the signal to noise ratio.[67]

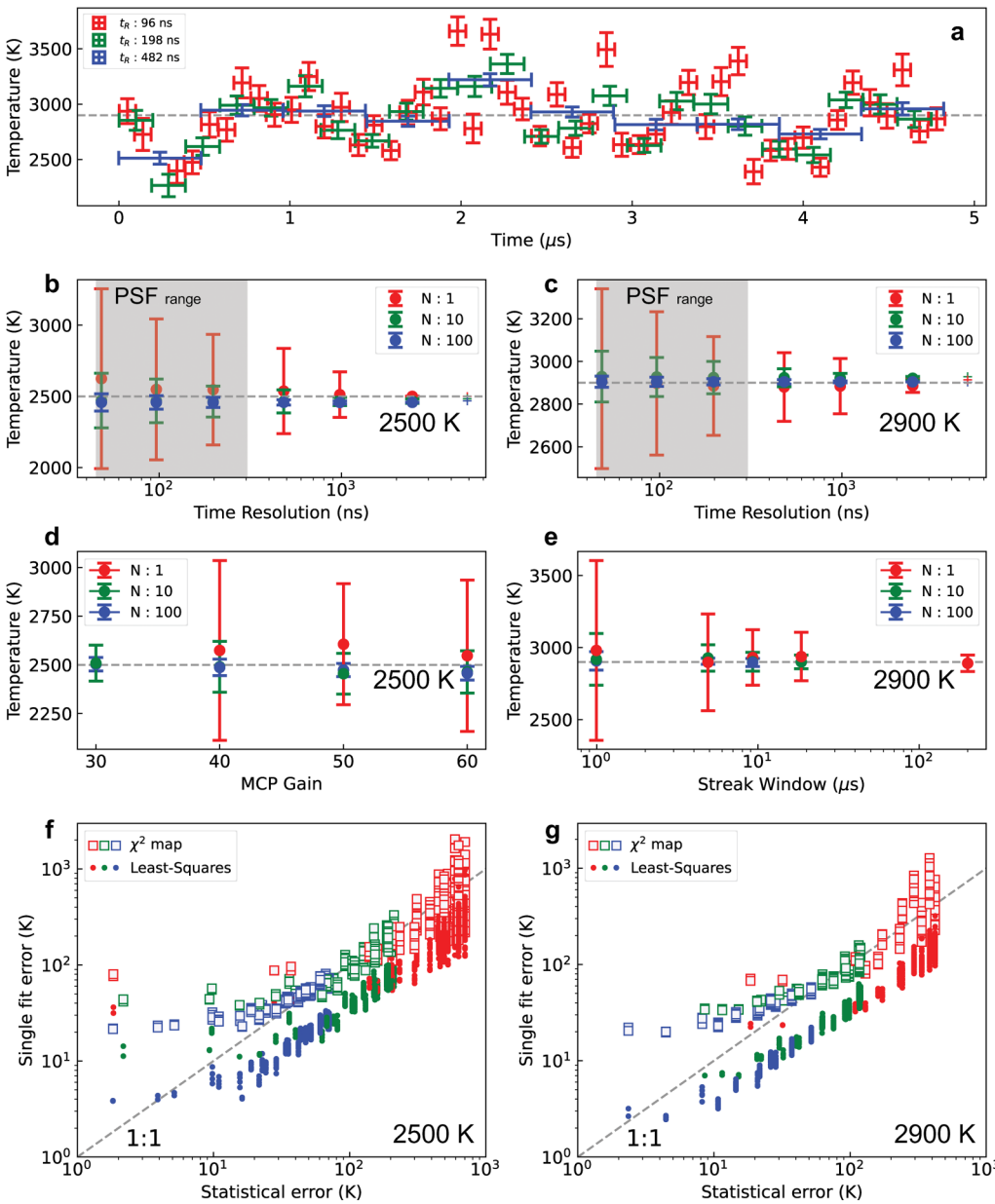

FIG. 10. Temperature uncertainty for changing experimental and fitting parameters for SOP data on standard lamps. Error is determined from fitting single binned spectra (least squares or χ^2 map) and from averages of the fitted temperature over all bins in an image (statistical error, given by standard deviation). (a) Temperature data on lamp set at 2900 K, over a 5 μs streak window using a MCP gain of 60 with a time resolution of 96, 198, and 482 ns and single sweep data collection. The error bar shows the least squares error on each temperature measurement. The number of integrated sweeps are varied in further analysis (b)–(g) as 1, 10, or 100 sweeps (red, green, and blue, respectively). (b) and (c) Average temperature and statistical error for images of lamp at 2500 (b) and 2900 K (c), as a function of time resolution used (bottom axis) and number of sweeps integrated (N). Dashed horizontal line indicates the set lamp temperature, and the shaded region between 45 and 305 ns shows the region over which the time resolution equals that typical PSF values. Streak window is constant at 5 μs and MCP gain at 60 (b) or 50 (c). (d) Average temperature and statistical error as a function of MCP gain (bottom axis) and integrated sweeps (N) at 2500 K. Time resolution is fixed at 198 ns with a streak window of 5 μs. At a MCP gain of 30 we were unable to measure lamp temperature under single shot conditions (N = 1) because of a weak signal (Sec. II G). (e) Average temperature and statistical error as a function of streak window length (bottom axis) and integrated sweeps (N) at 2900 K, with a fixed 20 pixel time resolution and using the full width of the spectrogram in the time axis (1016 pixels). The MCP gain is 50. (f) and (g) Comparison of statistical error (bottom axis) to single fit errors, based either on least squares fitting (closed circles) or χ^2 map analysis (open squares), as time resolution, MCP gain and streak window are varied, at lamp temperatures of 2500 K (f) and 2900 K (g). Vertical lines of points indicate the individual fit error distributions for the bins used to construct a given statistical error. Dashed line indicates ideal trend.

The SOP system was first tested with the NIR pulsed laser heating system, at the Deutsches Elektronen-Synchrotron, Germany (experiment 1) before being moved to the HED instrument hutch at the European XFEL. Results are reported for a free standing sample of 5 μm thick Pt foil employing LH at a repetition rate of 1 kHz (see Sec. V A) with the laser waveform WF_0 (Fig. 3). The streak camera was configured to operate using the enclosing trigger mode over a integration time of 1 s (collecting 1000 heating cycles) with the streak window set to 1 μs. Sample temperature analysis is limited to 525–800 nm (Fig. 5).

Once installed at the HED instrument, we performed MHz repetition rate (1.13–2.26 MHz)[32] pulsed x-ray heating (experiment 2)[33,39,59,61,64] on samples free-standing in vacuum or statically confined in a DAC (Table III). Beam energy was set to 17.8 keV, with a Gaussian profile with a 10–20 μm FWHM and a pulse length of 20 fs. The number of pulses per train varied from 1 to 20 with a pulse separation of 443 or 886 ns. The maximum energy on target per pulse was ~240 μJ with a peak fluence of ~100 J cm^{-2}. Unless otherwise stated, the wavelength range for fitting in this experiment was restricted to 575–775 nm and a 2 × 2 binned spectrogram image size, i.e. 672 × 508 pixels, was used. Due to the limited intensity of emission that we observed at the beginning of the experiment, the slits and pinhole in the optical path were removed mid-experiment, increasing signal.

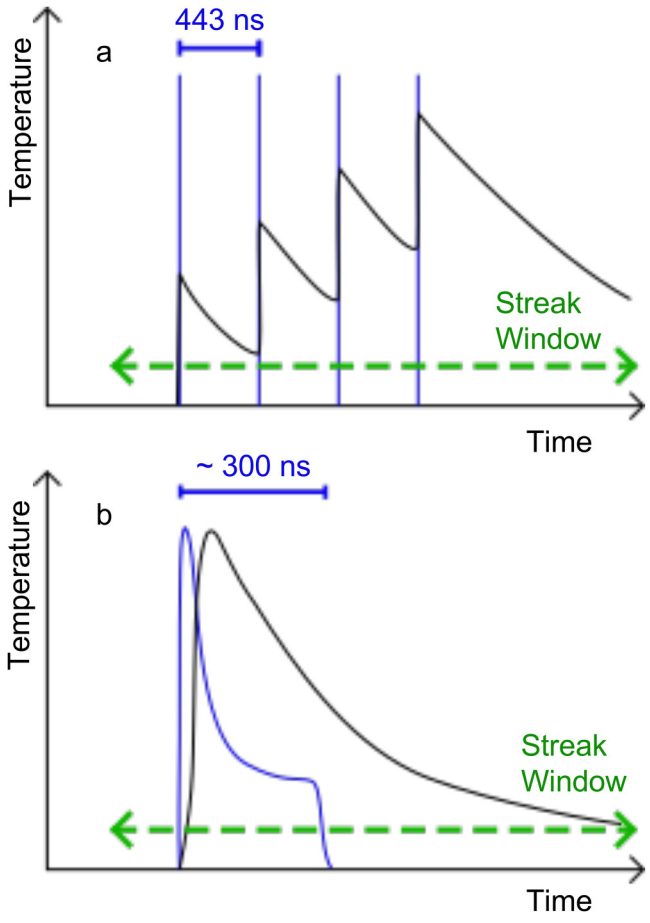

FIG. 11. Schematic of pump–probe timings used in XFEL heating (a) and laser heating (b) experiments. Blue lines indicate the timing and pulse shape of pump pulses, with black lines showing the expected variation of sample temperature. LH pulses (b) are ~300 ns in duration (Fig. 3) with the XH pulses (a) having a pulse length of ~20 fs and a pulse separation of 443 ns at 2.26 MHz.

Further LH experiments were performed at the HED instrument, during a series of laser-heating commissioning runs in combination with XFEL radiation (experiment 3).[63] The goal was to understand how to heat samples optically and probe noninvasively with x-rays. These experiments focused on assessing any combined effects of heating with the NIR laser and XFEL, when both lasers are incident on the sample during collection of optical emission. The x-ray pulse train comprised of 10–30 pulses spaced by 443 ns, an x-ray energy of 17.8 keV, an average energy per pulse on target of 126 μJ at 100% transmission, a focal spot size of 4.5 × 5 μm^2, and a pulse length of 20 fs. Due to improvements in the beam alignment the NIR laser spot, the XFEL spot and the full spatial filtering system (which was in place during this experiment) were all well aligned. The full spectrogram image size was used, i.e., 1344 × 1016 pixels, and streak windows were set to 5 μs. The optical laser was focused on the upstream surface of the sample, aligned to the same location as the XFEL, and sometimes also on the opposing downstream surface of the sample (double-sided heating).

IV. SAMPLE ENVIRONMENT

For experiment 1, the target (DESY1) comprised a 5 μm thick piece of Pt foil suspended in air.

For experiment 2, we report on data from a free standing foil target and samples enclosed and pressurized by a symmetric piston-cylinder type DACs (Fig. 12). For SS2, a 7.0(3) μm thick Ta foil, from GoodFellow, was mounted on a 100(20) μm thick Kapton tape substrate and suspended in vaccuum. DAC HIBEF3 was prepared with 200 μm culet type IIa diamonds, and a 2 μm piece of Au foil was loaded inside the chamber with H_2O and compressed to 30.3 GPa. DAC D1 was prepared with 300 μm culet type Ia diamonds and loaded with a 3 μm thick insulating layer of pressed MgO powder and 5 μm Ta foil before gas loading with Ne and compressing to 12.0 GPa. DAC HIBEF30 was prepared with 300 μm culet diamonds, with type IIa downstream and type Ia upstream, then loaded with three 20 μm thick disks of polycrystalline San Carlos Olivine and a 5 μm Pt foil then filled with Ne gas and compressed to 35 GPa. Some samples also contained a ruby (Al_2O_3:Cr) grain for use as a pressure marker.[77] Additional DAC samples where only the pressure medium was targeted are listed in Table III.

For experiment 3, two symmetric piston cylinder DACs were used. XFEL1 was prepared with 300 μm culet type Ia diamonds and XFEL2 was prepared with 200 μm culet type Ia diamonds. A 4 μm thick piece of Pt foil was placed with an insulating layer of KCl on either side in both cells and compressed to 31 (XFEL1) and 30 GPa (XFEL2).

Sample position was moved, where possible, between runs so that each heating cycle was performed on a fresh unheated sample location.

V. RESULTS

A. Pulsed laser heating of free-standing foil

Figure 13 shows the collected spectrogram and the resulting temperature measurement from experiment 1 (Pt foil in air), based on accumulation of 1000 heating cycles. A peak temperature of 3701 ± 71 K was observed, closely corresponding to the peak in laser power whereas emission intensity peaks later in time. Good agreement of emission spectra with the expected Planck distribution is observed over the full spectral range. We expect that the sample cools to ambient conditions between kHz cycles and that each cycle reaches similar temperatures; the close agreement of the spectra with a Planck distribution supports this. The differences between the different fit error estimations are shown in Fig. 13(b).

B. XFEL heating of free-standing foil

Target SS2 (Ta foil in vacuum) underwent irradiation by a single XFEL pulse at 50% x-ray transmission, which corresponded to a pulse energy of ∼44 μJ on target. Using two different time resolutions, 135 and 193 ns, we determine peak temperatures of ∼6500 K (Fig. 14). Emission was observed for ∼1 μs after exposure [Fig. 14(a)]. A large uncertainty ($\sigma_T > 10\%$) correlates with a weak and noisy emission in this case.[62] That is, despite reaching higher temperature than both the calibration lamp and laser-heated foil in preceding example, the signal is lower due to only single-shot collection, smaller emitting area, as well as use of spatial filtering. Validity of the temperature estimation is confirmed by the damage imprinting observed during post-experiment analysis [Fig. 14(d)]. The observed hole and drip features formed suggest that there was sufficient heating to melt a large area of the target consistent with high peak temperatures measured well in excess of the melting point. The short emission timescale can be explained by rapid target quenching (Sec. VI).

C. XFEL heating of a sample in a diamond anvil cell

HIBEF3 (Au foil in H_2O pressure medium) underwent irradiation by a single train of five XFEL pulses at 100% x-ray transmission and 2.26 MHz repetition rate (experiment 2) with an average pulse energy on target of 152 ± 81 μJ. Two different time resolutions, 96 and 135 ns, were used to evaluate the temperature from the SOP (Fig. 15). This cell was loaded with type IIa diamond anvils, and no additional background from fluorescence is observed (see Sec. II D). In Fig. 15(a), it can clearly be seen that as each XFEL pulse interacts with the target there is an increase in emission intensity on the SOP spectrogram, followed by a drop in intensity between pulses, as expected when the Au foil cools. We observe a peak temperature of ∼5500 K and minimum measurable temperatures of around ∼2500 K. Figure 15(c) highlights how the wavelength dependence of emission intensity changes with both time and temperature.

The temperatures achieved indicate that the Au sample was partly melted during the experiment, as temperatures exceed the known melting point of Au at 30 GPa (T_{melt} ∼2300 K).[7] We can see from the temperature profile that subsequent pulses do not stepwise heat the sample as expected,[31] with peak temperatures averaging about 4500 K at the time of pulses 2–5. This could be due to the specific energies of each pulse in the train, disruption of the Au upon melting,[29] or increase in the opacity of H_2O under high pressure and temperature[23,78] leading to limitations on apparent temperature.[11] It is also notable that peak emission intensity increases with time, despite no clear increase in peak temperature, which can be attributed to increased emitting area (i.e., due to lateral heat conduction) or emissivity (i.e., due to optical changes in pressure medium). Similar effects are detected in other targets. Compared to the freestanding foil, there is a more gradual decay of the emission intensity after heating, likely a result of better confinement and insulation of the sample during quenching.

D. Characterizing x-ray fluorescence

The preceding examples lacked discernible fluorescence, and emission was interpreted as purely thermal radiation. We now discuss targets having significant x-ray fluorescence background (Sec. II D). For example, Figs. 16(a) and 16(b) compare SOP records for irradiation by two XFEL pulses, with an average energy on target per pulse of ∼135 μJ, where a difference in the observed optical emission between the similar samples and different diamond types (Type Ia in VP002 and Type IIa in HIBEF3) can be seen. In both cases, we are observing emission from a Au sample in H_2O pressure medium, at 37.0 and 30.3 GPa, respectively.

While the SOP spectrogram from the sample in DAC VP002 shows emission across all wavelengths below 850 nm, there is very little or no emission detected for sample of HIBEF3. As the only difference between VP002 and HIBEF3 is the diamond type, we conclude that Fig. 16(a) shows the fluorescence signal from the diamonds in VP002. In terms of the spectral response, we see that in the regions where $\lambda < 575$ nm and $\lambda \sim 800$ nm, there are peaks in the emission intensity, which characterize fluorescence emission from a variety of targets (Fig. 8). The optical emission from the sample in VP002 demonstrates a symmetrical shape with respect to time, which as discussed represents the PSF of the SOP.

The weak emission from the sample in HIBEF3 at low XFEL pulse energy [Fig. 16(b)] shows only emission from the second pulse and with a very different temporal and spectral shape than that observed from VP002 — suggestive of thermal emission from cumulative heating. That emission here is purely thermal in nature is further clarified by increasing the XFEL energy on this sample [Fig. 16(c)], i.e., to 245 ± 53 μJ/pulse. The emission is asymmetric with respect to the time axis, with a tail in emission intensity after each XFEL pulse incident on the target, likewise the emission peaks at around ∼700 nm in the wavelength axis, similar to the spectral shape of the calibration lamp (Fig. 8). Finally, a cumulative increase in emission intensity showing stronger emission from the second pulse is clearly resolved, following expectations of stepwise heating. The peak temperature, after the sample in HIBEF3 has interacted with the two XFEL pulses, is measured to be 5282 ± 650 K.

While fluorescence is often of some use, such as for alignment[7] and determining experimental timings (Sec. II E), it can potentially interfere with pyrometric temperature measurements. This is because the measured spectrogram can become a combination of thermal and fluorescence emission at higher powers. Here, we explore how, when there is a large fluorescence signal, e.g., when using type Ia diamond anvils, the fluorescence component

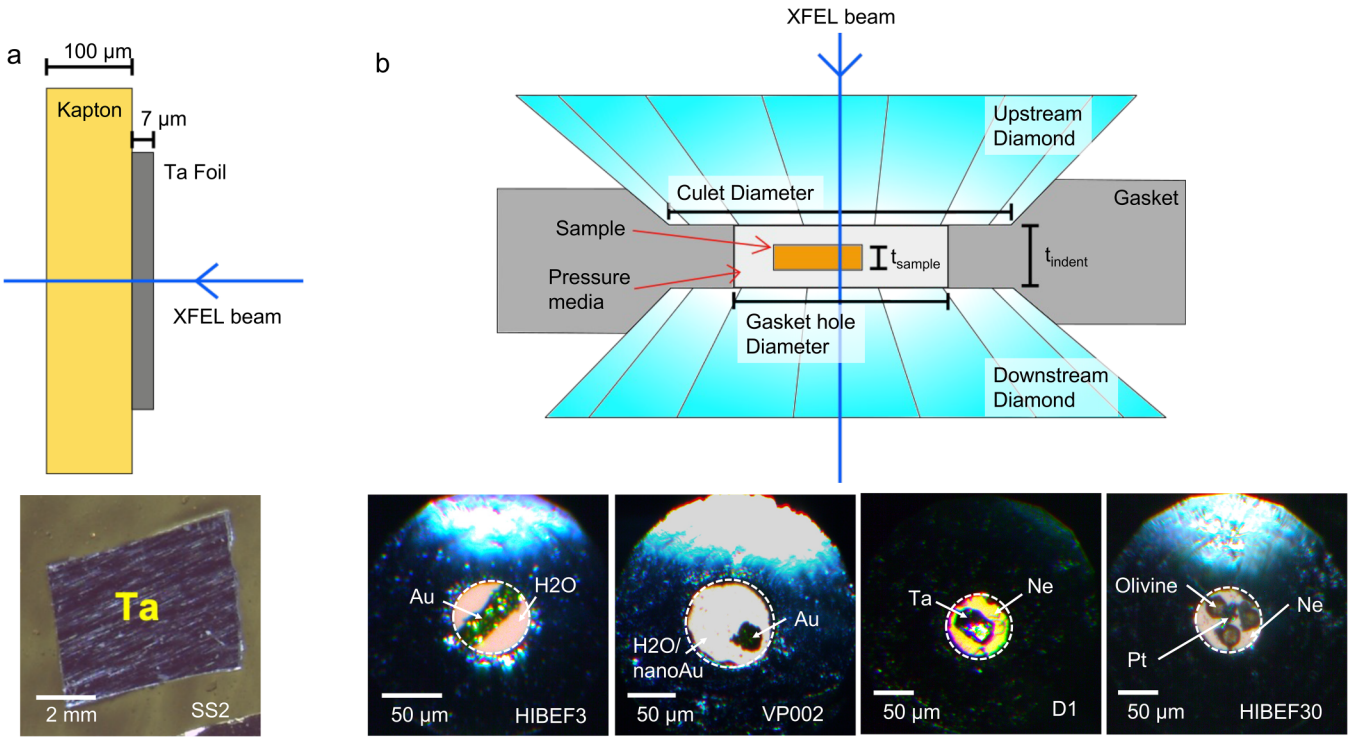

FIG. 12. Schematics and photo-micrographs of free-standing and DAC samples used during experiment 2. (a) Schematic and photo-micrograph of free-standing Ta sample (SS2). (b) Schematic and photo-micrographs of DAC sample configuration used during experiment 2. Photo-micrographs of samples in DACs (HIBEF3, VP002, D1, and HIBEF30) are shown, with the gasket hole highlighted by dashed circle. Sample thickness (t_{sample}), sample chamber thickness (t_{indent}), sample chamber diameter, and diamond culet diameter are shown. Both schematics are not to scale. All photo-micrographs are viewed from the upstream side, with respect to the XFEL beam, and are illuminated by transmitted and reflected light.

can be removed before temperature measurement. We, thus, examine whether and how the fluorescence signal would distort the spectral shape and temperature being measured.

To remove the fluorescence signal, we have developed a method to create a synthetic SOP image that simulates the fluorescence emission for a particular sample configuration. By measuring the optical emission from the same target at low XFEL beam transmission, with the same optical configuration and sample containment, and varying numbers of XFEL pulses, we can survey the fluorescence emission shape in both wavelength and time before the onset of any thermal emission. The streak window used in each run is kept constant throughout and all runs are recorded in sequential (single sweep) mode in order to correlate observed fluorescence with the power of each individual XFEL pulse.

The time evolution of fluorescence emission under pulsed XFEL heating is determined by multi-parameter least squares fitting[70–72] of a superposition of Lorentzian distributions (one Lorentz distribution is used for every pulse in the XFEL pulse train) to the wavelength-averaged spectrogram emission intensity in the UV region [$451 < \lambda < 545$ nm; Figs. 17(c) and 17(d)]. No pincushion effect was accounted for prior to fitting. Peak separation in each fit is fixed and corresponds to the time between XFEL pulses in a train (here 443 ns). At low XFEL transmission there is minimal or no thermal emission so we observe a good fit between the Lorentzian curves and emission intensity with time [Fig. 17(c)]. Whereas at higher XFEL beam intensity and number of pulses there is only good agreement between the Lorentzian distribution and emission intensity at the start of the record (time $< 0.75\,\mu$s) where only a few pulses have irradiated the sample, typical of a signal dominated by fluorescence [Fig. 17(d)]. That is, optical emission from later pulses (time $> 0.75\,\mu$s) do not exhibit a good fit to the expected Lorentz shape and are seen to reach peak intensity later than expected from the pulse separation and have a longer decay time, indicating thermal emission contribution. This gives us a qualitative measure to distinguish between different emission types. After the Lorentz fits from multiple runs have been manually filtered, to only include fluorescence pulses, we can determine the average FWHM, or PSF, and amplitude of fluorescence emission in the time axis. The relationship between emission intensity and XFEL pulse energy, as measured by the beamstop photodiode "PD_3" [Figs. 1(b) and 17(e)],[20,39,61,62,79] is determined to be a power-law fit [$\text{Intensity} = 0.072 \cdot \text{PD\_3}^{0.83}$ for D1, Fig. 17(f)]. We can, therefore, determine the expected fluorescent emission intensity from the photodiode signal for any run using this sample. Spectral shape is determined through a least squares fitting of time-averaged emission intensity from the accumulated spectral shape from multiple fluorescence-only runs to five superimposed Lorentzian distributions

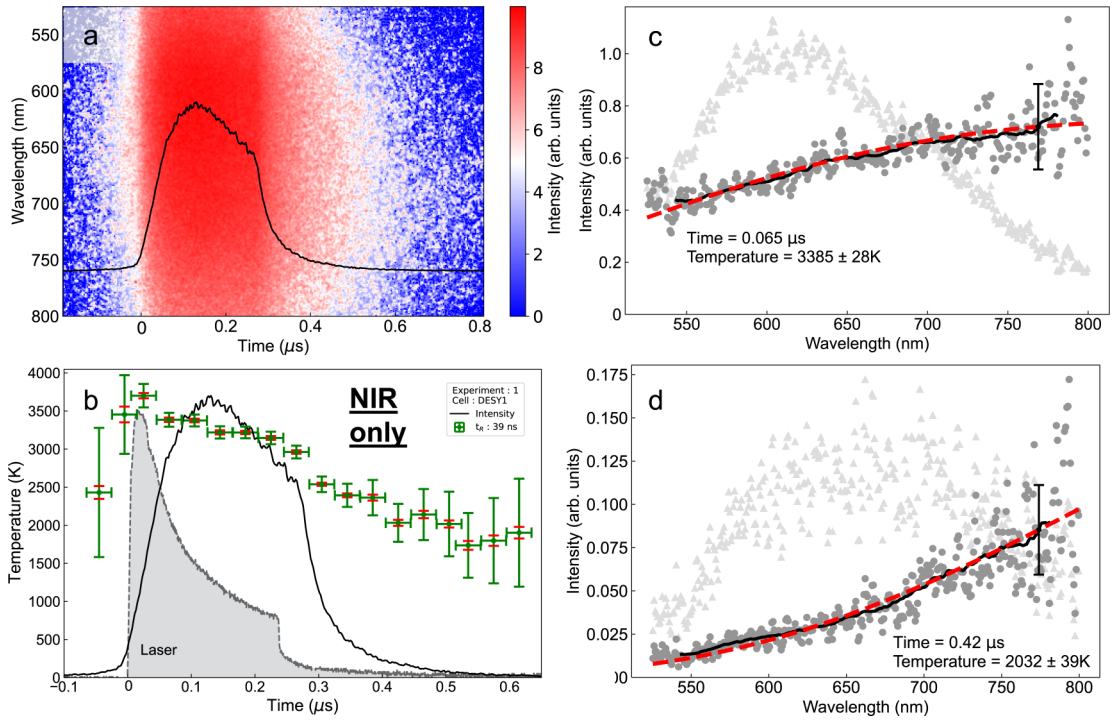

FIG. 13. Optical emission collected from laser-heated platinum foil (5 μm thick, DESY1) using a 1 μs streak window and the enclosing trigger mode. Time resolution is set to 39 ns. (a) SOP spectrogram with wavelength axis restricted to 525–800 nm. Relative intensity profile with respect to the time axis (averaged over this wavelength range) is shown in black. (b) Final temperature history with both temperature error estimations shown. Error from least squares fitting is shown as the red error bar, and green is the error associated with the contour on the χ^2 map. Emission intensity is the black curve, and laser pulse intensity is the filled gray profile (timing estimated from the onset of emission). (c) Binned optical emission at time = 0.065 μs and Planck fit to data determined through the least squares fitting (red dashed line) at $T_{fit} = 3385 \pm 28$ K. (d) Binned optical emission at time = 0.42 μs and Planck fit to data determined through the least squares fitting (red dashed line) at $T_{fit} = 2032 \pm 39$ K. (c) and (d) show the original uncorrected emission data (gray triangles), the corrected emission after taking into account the transfer function of the system (dark gray circles) and the moving average of emission (solid black line). The average standard deviation in emission intensity during smoothing is shown as a single black error bar.

[Figs. 8 and 17(b)]. We expect the results of the above fitting routines to depend highly on sample configuration, window thickness, materials present in the beam, etc., and so should be analyzed independently for each sample.

A synthetic fluorescence-only SOP image is then created using the average FWHM emission duration, amplitude of emission with respect to photodiode intensity and spectral shape of emission [Fig. 17(g)]. Subtraction of the synthetic fluorescence emission from the raw SOP image yields a modified SOP image which is used for temperature determination [Fig. 17(h)].

E. XFEL heating of a diamond anvil cell after fluorescence removal

An example of a target with considerable fluorescence emission is DAC D1 (5 μm Ta foil in MgO/Ne medium at 12 GPa in a DAC with Type Ia diamonds). After removal of fluorescence emission (Fig. 17, see Sec. V D), sample temperature is determined for four pulse XFEL irradiation at 100% x-ray transmission (216 $\pm$ 26 μJ/pulse) (Fig. 18).

Here, we can see that emission from the first pulse is entirely due to fluorescence; prior to fluorescence removal, peak temperatures of 4000–6000 K were suggested, however, after correction the temperature is too low to detect ($\lesssim$2500 K). The second pulse shows comparable levels of fluorescence and thermal emission; however, the apparent peak temperature rises from ~4000 to ~5000 K upon fluorescence correction. Hence, the effect of fluorescence on apparent temperature is not straightforward. Subsequent pulses (3 and 4) show much higher thermal emission than fluorescence, with the correction having a negligible effect. Finally, there is a long tail of thermal emission after the pulses which is not affected by fluorescence background and is unaffected by correction. As in the prior example of a DAC under XFEL irradiation (Sec. V C), peak temperatures reached after each pulse remain relatively constant later in the pulse train, while emission intensity rises.

F. XFEL heating with longer pulse trains and SOP windows

With large numbers of pulses available at high repetition rates at modern XFEL sources (e.g., 2700 pulses at 4.5 MHz at European

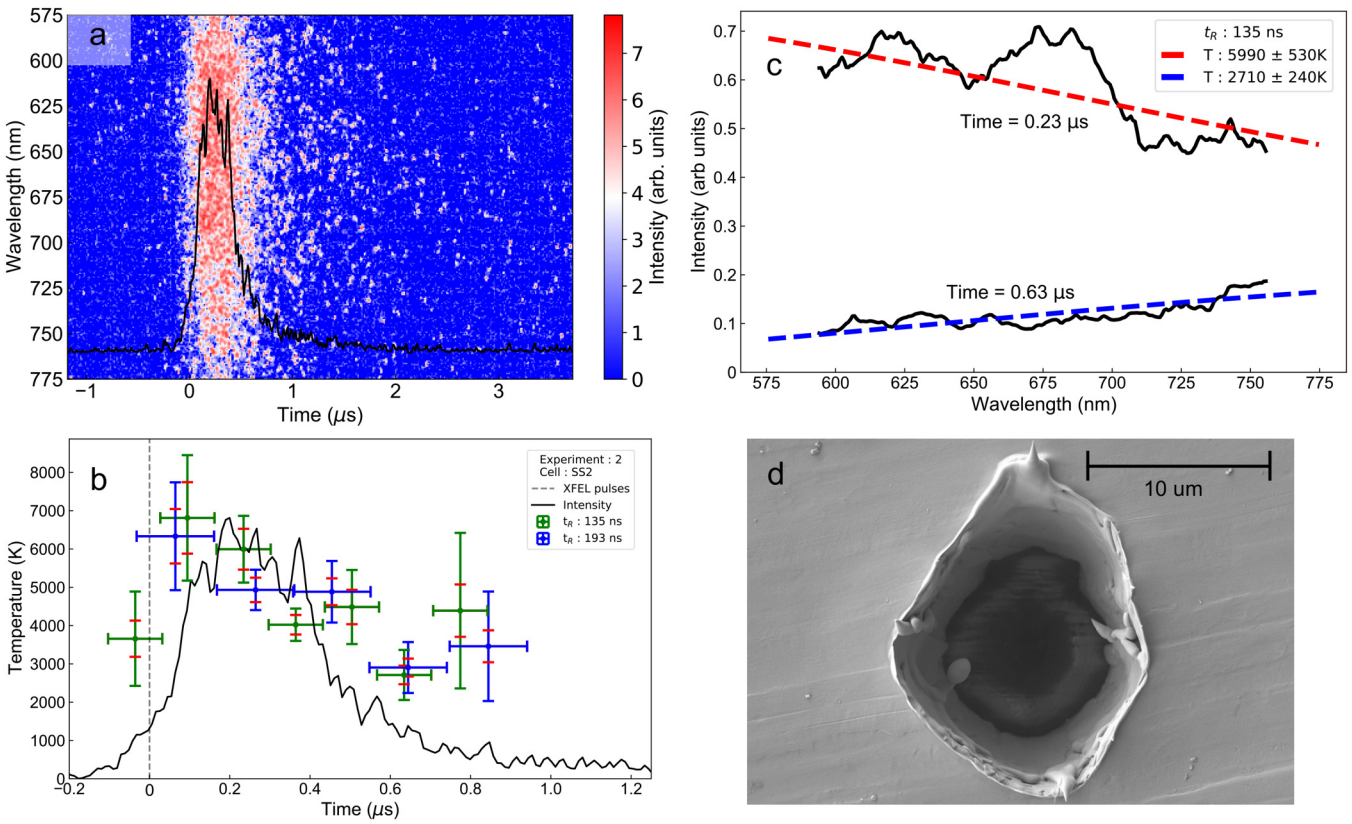

FIG. 14. Optical emission from single-pulse XFEL irradiation of tantalum foil (7 μm) in vacuum (SS2) with streak window set to 5 μs. Wavelength range for fitting is restricted to 575–775 nm. (a) SOP spectrogram with integrated intensity for reference (black). (b) Temperature history using two different time resolutions, 135 (green) and 193 ns (blue), with relative intensity of emission for reference. Both error estimations for every temperature are shown (red is the least squares error, and green/blue shows the error determined from the contour χ^2 goodness-of-fit map). The time at which the XFEL pulse is incident on the sample is shown as a single vertical dashed line (based on fluorescence timing observed in other targets). (c) Gray-body spectral fits to optical emission data (black lines). Red and blue dashed lines are the Planck fits at T_{fit} = 5990 $\pm$ 530 K and T_{fit} = 2710 $\pm$ 240 K, respectively. (d) Post-beamtime SEM image of damaged target area.

XFEL), there is much potential in using SOP in dynamic experiments on longer timescales. However, as the streak window length is increased, the spacing, in pixels, between successive XFEL pulses is reduced. This leads to poor definition between the optical emission of neighboring peaks and the expected saw-tooth like shape of emission intensity with time is smoothed out. In addition, it may be more difficult to discriminate and model fluorescence background. This means at longer streak windows, we cannot easily identify emission from individual XFEL pulses in the pulse train.

An example of this scenario is given here for an oxide mineral sample (olivine) with low absorbance and slow thermal transport dynamics at 35 GPa in a DAC (HIBEF 30), undergoing cumulative heating over 20 XFEL pulses at 2.26 MHz with a streak window of 20 μs (Fig. 19). Fluorescence emission is evident from additional datasets collected at lower power, which shows characteristic strong emission in the blue.

To determine the expected fluorescence emission in this case, we surveyed the optical emission from a short streak window, e.g., 5 μs, at varying XFEL pulse energies and converted it to the longer streak window during modeling, e.g., 20 μs. The spectral shape and time dependence of the expected fluorescence spectrum is determined the same way as described above. To adapt from a 5 μs window to a 20 μs window, we assume the spectral and temporal shape [Fig. 19(b)], PSF (Sec. II E), and amplitude of emission intensity dependence on photodiode values is independent of the streak window but the spacing, in pixels, between XFEL pulses is reduced. The resultant fluorescence emission in the time domain [Figs. 19(a) and 19(d)] shows a continuous distribution throughout irradiation.

After removal of the fluorescence emission, the thermal-only signal is observed [Fig. 19(e)] and can be used to measure sample temperature [Fig. 19(f)]. By comparing the SOP spectrogram measured before [Fig. 19(a)] and after [Fig. 19(e)], the fluorescence emission is removed we can clearly see that the emission on the thermal-only image is only significantly changed during the first 5 μs. This suggests that the emission in the first 5 μs is dominated

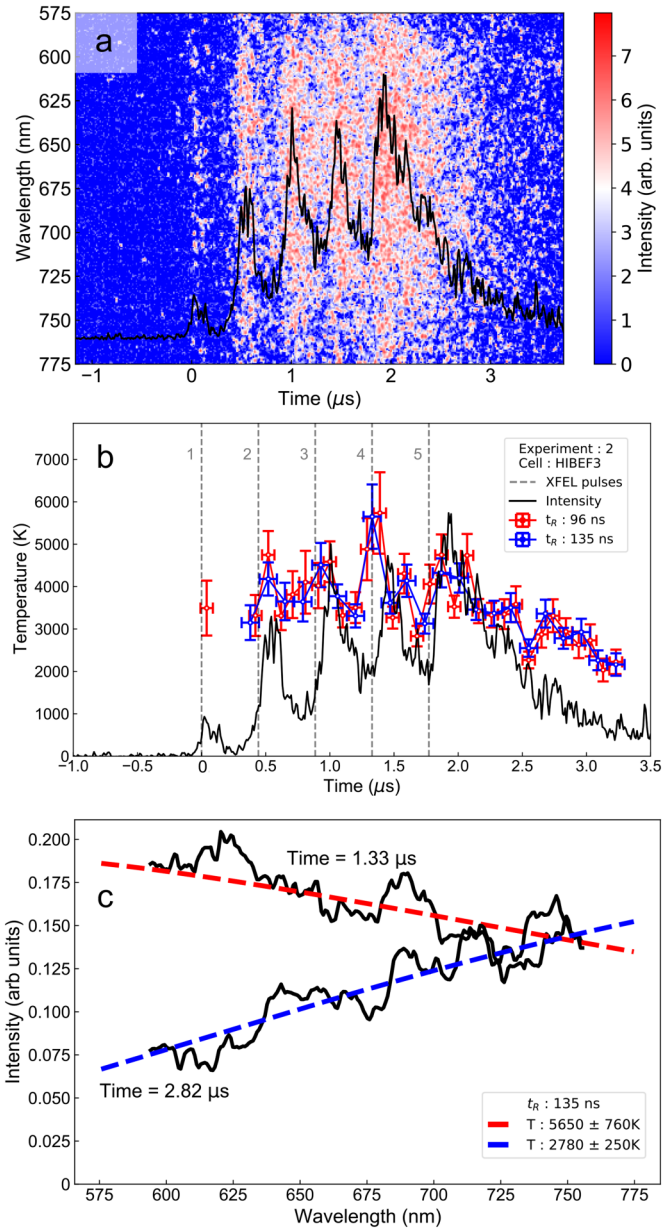

FIG. 15. Optical emission from five-pulse x-ray irradiation of gold foil (2 μm) in a DAC with a H_2O pressure medium held at 30.3 GPa (HIBEF3). The streak window is set to 5 μs, and the time resolution of the temperature measurements are 96 and 135 ns. The wavelength range used for fitting is 575–775 nm. (a) SOP spectrogram image, with the relative emission intensity, averaged over wavelength range used for fitting shown for reference (black). (b) Temperature history of Au foil measured with two different time resolutions (96 ns red; 135 ns blue), with relative intensity of emission for reference (black). The times at which the XFEL pulse train is incident are shown as dashed vertical lines. (c) Gray-body spectral fits to optical emission data (black lines). Red and blue dashed lines are the Planck fits at T_{fit}= 5650 $\pm$ 760 K and T_{fit}= 2780 $\pm$ 250 K, respectively.

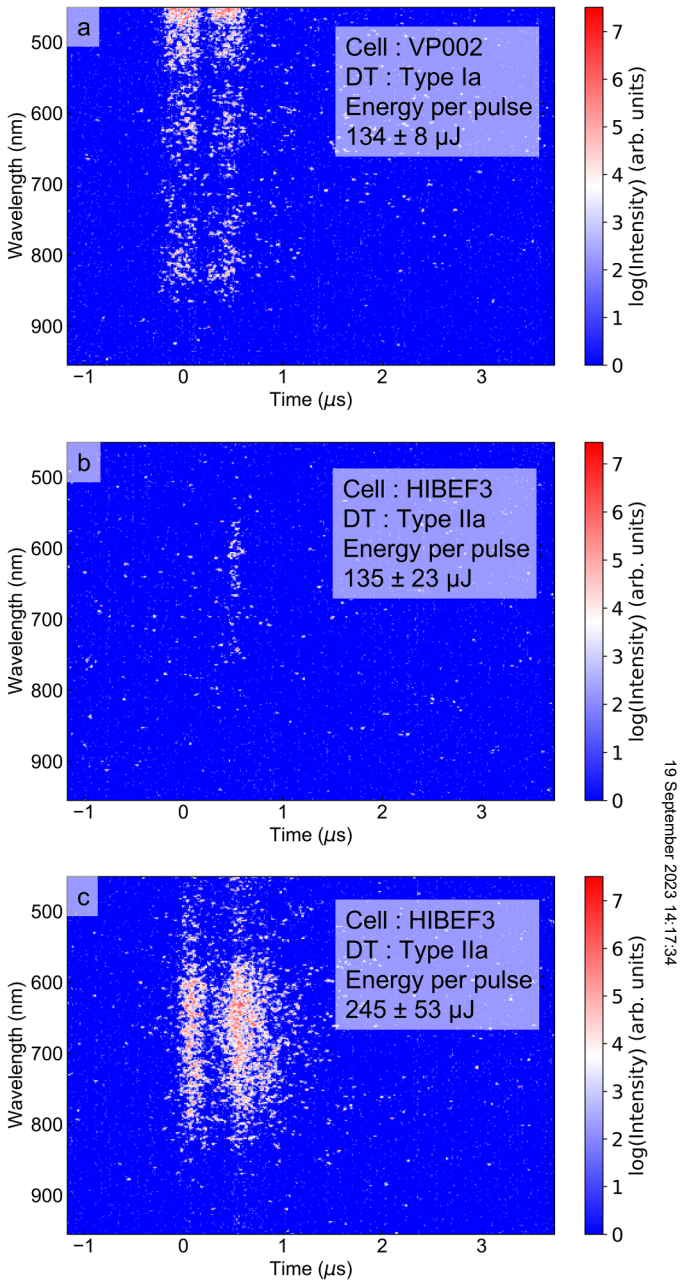

FIG. 16. Optical emissions observed from two-pulse XFEL irradiation of gold foil (2 μm) in a DAC with a H_2O pressure medium from VP002 and HIBEF3. The upstream diamond type (DT) varies. During collection of emission the spacial filtering was removed, and the streak window was 5 μs. (a) SOP spectrogram of optical emission when cell is assembled with Type Ia diamonds (VP002, upstream diamond thickness = 2.201 mm) at 37.0 GPa. Average energy per pulse is 134 $\pm$ 8 μJ. (b) SOP spectrogram of optical emission when cell is assembled with a Type IIa diamond (HIBEF3, upstream diamond thickness = 2.275 mm) at 30.3 GPa. Average energy per pulse is 135 $\pm$ 23 μJ. (c) SOP spectrogram of optical emission from HIBEF3 irradiated with two XFEL pulses with an average energy per pulse is 245 $\pm$ 53 μJ.

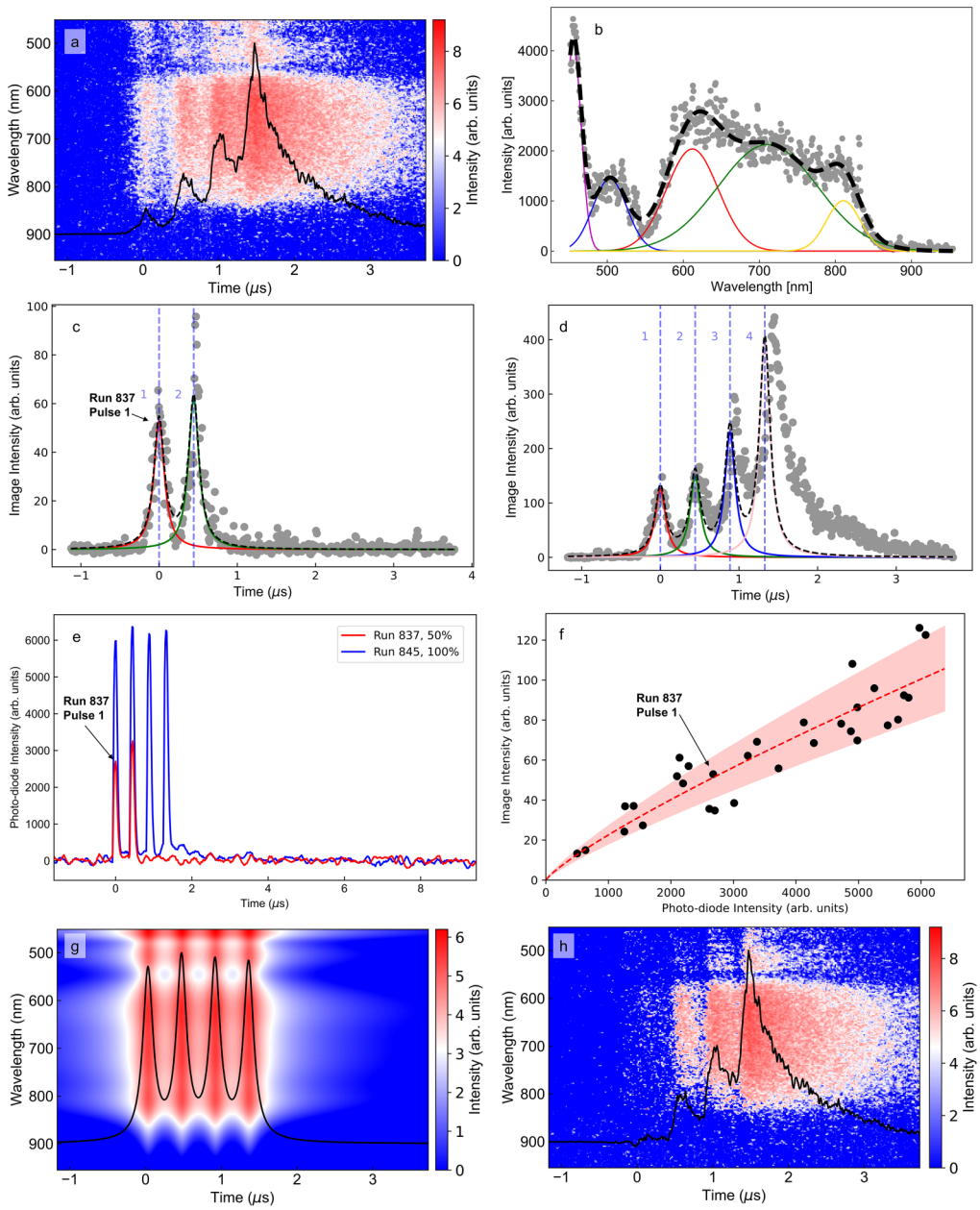

FIG. 17. Thermal and fluorescence optical emission from XFEL irradiation of DAC target D1 (Ta foil at 12 GPa). Streak window is set to 5 μs throughout. (a) Original SOP spectrogram image of four-pulse irradiation on Ta, at 100% transmission of the XFEL beam with relative intensity for reference (black). (b) Lorentz least squares fitting to the time-averaged optical fluorescence emission, gray markers (overall fit shown as black dashed, individual Lorentz fits are shown in solid color lines). (c) Lorentz least squares fitting to the wavelength-averaged optical emission from two pulse irradiation at 50% XFEL beam transmission (run 837), gray markers (overall fit shown as black dashed, individual Lorentz fits are shown in solid color lines). The timing of the XFEL pulses are shown as dashed vertical lines. (d) Lorentz least squares fitting to the wavelength-averaged optical emission from a four pulse irradiation at 100% XFEL beam transmission (run 845), gray markers (overall fit shown as black dashed, individual Lorentz fits are shown in solid color lines). The timing of the XFEL pulses are shown as dashed vertical lines. (e) Photodiode signal showing beam intensity from the runs shown in (c) and (d). (f) Photodiode intensity, from multiple runs [two of which are shown in (e)], against fitted Lorentz distribution amplitude of fluorescence emission (c), black markers, and fitted power-law distribution, red dashed line. Envelope indicates a 20% error on power-law fit. The point labeled "Run 837 Pulse 1" is determined from magnitude of the first pulse in (c) and (e). (g) Synthetic SOP image constructed based on time profile (c), spectral shape (b), and beam intensity (f). Relative emission intensity is shown in black. (h) Corrected SOP image showing only thermal emission from Ta foil with relative emission intensity shown in black.

by fluorescence and that at later times thermal emission is dominant. Thus, only temperature measurement obtained early in the record differs significantly before and after fluorescence emission is removed while there is minimal change in temperature at later times — and none at all after the XFEL pulse train is completed [Fig. 19(f)]. A stepwise heating dynamic is clearly observed in both the temperature and emission records after correction.

As the magnitude of the fluorescence correction to temperature was particularly noticeable here, we also examined how uncertainty in the fluorescence correction might impact the results. To do this, we assumed a uniform increase or decrease of fluorescence intensity across all pulses in the pulse train. An increase or decrease within the uncertainty of the fit to image intensity vs photodiode intensity [e.g., Fig. 17(f)] produced negligible changes in the assessed temperature. Only when intensity errors exceed ∼20% do systematic errors become comparable to the standard error on the temperature. Fluorescence modeling error is less than this critical level for the experiments examined here.

G. Laser heating of a diamond anvil cell

Installation of the laser-heating system at the HED hutch allowed LH of samples in conjunction with x-ray irradiation. We first discuss results for pulsed LH of DAC samples without any x-rays (Fig. 20). Optical emission collected from Pt foil in a DAC with KCl pressure medium at 31 GPa (XFEL1) under pulsed LH with 1000 heating cycles (1 s exposure at 1 kHz streak repetition rate) using the enclosing trigger mode is shown. A peak temperature of 7800 ± 400 K is observed at the peak of emission at 0.12 μs after the start of the laser pulse. The timing of the laser pulse is estimated from the onset of optical emission. Upon repeating this LH run multiple times, we observe that there is a large scatter in the measured temperature (Fig. 21), which can be attributed to changes in the sample coupling, which may be due to repeated melting. In all runs there is an unusual broadening of emission in time, such that emission appears well before the start of the laser pulse with relatively high apparent temperatures. This is possibly due to a bleeding effect occurring due to the large number of sweeps collected in the single image;[67] more study is required to understand this issue. However, it does not appear to play a role in single-shot collections.

H. Laser heating of a diamond anvil cell with XFEL irradiation

Figure 22 shows an example of LH combined with x-ray irradiation of Pt foil in a DAC with KCl pressure medium at 30 GPa (XFEL2). The sample was irradiated by a single NIR laser pulse and 30 XFEL pulses at 12% x-ray transmission. The relative timing of the laser and XFEL is estimated from photodiode traces where both x-ray and optical laser were detected [e.g., Fig. 22(b)], as well as from peak positions in SOP data. Here, the first XFEL pulse is delayed by −510 ns from the start of the optical laser pulse. Instead of extending the streak window to encompass the whole event, i.e., all 30 XFEL pulses, the streak window only recorded the first few pulses. Good alignment of the NIR laser with the x-ray beam is confirmed by clear in-situ detection of laser heating by simultaneous x-ray diffraction.

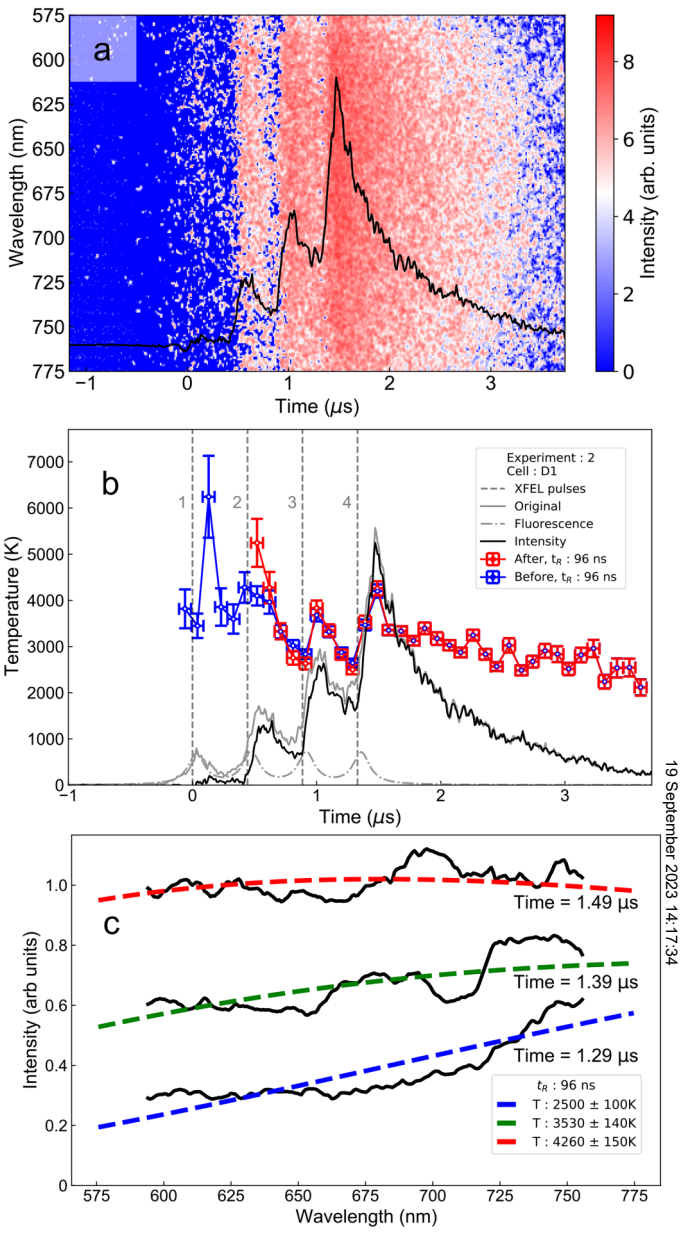

FIG. 18. Pyrometric temperature estimation of a four bunch irradiation of 5 μm Tantalum foil at 12 GPa (D1), run 845, after fluorescence removal (Fig. 17). (a) SOP spectrogram after fluorescence removal showing region of interest used to determine sample temperature (575–775 nm). Relative intensity of emission shown in black. (b) Temperature history before (blue) and after (red) fluorescence removal. The relative emission intensity (post-fluorescence removal) is shown in black, with the fluorescence signal shown as a dashed line and original emission intensity shown in gray. The times at which the XFEL pulse train is incident on our sample is shown as dashed vertical lines. (c) Least-squares fits of data (black lines) to Planck's law at time = 1.29, 1.39, and 1.49 μs. Time resolution is 96 ns in this case. Systematic deviation of data from the Planck fit at lower temperature (upward curvature) may be related to increasing emissivity variation in the visible range at low temperature[68] compared to high temperatures.[24]

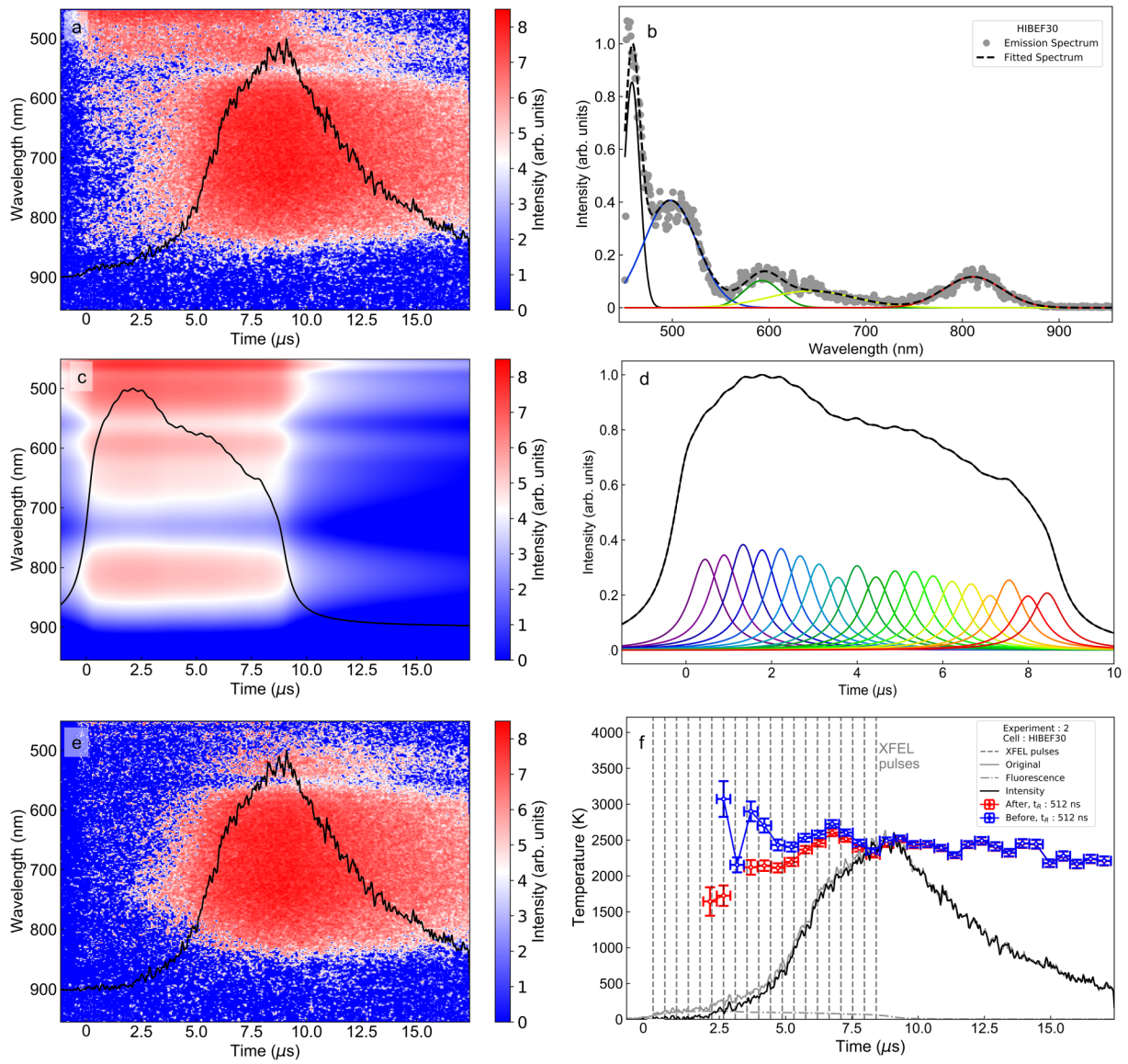

FIG. 19. Thermal and fluorescence optical emission from HIBEF30 (Olivine in Ne at 35 GPa) under irradiation by 20 XFEL pulses at 100% transmission with a 20 μs streak window. The average energy on target across the 20 XFEL pulses was 170 $\pm$ 68 μJ. (a) Original SOP spectrogram of run 781 with the relative emission profile shown in black. (b) Lorentz fit to fluorescence emission spectrum of HIBEF30. Dashed black line shows the best fit line, with five individual Lorentzian peaks shown in color. (c) Synthetic SOP image constructed by combining spectral shape (b) and time dependence (d) of fluorescence emission; time-dependent fluorescence emission profile is shown in black. (d) Model time dependent fluorescence emission for HIBEF30. The black solid line shows cumulative fluorescence emission, with individual pulses shown in color. (e) Corrected SOP spectrogram from run 781 with fluorescence emission removed. (f) Measured sample temperature of Olivine under x-ray heating. The measured sample temperature determined before (blue) and after (red) fluorescence emission is removed is shown. The times at which 20 XFEL pulses are incident on the sample are shown as vertical dashed lines with the relative emission intensity before (gray) and after (black) fluorescence removal.

With the x-ray transmission set at a level where no optical emission is observed from the x-rays alone, it is desired that only the laser pulse will heat the sample while the XFEL pulses will only probe the induced states. From the intensity profile, we observe a steady decrease in emission with time suggesting only laser-heating is occurring. From the temperature profile, however, we observe oscillations in the temperature after the laser pulse—not unlike the behavior shown above for x-ray heated targets, and at higher x-ray power on this target (see below). While subtle, the timing of these excursions, and their rather large amplitude, is consistent with significant XH.

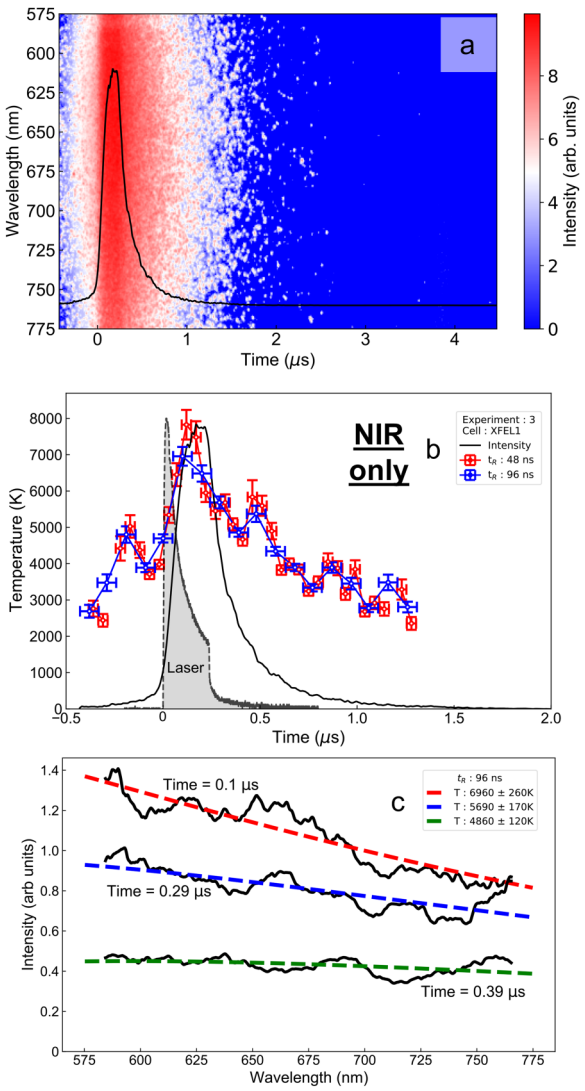

FIG. 20. Pyrometric temperature measurement of pre-compressed Pt with KCl pressure medium at 31 GPa (XFEL1) under pulsed LH. The recorded SOP spectrogram shows the integrated optical radiation collected over 1 s. (a) SOP image with relative intensity of emission shown in black. (b) Temperature history with relative emission intensity shown in black. The estimated time at which the laser pulse is incident on the Pt sample is shown as the shaded region. (c) Least-squares fits of emission spectra (black lines) at time = 0.1, 0.29, and 0.39 μs using a time resolution of 96 ns.

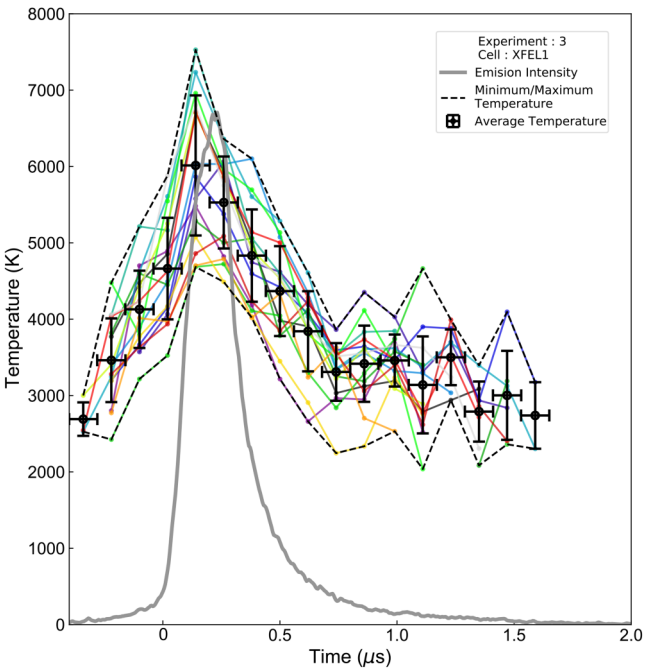

FIG. 21. Reproducibility of pyrometric temperature of pre-compressed Pt with KCl pressure media at 31 GPa (XFEL1) from 16 heating runs using identical NIR laser intensity. The average temperature is shown, with the standard deviation in temperature measurements plotted as the error bar. Individual heating runs are plotted as solid colored lines with the maximum and minimum measured temperature (dashed black lines).

At higher XFEL transmission, combined XH and LH clearly occurs in the target. Figure 23 shows an example of laser heating with x-ray pulse exposures at 50% x-ray transmission, on DAC XFEL2. The XFEL pulse train consists of 10 pulses and the delay of the first XFEL pulse from the start of the optical laser pulse was +60 ns.

Several noteworthy features are seen in the data. High temperatures are rapidly achieved by the transient optical pulse at the beginning of the experiment, as well as high emission intensity. This heat pulse decays with time after the laser shuts off. The contribution from x-ray heating becomes clearly visible after about 1 μs. In comparison to lower power data on this sample, XH roughly maintains the temperature, while emission intensity drops off considerably. The large difference in emission amplitude in the LH stage compared to the XH stage, at a similar temperature, is likely due to the difference in hotspot size. That is, if the LH spot diameter is larger by a factor of ~3 (Sec. II A), the emission intensity should be greater by a factor of 9, which is similar to what we observed. Thus, in this experiment the transition between emission from the larger optical laser heating spot and emission from a smaller hotspot associated with the x-ray beam is observed. Also, rather than sustain the high initial temperature achieved by the optical laser, x-ray heating seems to achieve lower temperatures. This could be due to the conditions adopting a limiting x-ray train heating temperature for this sample,[31] which is lower than that achievable by the optical laser—i.e. where x-ray pulse heating and inter-pulse cooling reach a balance at long timescales.

Finally, there is no detectable fluorescent emission despite using type Ia diamond in this experiment, with emission in both types of heating (LH and XH) equally well described as thermal only. This indicates that the spatial filtering system reduces the contribution of fluorescent emission from diamonds in the SOP spectrum.

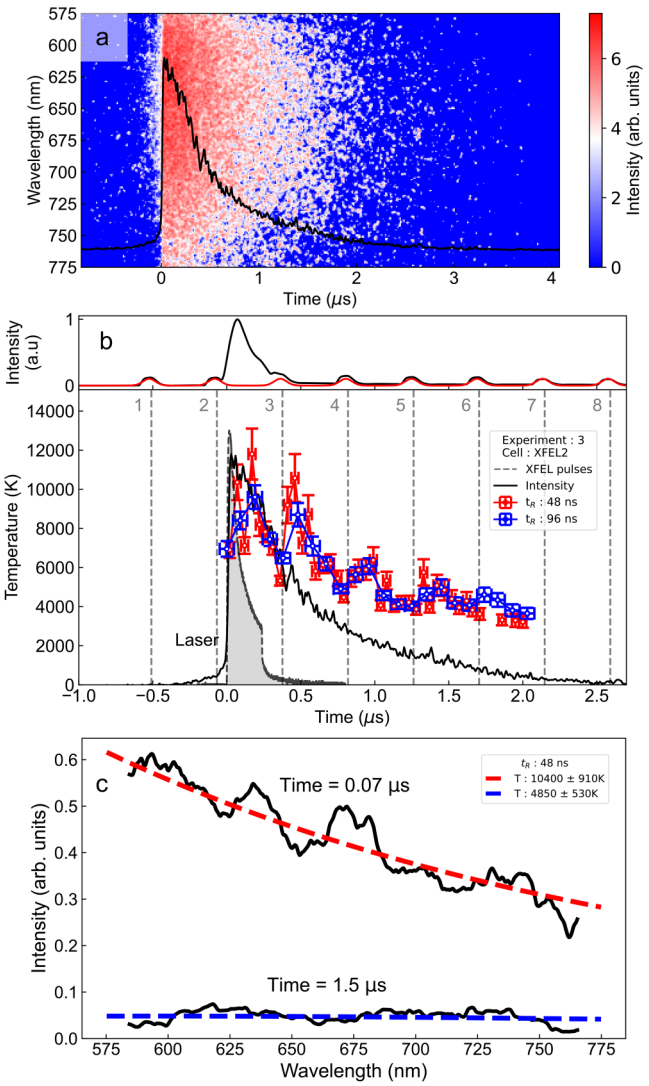

FIG. 22. Optical emission from LH of Pt foil in a DAC with a KCl pressure medium held at 30 GPa (XFEL2), which is simultaneously probed by an XFEL pulse train, consisting of 30 XFEL pulses. Streak window is set to 5 μs and a time resolution of 48 and 96 ns. (a) SOP spectrogram image in the region of interest used for fitting the Planck spectrum with relative intensity for reference (black). (b) Upper panel : Photodiode signal showing the total signal (black) with the XFEL beam intensity (red). Lower panel: temperature history at two different time resolutions (48 and 96 ns), with relative intensity of emission for reference (black solid line). Laser pulse used is shown in gray and the times at which the XFEL pulse train is incident on our sample is shown as dashed vertical lines. (c) Gray-body spectral fits to optical emission. Red and blue dashed lines are the Planck distribution, and black solid line is the data.

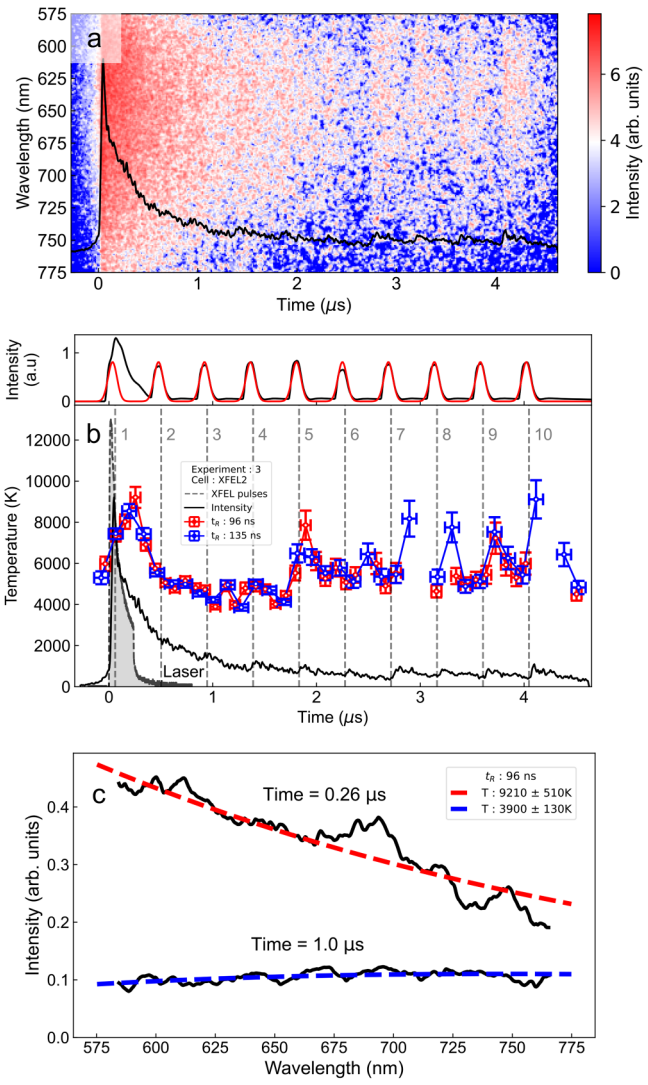

FIG. 23. Optical emission from optical laser and x-ray heated Pt foil (4 μm thick), in a DAC with a KCl pressure medium held at 30 GPa (XFEL2), at higher x-ray transmission than Fig. 22 (see that figure for additional details). (a) SOP spectrogram image. (b) Upper panel: Photodiode record. Lower panel: Temperature history. (c) Least-squares temperature fits.

VI. FINITE ELEMENT MODELING

Given that temperature measurements are deployed here in new experimental scenarios where they have been previously untested, we applied numerical finite element analysis (FEA) to representative cases. Examples of modeling for more traditional experiments (with optical laser radiation only) are discussed elsewhere.[11,13,67,75] That is, while the observations presented here are consistent with qualitative expectations for the heating and cooling behavior of samples under XFEL, optical, or combined radiation sources (Fig. 11), we further compare the observations quantitatively with the expected behavior,[13,31] first as predictions, and in cases where the prediction fails, by optimizing parameters to improve agreement between the model and the data. The objective is to provide greater insight into the heating behavior underlying

the measurements, including the role of time-dependent temperature gradients, the correlation of emission intensity and temperature, and interactions between multiple radiation sources.

In our models, we assume the model geometry is fixed (see Fig. 24) and employ an isobaric approximation for thermal analysis, i.e., that the heating and cooling can be treated as if it occurred at constant pressure.[31] This is suitable for making comparisons with the presented datasets. Temperature changes in the sample after initial heating are due to heat diffusion through the target; radiative heat losses from the sample (by way of thermal emission) have a negligible effect on the results (confirmed by running models with and without radiative losses). Inclusion of latent heat effects[39,80] had a minor effect on the models, but as this did not significantly affect first-order comparisons with the data, it was left out in the models reported here. Temperature dependencies of parameters were included where available, whereas pressure changes with temperature were expected to have only a minor effect and were not included.

The models account for the incident energy per pulse as measured in the beamline, with a factor accounting for transmission to the sample, which is nominally ∼30% of the upstream pulse energy monitor (SASE XGM)[61] as determined in separate analysis of damage imprinting on freestanding foils.[39,62] In this way, the distribution of conditions achieved are predicted from the known beam properties, geometry of samples, and sample properties at relevant pressures and temperatures (Table IV).

Modeled temperatures are reported for the peak upstream temperature for metallic samples and a range of axial temperatures for transparent samples. For heated metal layers, the SOP data will be generally dominated by the maximum temperature on the observed (upstream) surface due to the strong scaling of emission intensity with temperature in the studied temperature range. For nonmetallic targets, emission from a wider range of locations may contribute to observed values. We also report a bulk averaged temperature within the primary sample layer, weighted by beam intensity, to represent the apparent temperature as would be observed by x rays probing the bulk through x-ray pulses. This is computed as

$$T_X = \frac{1}{2\pi\sigma_G^2 d}\int_0^R \int_{-\frac{d}{2}}^{\frac{d}{2}} 2\pi r\ T(r,z)\exp\left(-\frac{r^2}{2\sigma_G^2}\right) dz\, dr, \qquad (5)$$

where σ_G is the Gaussian width parameter of the beam,[31] d is the thickness of the sample, and the sample radius is R, with the normalizing prefactor assuming $R \gg \sigma_G$. Where the latter requirement is not fulfilled the initial T_X falls below the initial (ambient) value i.e., T_0; a correction factor of T_0/T_X from the start of the simulation can be globally applied to the T_X as a correction. This is only relevant to very narrow samples: e.g., for the 25 μm diameter Olivine disks compressed in DAC HIBEF30, comparable in size to the x-ray beam, the correction factor is $300/245 = 1.23$, while it is computed as unity for the other samples analyzed with the finite element technique.

Model results for four datasets are shown in Fig. 25 with sample and model parameters given in Table IV. Model parameters are initially set based on the known geometry, pressure, and literature properties of samples under pressure and temperature; where the model fails to predict the data, certain parameters are optimized to improve the fit as shown in the table. Comparison of the models with the data and the meaning of this analysis is discussed in Sec. VII E.

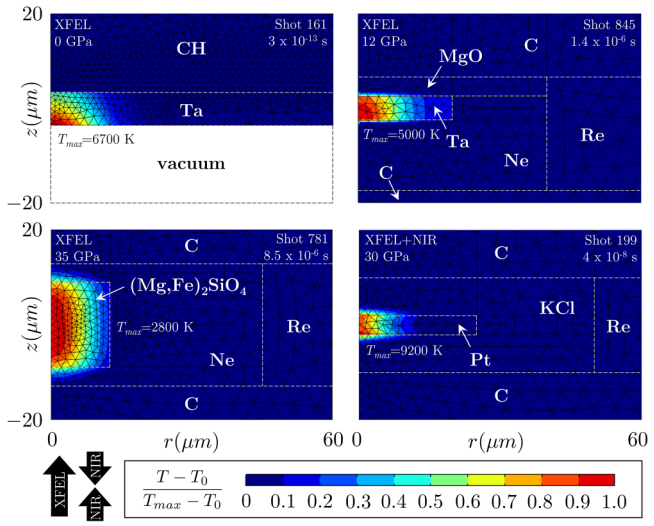

FIG. 24. Geometric configuration of finite element models with mesh, and temperature distribution at peak achieved temperature in each experiment, T_{max}.

VII. DISCUSSION

A. Low signal performance

The minimum detectable temperature of the SOP diagnostic outlined in this study ranges from 1500 to 3000 K for microsecond-duration events. Below this limit, gray-body Planck fits become dominated by background (for well subtracted background this is close to zero counts) resulting in a flat Planck fit determining apparent temperatures in the 3000–4000 K range. Screening of the data based on rigorous criteria is needed to identify and exclude such data, as minimum detectable temperatures can be even lower than the temperatures spuriously obtained when no signal is present. That is, the apparent temperature alone is not a reliable indicator of accuracy or a direct indicator of the detection limit. For example, while low (< 3000 K) and high (> 4000 K) temperatures can be judged as plausibly accurate on the basis of fitted temperature alone, these midrange temperatures can also be mimicked through the background (i.e., absence of signal).

Additional insight is gained by considering the character of the data as the detection limit is passed. Streak camera low intensity performance depends on intensifier gain and other factors, however, some broad trends are observed for this Hamamatsu device. At low signal levels, signal is dominated by individual intensifier events, leading to a spotty appearance of the streak image, with spectral lineouts showing sharp peaks over a low (zero) background. Fits to the data at this condition are dominated by background. As signal level is raised, the number of individual intensifier events becomes sufficient to populate more of the image area and, depending on size of a time bin, the spectral lineout. Once a statistically sufficient number of intensified events are

TABLE IV. FEA parameters. Material properties are thermal conductivity (k), heat capacity at constant pressure (C_P), density (ρ), and absorption coefficient (α). Units for temperature T, pressure P, and density ρ are in K, GPa, and g/cm^3, respectively, where these appear in formulas. Heat capacities are often Shomate fits. Pulse energy is based on SASE XGM upstream energy average and the pulse factors, which represent pulse to pulse variations in energy are determined from the SASE XGM, HED XGM, local photodiode or are left as unity where this information was not available. Where information is left blank, it is not relevant to the model. Text in parenthesis and in bold indicates values optimized after initial estimates to improve match to data; the optical laser energy is for the whole pulse and is only optimized to the data, assuming complete absorption in the upstream sample surface.

Target	Foil array	D1	HIBEF30	XFEL2
Shot/experiment	161/Expt. 2	845/Expt. 2	781/Expt. 1	199/Expt. 3
Pressure (GPa)	0	12	35	30
		Geometry		
Thickness				
Chamber (μm)		24	26	20[a]
Sample (μm)	7	5	18	4
Medium US/DS (μm)	/2000	15/4	4/4	8/8[a]
Diamonds (μm)		2350	2290	2000[a]
Diameter				
Cavity (μm)		80	90	100[a]
Sample (μm)	120	40	25	50[a]
Simulation (μm)	120	150	150	150
XFEL spot (μm)	16	16 **(13)**	16	5
NIR laser (μm)				14
		Material		
Sample	Ta	Ta	Olivine $(Mg_{0.9}Fe_{0.1})_2SiO_4$	Pt
k (W/m K)	57[c]	67[c,d] **(100.5)**	4.10 $(298/T)^{0.493}(1+0.032\ P)$[e]	$64.5+1.03\ P+0.0198T$[f]
C_P (J/kg K)	$1.346\times10^2+2.221\times10^{-2}\ T$ $-1.10\times10^{-6}\ T^2+2.50\times10^{-11}\ T^3$ $-3.243\times10^5/T^2$[h]	$1.346\times10^2+2.221\times10^{-2}\ T$ $-1.10\times10^{-6}\ T^2+2.50\times10^{-11}\ T^3$ $-3.243\times10^5/T^2$[h]	$1585-1.238\times10^4\ T^{-0.5}$ $-3.139\times10^6\ T^{-2}-3.184\ P$ $+8.414\times10^{-2}\ P^2$[i]	133+0.007 75T[f,g]
ρ (g/cm^3)	16.662[h]	17.522[j]	4.028[k]	23.408[f]
α (1/m)	138 696[l]	145 985[l]	2130[l]	235 797[l]
Medium [US/DS]	/Kapton	Ne/MgO	Ne/Ne	KCl/KCl
k (W/m K)	0.46[m]	0.1–1[n] **(.1)**/ $5.9\times(\rho/3.3)^{4.6}\times(2000/T)$[q,r] **(1)**	1[n,o]	28[p]
C_P (J/kg K)	1095[m]	1840[n]/ $1173+0.141\ T-2.17\times10^{-5}\ T^2$ $+2.59\times10^{-9}\ T^3-2.62\times10^7/T^2$ $-5.3\ P+4.79\times10^{-2}P^2$[r,s] **(1000)**	1840[n]	690[f]
ρ (g/cm^3)	1.42[m]	3.074[t]/3.826[u]	3.932[t]	3.644[v]
α (1/m)	92[l]	612/1001[l]	783[l]	4770[l]
Gasket			Re	
k (W/m K)			48[m]	
C_P (J/kg K)			140[m]	
ρ (g/cm^3)			21.020[m]	
α (1/m)			184 000[l]	
Anvils			Diamond	
k (W/m K)			1500[m]	
C_P (J/kg K)			630[m]	
ρ (g/cm^3)			3.510[m]	
α (1/m)			196[h]	
		Source		

TABLE IV. (*Continued.*)

Target	Foil array	D1	HIBEF30	XFEL2
XFEL				
Photon energy (keV)	17.8	17.8	17.8	17.8
Rep rate (MHz)		2.26	2.26	2.26
Pulse delay (ns)		443	443	443
Pulses/train	1	4	20	10
Energy/pulse[w] (μJ)	293	720	567	420
Filter transmission	0.5	1	1	0.5
Beamline loss factor	0.3	0.3 **(0.036)**	0.3	0.3 **(0.038)**
Energy on target (μJ)	44	216 **(25.92)**	170	63 **(7.94)**
Pulse power factors	1	0.88,1.36,0.81,0.95	1.50,1.19,1.28,1.51,1.39,1.41, 1.26,1.09,0.84,1.06,0.84,0.95, 0.94,0.86,0.76,0.72,0.53,0.79, 0.52,0.57	1, 1, 1, 1, 1, 1, 1, 1, 1, 1[a]
Optical laser				
Energy on target (μJ)				24[b] (both sides)
Delay from pulse 1 (ns)				−60
Pulseshape				250 ns (WF_0)

[a]Value estimated.
[b]Value optimized to data.
[c]Reference 81.
[d]Reference 82.
[e]Reference 83.
[f]Reference 11.
[g]Reference 84.
[h]Reference 62.
[i]Reference 85.
[j]Reference 86.
[k]Reference 87.
[l]Reference 88.
[m]Reference 31.
[n]Reference 89.
[o]Reference 90.
[p]Reference 91.
[q]Reference 92.
[r]Reference 93.
[s]Reference 94.
[t]Reference 95.
[u]Reference 96.
[v]Reference 97.
[w]SASE XGM (upstream).

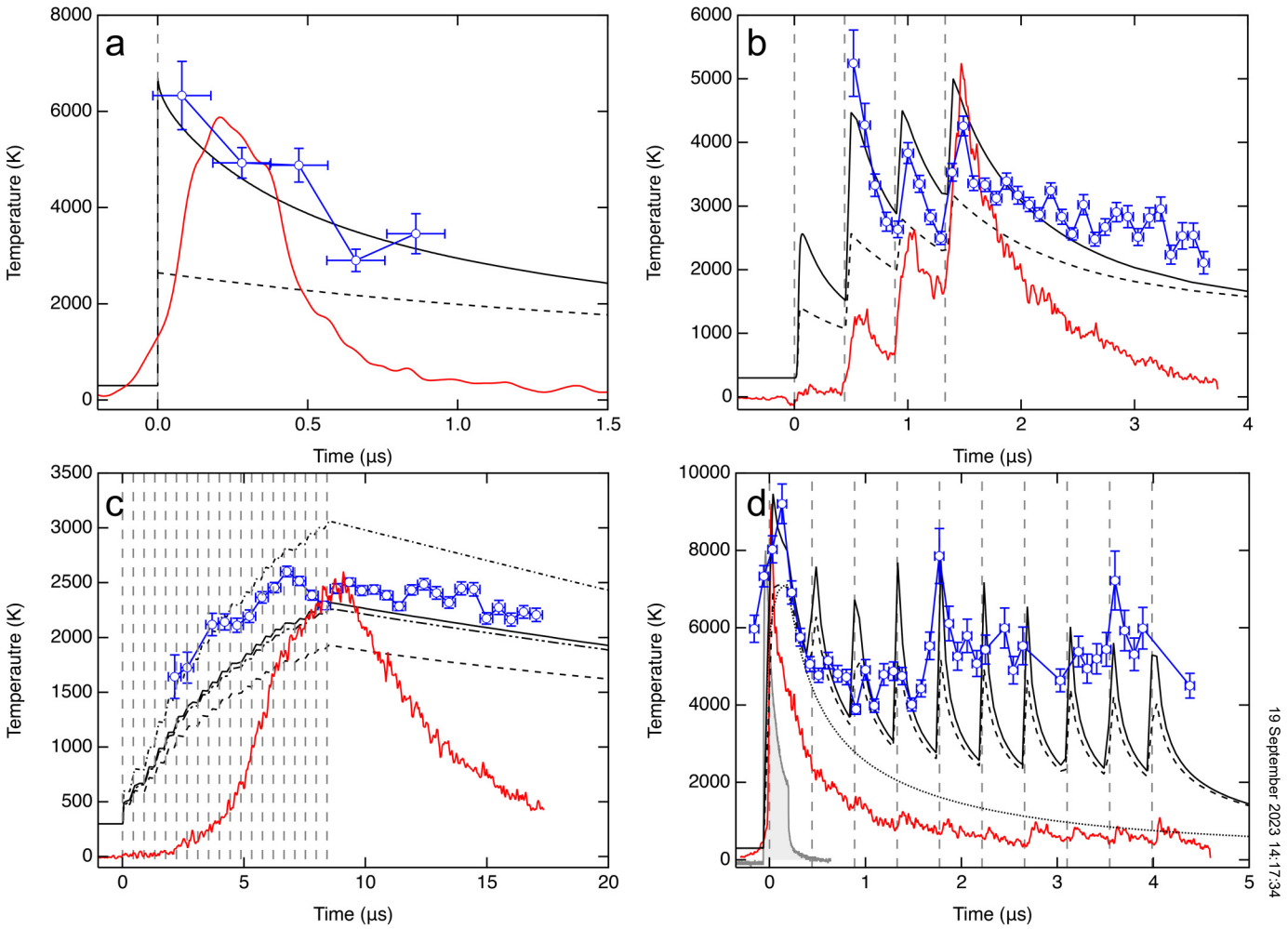

FIG. 25. Finite element analysis of conditions achieved in selected experiments and comparison with SOP data. Measured temperatures are blue, with horizontal error bar showing time resolution (Sec. V); red line shows emission intensity after any fluorescence is removed. FEA results are in black, with the solid line showing the peak (on axis) temperature of the upstream (SOP facing) sample surface, and the dashed line the apparent sample temperature for x-ray probes, T_X. Sources are in gray; vertical dashed lines are XFEL pulses, filled solid line is NIR laser pulse. (a) Conditions for freestanding Ta foil for single XFEL pulse irradiation (Sec. V B). (b) Conditions for Ta foil in a DAC at 12 GPa under 4-pulse 2.26 MHz XFEL irradiation (Sec. V E). (c) Conditions for Olivine disk in a DAC at 35 GPa under 20-pulse 2.26 MHz irradiation (Sec. V F). The dotted-dashed line and dotted-dotted-dashed lines show the temperature, on-axis, in the sample center and downstream surface, respectively, considering that emission can emerge from the whole sample in this example. (d) Conditions for Pt foil at 30 GPa under combined heating with a single NIR pulse, and 10 XFEL pulses at 2.26 MHz (Sec. V H). The dotted line shows the peak temperature on the observed upstream surface if x-ray heating is not included.

present in the binned spectrum, fits become dominated by the signal and begin to accurately represent temperature (as confirmed using our analysis on standard lamps, Fig. 10). A portion of the image area may still be reading background levels even in this case, but a sufficient number of events are accumulated in the time bin to represent the intensity at a given wavelength. In other words, near the detection limit the measurement operates in a quasi-photon counting mode, where accumulating individual intensifier events is necessary to give a statistical picture of emission spectra. Noise emerging from this phenomenon additionally becomes a good indicator of temperature fit quality. We note that low signal performance varies considerably for streak cameras used in SOP applications (see e.g., Ref. 75).

B. Temperature accuracy

The uncertainty of temperature estimation in pyrometry is dependent on many factors, but here it is predominantly controlled by the intensity and noise characteristics of the emission. Planck fits to low emission intensity spectra result in fits that have a larger associated uncertainty. Intensity of the optical emission is intrinsically controlled by the temperature, as described by the Stefan–Boltzmann

relationship between intensity and temperature ($I \propto T^4$, approximately valid in the visible at the present temperatures), as well as the size of the emitting and detected area, the optical properties of the sample, emission duration, and other factors. Hence, the lower bound of measurable temperature depends on a number of experimental details, though below ~1500 K, there is insufficient emission intensity to accurately fit a Planck distribution in any case.

Determining the appropriate time resolution used to fit sample temperature needs careful consideration. Error generally increases with increasing time resolution (decreasing time bin width) as a result of poorer statistics but also by possible introduction of systematic error as discussed above. That is, by reducing the amount of emission in any single time bin, we may introduce effects similar to those observed in the low temperature regime, i.e., due to a spotty appearance of spectra (Sec. VII A). However, by using a significantly larger time bin to reduce the error in temperature, one must also consider the effects related to time-dependent temperature changes, from either the sample heating or cooling within a time bin, which could itself increase the fit uncertainty and systematic error. This may have a somewhat predictable effect due to the T^4 scaling of intensity with temperature resulting in the emission spectrum being dominated by the peak temperature.

Additional sources of systematic error can arise due to perturbations in the spectral shape of emission from any non-thermal emission sources. In our current survey, a significant proportion of data is affected by the non-thermal signal resulting from target luminescence (fluorescence) during x-ray exposures in targets having dielectric components. The spectral shape of emission for a DAC sample is shown in Figs. 8 and 17(b). The spectral shape here is obviously non-thermal and will negativity affect any temperature measurements' precision and accuracy. As shown by Fig. 18(b), the temperature that is determined without accounting for fluorescence emission is significantly different from the actual sample temperature. This effect is small enough to be neglected when the intensity of thermal emission is much larger than that of the fluorescence emission.

Ideally, spatial filtering will both exclude emission from above and below of the sample plane to eliminate non-sample background signal, and exclude emission from outside a selected area of the hotspot, to minimize the effect of integrating signal over spatial temperature gradients or to isolate detection to an x-ray probed area[11] (e.g., to the area probed by XFEL radiation in laser heating applications). Non-sample signal exclusion is here realized using a tight-focusing spatial filter configuration similar to a confocal microscope, as commonly employed in optical Raman spectroscopy measurements in DACs where diamond anvil Raman and fluorescence signals need to be suppressed.[98] Use of higher magnification or smaller pinhole could better isolate detection to a specific region of a hotspot, at the expense of signal intensity and flourescence exclusion. From initial observations at European XFEL, thermal emission measurements are generally light starved, fluorescence background potentially swamps the data, and XFEL beam alignment can vary, so we currently use a filtering scheme with a larger pinhole (50 μm) and 1:1 magnification.

It should be emphasized that due to the prevalence of spatiotemporal gradients in temperature during experiments, the SOP can be taken to represent an average of temperatures in a particular spatial area and over a particular range of time, usually weighted toward higher temperature. The spatial and temporal variations in temperature must be separately accounted for in assessing final uncertainty on measurements of quantities of interest. That is, the SOP temperature should usually, in detail, be considered a spatiotemporal constraint on temperature in an experiment as opposed to the automatically best value of the temperature for a given contemporaneous property measurement (e.g., Sec VI).

C. Target fluorescence behavior

Non-thermal, visible-band optical luminescence generated by XFEL pulses was commonly observed by SOP in targets containing dielectric materials. This luminescence often resembled the conventional fluorescence behavior of the dielectrics under optical excitation, and was consistent with a rapid decay (faster than the time resolution) and broadband emission in most cases. For example, the XFEL-induced luminescence characteristics of diamond and YAG:Ce crystals was effectively instantaneous for the μs-sweeps used here, consistent with conventional relaxation times < 100 ns.[99,100] When excited using a similar x-ray photon energy, fluorescence spectra of diamond are broadly similar between high-intensity XFEL and low-intensity synchrotron irradiation (Fig. 8).

Some deviations from rapid emission were noted for certain sample materials (Fig. 7), with a notable case being that of ruby. In one DAC, a larger ruby piece (used as a pressure marker, see Sec. IV) was targeted independently with the XFEL (Fig. 26). The XFEL-excited ruby luminescence also exhibited conventional fluorescence characteristics, including line emission at ~696 nm (under pressure of ~5 GPa) and a relaxation time measured to be ~250 μs, comparing well with literature values using laser-induced optical fluorescence.[99] This suggests that XFEL irradiation with SOP can allow *in situ* ruby pressure measurements without additional laser excitation, including during dynamic pressure conditions. As ruby was localized in samples, it was easily avoided in practice. Data are currently insufficient to establish the degree of sample contributions to observed fluorescence in most cases in the DAC, with observed variations in fluorescence amplitude likely to be due to different diamonds and stress states.

While the temporal and spectral structure of x-ray fluorescence itself may have interesting properties and applications, we here characterized it principally for the purpose of its removal from thermal emission measurements.

The effect of fluorescence on apparent temperature is not straightforward to predict. When not accounted for in temperature measurements, fluorescence can manifest itself by spurious high or low temperatures, possibly related to emission rising toward both red and blue ends of the visible range in representative cases. In most cases with such contamination, the fluorescence is most strong in the blue and spurious high temperatures may be inferred. While this often leads to clear deviations from an ideal Planck distribution, such as a concave upward spectrum, rising toward both red (thermal contribution) and blue (fluorescence contribution), it may be considerably more subtle. Given that fluorescence emission is unique for each target both in terms of spectral shape and intensity (e.g., due to different diamonds, Figs. 7 and 16), characterization of the fluorescence emission must be performed for each target, and, for DACs, at

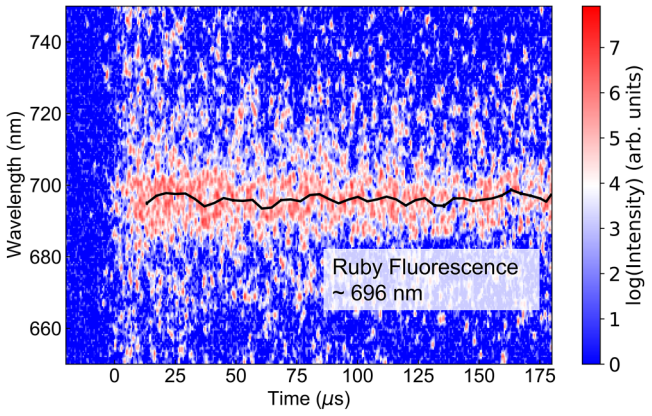

FIG. 26. Optical fluorescence emission from ruby in target SB001 (Fe/N2 at 5 GPa) following single pulse XFEL irradiation (136 μJ/pulse). Black curve is the fitted fluorescence peak, using a single Gaussian fit (20 pixel time average, 2 × 2 image binning), at 696(1) nm, indicating a pressure of 5(3) GPa.[77]

the specific pressure conditions and sample location of interest. Diamonds at Mbar pressures have exhibited unique fluorescence distributions in the SOP differing considerably to those in lower pressure anvils, consistent with pressure sensitivity of fluorescence.[101]

Fluorescence emission can be characterized and removed from SOP spectrograms, but this currently requires reference experimental runs at low XFEL power without any contribution from thermal signal. Given the difficulty of the fluorescence correction even armed with this reference data, its *a priori* elimination is desireable. Assuming most fluorescence emerges from the diamond anvils in DAC targets in studied cases, this can be achieved by eliminating signal from the anvils (or more generally, dielectric matter surrounding the target material of interest). Use of spatial filtering can minimize such contributions, with preliminary observations suggesting it can be reduced considerably for DAC targets (Fig. 22). Use of type II low fluorescence anvils on one or both sides of the DAC may also be valuable if fluorescence minimization is desired (for nontransparent samples, only observed anvils need to be of type II). However, some evidence of sample contributions are also identified (Figs. 7 and 26), so these practices may not entirely be able to eliminate fluorescence backgrounds.

Fluorescence removal may leave residual systematic errors in assessed temperatures, if the corrections are inaccurate. This is particularly an issue where the correction in temperature is larger. However, when considering the case of the largest fluorescence temperature correction observed here (Fig. 19, not including cases where the correction eliminates the detectable emission altogether), we find these systematic errors are negligible compared to the temperature error assessed by least squares fitting.

D. X-ray heating observations

Heating is observed with pulse energies of 10–300 μJ at 17.8 keV on various targets, both freestanding and confined (and pressurized), for a focal size in the range of 5–20 μm FWHM — conditions common for x-ray pump probe experiments at free electron lasers. X-ray heating of samples is a natural by-product of intense XFEL radiation[29,31,37,39] and has been previously observed to occur with detectable optical emission.[37] We here realize the longstanding objective[35] of detecting this radiation with pyrometric techniques in order to determine temperature, while also validating directly heating models.

X-ray heating with single pulses shows a peak and decay in the temperature-time profile which can be understood as rapid (effectively instantaneous) heating followed by a gradual decay as the sample cools. X-ray heating from pulse trains is meanwhile expected to induce stepwise heating,[31] as samples are pumped to higher temperatures while incompletely cooled, assuming constant energies within each pulse. While the SOP images show some evidence of stepwise heating, specifically, a rising thermal emission intensity, temperatures rarely show dramatic corresponding increase later in the pulse trains. A plateau in temperature is expected even when pulse energies are constant due to balance of cooling and heating in time. Moreover, the effect of variable pulse energies can be significant. These effects are considered quantitatively in Sec. VI using FEA models, which confirm that the limiting temperatures with time observed can be considered a direct result of the specific pulse train energy profiles. It should also be noted that sample disruption and internal movement during pulse trains (e.g., due to melting[29]) could also affect achieved temperatures, though this is not required to interpret the present data.

Comparing free-standing samples (e.g., SS2, Sec. V B) to those in a DAC (e.g., D1, Sec. V E), we see shorter emission timescales for the freestanding foil, i.e., the time for the emission intensity to drop to zero after initial irradiation is shorter. The longer emission for confined compared to freestanding foil is somewhat unexpected as the additional heat sink of the highly thermally conductive diamonds around the confined sample should lead to it cooling relatively faster. This may be related to rapid damage processes in the unconfined case [Fig. 14(d)].

E. Finite element modeling implications

In some cases, FEA closely predict the observed SOP temperatures (Fig. 25). This is not unexpected for the freestanding Ta foil [Fig. 25(a)] since the nominal beamline transmission (30%) was calibrated to ablation damage data on Ta foil during the same experiments,[39] however, this still shows the consistency of the independent SOP measurement of temperature with model predictions.[62] Similarly, a completely independent experiment on olivine [Fig. 25(c)], which reaches only modest temperatures, is closely predicted (considering that emission likely emerges from the full volume of the sample in this case). For high-Z foils in the DAC [Figs. 25(b) and 25(d)], significantly lower radiation absorption than expected must be assumed in order to reproduce the observed temperatures, and in some cases other parameters, e.g., thermal conductivity, also require adjustment, including outside their plausible range (Table IV).

These simulations have a range of immediate implications for use of SOP techniques in XFEL experiments, especially where x-ray heating occurs as a result of XFEL irradiation:

1. With high time resolution and small numbers of pulses, individual pulse heating (and cooling) events are observed [Figs. 25(a)

and 25(b)]; lower time resolution and larger numbers of pulses cause events to smear into a continuum in SOP, with models able to extract underlying variations [Fig. 25(c)]
2. High temperatures beyond ~0.5 eV (~6000 K) are rarely detected in SOP in x-ray heating, even when strongly expected on the basis of x-ray power. This implies an effective limit on observed temperatures, though the cause is not clear (discussed below).
3. Average temperature in the bulk detected by x-ray probes (i.e., T_X in Fig. 25) can differ substantially from that observed in SOP, with a range of possible reasons, including:
   (a) X-ray probes average over the temperature gradient in the bulk, whereas SOP is usually measured on a surface (in opaque samples) and dominated by peak temperature (due to weighting by the $\sim T^4$ scaling of emission intensity).
   (b) X-ray probe temperature will correspond to conditions just before each pulse whereas SOP at similar time is dominated by the elevated temperature just after the pulse.
   (c) X-ray probe temperature may be susceptible to phase change, for example, if determined from XRD using volume expansion in a crystal, a maximum volume will be observed near temperature-dependent phase transitions (such as melting) even though temperature continues to rise in SOP.

   Consequently, where XH is significant, comparisons of x-ray probe data and SOP require a careful consideration of both time and space dependence of the temperature in the sample and the specific sensitivities of each measurement.

An interesting case study is that of Olivine [Fig. 25(c)]. Even here, where individual pulse heating is small and heating is gradual, the difference in x-ray probe temperature and emission temperature can be significant, due to the continued presence of lateral gradients resulting from pump and probe of identical size. In detail, hotspot peak temperatures on the beam axis dominate the SOP data, whereas these temperatures contribute little to the volumetric average represented by x-ray probes.

F. Temperature of laser heated samples

We observe that the temperature of the sample in DACs DESY1 (Fig. 13) and XFEL1 (Fig. 20) using LH only follows the generally expected thermal evolution from prior studies. In this case, the peak in temperature coincides closely with the laser pulse and peak in emission intensity, though higher time resolution shows more detail in the temperature evolution (Fig. 13). Both the emission intensity and fitted sample temperature fall off after the laser pulse as expected. The spectral shape of emission also clearly demonstrates a gray-body distribution with respect to changing temperatures. Both of these validate the use of this SOP setup as a reliable temperature diagnostic for laser-heated samples.

G. Relationship between emission intensity and temperature

Temperature and emission intensity are observed to have limited correlation in these experiments. That is, emission intensity is not a direct, quantitative proxy for temperature. Though qualitative trends of emission intensity increasing with temperature are observed, amplitude often changes irrespective of the temperature within the same experiment. For example, in the case of serially x-ray heated metal in a DAC (Secs. V C and V E, Figs. 15 and 18), peak temperatures, coincident with x-ray pulses, remain roughly constant with increasing time but corresponding emission intensity increases. Similarly, in the case of optical heating, temperature initially decreases as emission intensity rises at the beginning of the optical laser pulse (Sec. V A and Fig. 13).

A variety of factors can contribute to the emission intensity trends in the SOP images. Variations in the emitting surface area size and temperature gradient significantly controls the emission. For example, Fig. 27 compares emission intensity observed experimentally and predicted from FEM modeling, during 4-pulse irradiation of Ta foil in MgO and Ne in DAC D1, shot 845 [see Figs. 18 and 25(b)]. Consistent with the observations, the first pulse exhibits very weak emission [Fig. 27(a)], and temperature is predicted to fall below the detection limit [Fig. 27(b)]. The next 3 pulses show similar peak temperatures [Fig. 27(a)] and radial temperature distributions [Fig. 27(b)], however, even small changes in the radial temperature distribution are seen to dramatically affect the emission amplitude. The results show that the dramatic rise in emission intensity is due to the heated area becoming wider with time, regardless of peak temperature.

Thus, where emission intensity is generally increasing with time, often without a clear corresponding increase in peak temperature, as in the above examples, it can often be attributed to changes in heated area size and gradients. A continuous broadening of the x-ray laser heated spot with time as heat conducts from the focal point laterally[31] and inconsistent pointing within pulse trains[39] can both lead to larger hot areas at later time. For example, in Fig. 27(b), the FWHM of the radial temperature gradient broadens, just due to conduction processes, from 6.7 μm at the time of the first pulse to 8.6 μm at the time of the fourth pulse, corresponding to the significant increase in total emission.

Other factors may also play a role in emission amplitude, and its relationship to measured temperature. Changes in target optical properties with temperature or time may become significant, such as where target emissivity may increase due to onset of conductivity in pressure media at high temperature, or where optical properties change as a function of time due to phase transformation or reaction kinetics.[11,38,75] Instrument performance can also play a role, including by smearing due to the point spread function or integration of multiple sweeps, or pincushion sensitivity variations. Finally, fluorescence contributions can lead to deviations from true thermal emission intensity particularly where temperatures and/or thermal emission signal is low, in many cases expressing as apparently blue (and, therefore, hot) emission spectra despite low signal.

Comparing x-ray and laser heating, differing sizes of heated areas correlate to differences in emission intensity, with x-ray experiments with tighter focused radiation generally showing lower emission amplitudes for comparable temperatures. When combined together, the broad laser heated spots at one time in an experiment is in contrast to smaller hotspots maintained by the x-ray pulse train at other times (Sec. V H, Fig. 23), and consequently, emission intensity varies irrespective of temperature.

One consequence of these observations is that a constant emissivity approach to fitting the time domain temperature data,

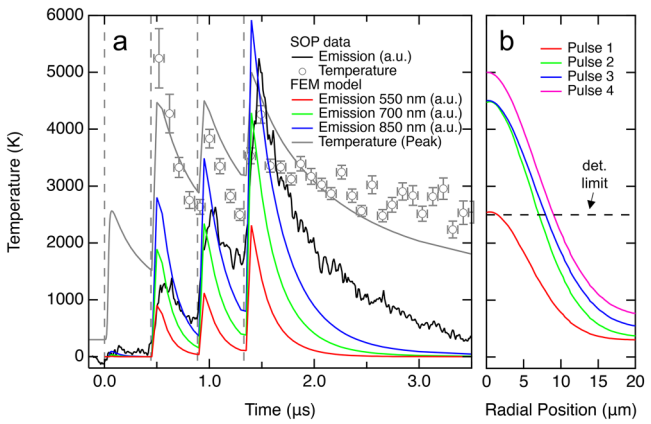

FIG. 27. Emission intensity behavior observed in Shot 845 (sample D1, Fig. 18) together with finite element model results. (a) Experimental data compared to finite element model, with emission intensity in arbitrary units. Observed emission intensity is averaged over the wavelength range 575–775 nm. Predicted intensities in FEM are the total intensity at 550, 700, and 850 nm, integrated over the metal foil surface (units of calculation are $W\,sr^{-1}\,Hz^{-1}$). (b) Radial temperature gradient on the observed (upstream) metal foil surface just after each x-ray pulse. Dashed line shows approximate detection limit. Emission intensity is calculated in the FEM model by integrating the Planck function over this surface.

which can reduce fitting error,[67] is not generally applicable in these experiments. Similarly, an intensity-based measure of temperature, as is commonly used in SOP systems for shock wave experiments[51] is not easily used in experiments of the current type.

H. Maximum temperatures achieved

Potentially very high temperatures are achievable with either pulsed laser or x-ray heating in these experiments.[11,29,31] Laser heating observations are consistent with prior expectations and experience from standard laser heating experiments, with temperatures not much beyond the melting point for unconfined foil, and significantly higher (in the eV or 11604 K range) when pulsed heating confined foils.[11] Values in the range of 3000–6000 K are common in even continuous laser heating of confined foils. X-ray heating shows more unexpected behavior. For the x-ray energies available at the beamline and the high absorbances of some samples studied (e.g., Ta and Au), very high temperatures should be achievable in these samples, in the multi-eV range.[29,31] However, rarely did temperatures produced by x-ray heating and detected pyrometrically reach high values beyond ~5000–6000 K. This is comparable or even less than the typical maximum temperatures achieved by continuous laser heating of DAC samples and well below those seen in pulsed laser heating, including using this same experimental setup.

Temperatures in freestanding XH foils were also larger than those seen in the DAC under x-ray heating. For example, in freestanding Ta, values up to ~6000 K were observed in a single exposure at 50% power equivalent to 25 μJ/pulse (Fig. 14). The required beamline transmission to the sample in this case was ~30% (Table IV), which was validated using an energy scan over the full range of energy using ablation as a diagnostic of temperature.[39,62] However, for Ta in a DAC, at even higher power levels (100%, 137 μJ/pulse), thermal emission was not detectable in a single shot at all, and even the cumulative heating provided by a series of pulses did not achieve the same temperature as a single pulse on a free-standing foil (Fig. 18). The effective beam line transmission to the target needed to explain this data is roughly an order of magnitude smaller than in the freestanding foil case (Table IV) and below any plausible real value for the transmission.

There could be a variety of reasons for these observations. This effect may be partly due to cumulative and *in situ* damage to these samples, occurring at high temperatures when samples are melted over large regions and subjected to large thermal and hydrodynamic stresses. Such localized damage is frequently observed in postmortem observations on high-Z samples.[29] It should also be noted that optically, it is difficult to observe very high temperatures in DAC experiments due to onset of opacity in transparent materials at high pressure and temperature;[9,11,78] in fact, screening of thermal radiation by hot but optically opaque pressure media[9,11] could be even more severe for x-ray heating due to embedding of directly heated layers within indirectly heated media. Relevant scenarios include heating of metallic layers cumulatively with efficient quenching at the metal surface, allowing very high temperature within the metal interior but undetectable temperature on the surface (with corresponding irregularities between x-ray and SOP temperature probing). Other effects that can increasingly act to reduce heating at higher temperature include increasing contributions of electronic heat capacity[29] and decompression cooling of isochorically heated states.[31] Rapid dissipation of heat on sub-ns timescales, such as by fast electron dynamics, could also limit observed temperatures. Still, temperatures of interest, e.g., near high pressure melting points, are readily obtained using XH methods especially when cumulative heating is employed.

I. Combining x-ray probing and other excitations

A key factor for planning XFEL experiments using separate excitations, such as optical lasers, is the extent to which the XFEL itself may affect sample state and observations. A single or serial pulse train could lead to perturbations in detected temperatures in SOP (Fig. 23). Meanwhile, temperatures detected by x-ray probes may deviate from those achieved through separate excitation alone, if preceding probe pulses in a pulse train have altered the local temperatures via residual heat. Such x-ray heating can have obvious (Fig. 23) or subtle (Fig. 22) effects on SOP data, hence, the role of x-ray heating in measurements using other excitation may not be easily assessed from SOP alone. One possibility is that probed spots may be much smaller than the excited area, with any local heating having a small impact on total emission signal but a critical impact on x-ray pulse train observations. Another is that significant heating is possible below the detection limit of SOP. While heating can be mitigated by reducing the XFEL fluence or using samples of low absorption, our data show that considerable heating remains possible in such scenarios. Alternatively, many experiments can be

conducted in a fashion such that the conditions following the XFEL probe are not of interest.

VIII. CONCLUSION

In this work, we have optically measured high temperature states induced by x-ray and optical laser pulses in condensed matter targets at a free electron laser facility. Dynamic temperatures in the range of 1000 to 10 000 K, with time resolutions in the range of tens to hundreds of nanoseconds are studied. These results match expectations of sample heating and temperature evolution calculated by numerical models, with forward modeling of temperature by finite element analysis able to accurately predict the measured total temperature evolution in certain scenarios.

Spectrally- and time-resolved optical emission is measured using a spectrometer mounted on a streak camera coupled with an optical microscope equipped with a confocal spatial filter to isolate a 50 μm diameter area on target and exclude signal away from the focal plane. XFEL irradiation comprised of 17.8 keV, 20-fs XFEL pulses in single shot or MHz pulse trains (443 ns repetition rate), while the optical laser was NIR (1070 nm) with a pulse length of 250 ns. These are focused to spots of $\sim$10 μm diameter on targets. The time-dependent thermal emission spectra are least squares fitted to the Planck function, with the time integration bins, the temporal point spread function and selected streak window affecting the time resolution of the temperature measurement. Uncertainty is evaluated from robust checking of goodness-of-fit parameters against statistical uncertainties in reference-temperature spectrograms.

We study a suite of representative targets including freestanding foils and multi-layer targets in the form of a diamond anvil cell used to contain heated samples and apply high pressures (GPa) prior to irradiation. Measured temperature is dominated by the peak temperature in the field of view, whereas emission intensity has a more complex development accurately predicted by numerical modeling of dynamic temperature gradients (Fig. 27). Where dielectric-bearing targets are irradiated by the XFEL (e.g., diamond anvil cells), background emission due to sample fluorescence is often detected. Thermal and fluorescent signals have distinct spectral–temporal appearance, and when similar in amplitude, fluorescence can perturb temperature measurements. Fluorescence appears at lower powers than required to produce a detectable thermal signal, such that data where only fluorescence is recorded can be used to interpret and model fluorescence behavior for a particular target and extract the thermal component of emission before sample temperature is analyzed. Fluorescence contributions are mitigated through spatial filtering and use of low fluorescence materials (e.g., type II rather than type I diamond). For optical laser heating, results broadly follow previous work using streak optical pyrometry methods.

The spectral SOP discussed here has potentially broad applications for time-resolved measurements of temperature and other optical signals at European XFEL and similar facilities. In the current sample environment configuration at EuXFEL, it is compatible with a range of x-ray and optical laser experiments. Modification of the sample imaging optics (e.g., for different targets, environments and measurements) can allow compatibility with a wider range of experiments. For example, SOP is well demonstrated in conjunction with shock wave compression, and the streak camera range (0.5 ns to 1 ms) covers what is typically required for shock wave techniques. The spectral SOP is particularly useful for lower temperature ranges (<10 000 K) where the emission wavelength dependence varies strongly with temperature. Other optical spectroscopic applications shown possible here include fluorescence spectroscopy, relaxation time studies, and pressure measurements.

ACKNOWLEDGMENTS

We thank H. Sinn for experimental assistance and T. Tschentscher and S. Pascarelli for fruitful discussions. We acknowledge European XFEL in Schenefeld, Germany, for provision of X-ray free-electron laser beamtime at Scientific Instrument HED (High Energy Density Science) and would like to thank the staff for their assistance. The authors are indebted to the Helmholtz International Beamline for Extreme Fields (HIBEF) user consortium for the provision of instrumentation and staff that enabled this experiment. We acknowledge DESY (Hamburg, Germany), a member of the Helmholtz Association HGF, for the provision of experimental facilities. Parts of this research were carried out at PETRA III (beamline P02.2) through proposal I-20190367 EC. The research leading to this result has been supported by the project CALIPSOplus under the Grant Agreement No. 730872 from the EU Framework Program for Research and Innovation HORIZON 2020. Part of this work was performed under the auspices of the U.S. Department of Energy by Lawrence Livermore National Laboratory under Contract No. DE-AC52-07NA27344 and by the U.S. Department of Energy through the Los Alamos National Laboratory, operated by Triad National Security, LLC, for the National Nuclear Security Administration (Contract No. 89233218CNA000001). The research presented in this article was supported by the by the Department of Energy, Laboratory Directed Research and Development program at Los Alamos National Laboratory under Project No. 20190643DR and at SLAC National Accelerator Laboratory under Contract No. DE-AC02-76SF00515. Support is acknowledged from the Panofsky Fellowship at SLAC (E.E.M.); the DOE Office of Fusion Energy Science Funding No. FWP100182 (M.F. and E.E.M.); RCUK-EPSRC Grant Nos. EP/P024513/1 (R.S.M.) and EP/R02927X/1 (E.J.P. and M.I.M.); the European Research Council (ERC) under the European Union's Horizon 2020 research and innovation Programme for Grant Agreement Nos. 670787 (G.F., M.A.B., and G.M.), 864877 (H.M.), and 101002868 (R.S.M.); the National Science Foundation Nos. EAR-1634415 (V.B.P. and GeoSoilEnviroCARS) and DMR-2200670 (A.F.G); and the Leader Researcher program (No. NRF-2018R1A3B1052042) of the Korean Ministry of Science and ICT (MSIT) (Y.L. and H.H.). K.A., K.G., R.J.H., Z.K., H.P.L., and R.R. thank the DFG for support within the Research Unit FOR 2440. Z.K. and C.P. acknowledge support from the DFG Project No. KO-5262/1. S.M. and J.C. acknowledge support from the MetalCore project, supported by the French government through the Programme Investissement d'Avenir (I-SITE ULNE/ ANR-16-IDEX-0004 ULNE) managed by the Agence Nationale de la Recherche. O.B.B. acknowledges the support of the Scottish

Doctoral Training Program in Condensed Matter Physics (CM-CDT). J.D.M. acknowledges support from EPSRC and AWE CASE studentships, UK Ministry of Defence ©Crown Owned Copyright 2022/AWE. A.F.G. and E.E.M. acknowledge the support of Carnegie Science.

AUTHOR DECLARATIONS

Conflict of Interest

The authors have no conflicts to disclose.

Author Contributions

O. B. Ball: Data curation (equal); Formal analysis (equal); Investigation (equal); Methodology (equal); Software (equal); Writing – original draft (equal); Writing – review & editing (equal). **C. Prescher:** Conceptualization (equal); Data curation (equal); Formal analysis (equal); Methodology (equal); Writing – review & editing (equal). **K. Appel:** Data curation (equal); Writing – review & editing (equal). **C. Baehtz:** Data curation (equal). **M. A. Baron:** Data curation (equal). **R. Briggs:** Data curation (equal); Writing – review & editing (equal). **V. Cerantola:** Data curation (equal). **J. Chantel:** Data curation (equal). **S. Chariton:** Data curation (equal). **A. L. Coleman:** Data curation (equal). **H. Cynn:** Data curation (equal). **H. Damker:** Conceptualization (equal); Data curation (equal). **D. Dattelbaum:** Data curation (equal). **L. E. Dresselhaus-Marais:** Data curation (equal). **J. H. Eggert:** Data curation (equal). **L. Ehm:** Data curation (equal). **W. J. Evans:** Data curation (equal). **G. Fiquet:** Data curation (equal). **M. Frost:** Data curation (equal). **K. Glazyrin:** Data curation (equal); Writing – review & editing (equal). **A. F. Goncharov:** Data curation (equal); Writing – review & editing (equal). **R. J. Husband:** Data curation (equal); Writing – review & editing (equal). **H. Hwang:** Data curation (equal). **N. Jaisle:** Data curation (equal). **Zs. Jenei:** Data curation (equal); Writing – review & editing (equal). **J.-Y. Kim:** Data curation (equal); Writing – review & editing (equal). **Y. Lee:** Data curation (equal); Writing – review & editing (equal). **H. P. Liermann:** Data curation (equal); Writing – review & editing (equal). **J. Mainberger:** Data curation (equal). **M. Makita:** Data curation (equal). **H. Marquardt:** Data curation (equal). **E. E. McBride:** Data curation (equal). **J. D. McHardy:** Data curation (equal). **M. I. McMahon:** Data curation (equal). **S. Merkel:** Data curation (equal). **G. Morard:** Data curation (equal). **O'Bannon E. F. III:** Data curation (equal). **C. Otzen:** Data curation (equal). **E. J. Pace:** Data curation (equal). **A. Pelka:** Data curation (equal). **Pépin C. M.:** Data curation (equal). **J. S. Pigott:** Data curation (equal). **C. Plückthun:** Data curation (equal). **V. B. Prakapenka:** Data curation (equal). **R. Redmer:** Data curation (equal); Writing – review & editing (equal). **S. Speziale:** Data curation (equal); Writing – review & editing (equal). **G. Spiekermann:** Data curation (equal). **C. Strohm:** Data curation (equal); Project administration (equal). **B. T. Sturtevant:** Data curation (equal). **P. Talkovski:** Conceptualization (equal); Data curation (equal). **L. Wollenweber:** Conceptualization (equal); Data curation (equal). **U. Zastrau:** Data curation (equal); Project administration (equal). **R. S. McWilliams:** Conceptualization (equal); Data curation (equal); Formal analysis (equal); Methodology (equal); Project administration (equal); Supervision (equal); Writing – original draft (equal); Writing – review & editing (equal). **Z. Konôpková:** Conceptualization (equal); Data curation (equal); Methodology (equal); Supervision (equal); Writing – original draft (equal); Writing – review & editing (equal).

DATA AVAILABILITY

The data that support the findings of this study are openly available in the data management portal for European XFEL (myMdC) at https://in.xfel.eu/metadata/doi/10.22003/XFEL.EU-DATA-002292-00, Ref. 59. Raw data were generated at European XFEL. Derived data supporting the findings of this study are available from the corresponding author upon reasonable request.

REFERENCES

[1]T. Duffy, N. Madhusudhan, and K. Lee, "Mineralogy of super-earth planets," in *Treatise on Geophysics* (Elsevier, 2015), pp. 149–178.
[2]T. Guillot, "Interiors of giant planets inside and outside the solar system," Science (Am. Assoc. Adv. Sci.) **286**, 72–77 (1999).
[3]J. D. Lindl, P. Amendt, R. L. Berger, S. G. Glendinning, S. H. Glenzer, S. W. Haan, R. L. Kauffman, O. L. Landen, and L. J. Suter, "The physics basis for ignition using indirect-drive targets on the national ignition facility," Phys. Plasmas **11**, 339–491 (2004).
[4]F. Graziani, M. P. Desjarlais, R. Redmer, and S. B. Trickey, "Frontiers and challenges in warm dense matter," in *Lecture Notes in Computational Science and Engineering* (Springer International Publishing AG, Cham, 2014), Vol. 96.
[5]B. Militzer, F. González-Cataldo, S. Zhang, K. P. Driver, and F. Soubiran, "First-principles equation of state database for warm dense matter computation," Phys. Rev. E **103**, 013203 (2021).
[6]M. Bethkenhagen, B. B. L. Witte, M. Schörner, G. Röpke, T. Döppner, D. Kraus, S. H. Glenzer, P. A. Sterne, and R. Redmer, "Carbon ionization at gigabar pressures: An ab initio perspective on astrophysical high-density plasmas," Phys. Rev. Res. **2**, 023260 (2020).
[7]G. Weck, V. Recoules, J.-A. Queyroux, F. Datchi, J. Bouchet, S. Ninet, G. Garbarino, M. Mezouar, and P. Loubeyre, "Determination of the melting curve of gold up to 110 GPa," Phys. Rev. B **101**, 014106 (2020).
[8]Z. Du, G. Amulele, L. R. Benedetti, and K. K. M. Lee, "Mapping temperatures and temperature gradients during flash heating in a diamond-anvil cell," Rev. Sci. Instrum. **84**, 075111 (2013).
[9]A. Dewaele, M. Mezouar, N. Guignot, and P. Loubeyre, "High melting points of tantalum in a laser-heated diamond anvil cell," Phys. Rev. Lett. **104**, 255701 (2010).
[10]S. Petitgirard, A. Salamat, P. Beck, G. Weck, and P. Bouvier, "Strategies for in situ laser heating in the diamond anvil cell at an X-ray diffraction beamline," J. Synchrotron Radiat. **21**, 89–96 (2014).
[11]R. S. McWilliams, D. A. Dalton, Z. Konôpková, M. F. Mahmood, and A. F. Goncharov, "Opacity and conductivity measurements in noble gases at conditions of planetary and stellar interiors," Proc. Natl. Acad. Sci. U.S.A. **112**, 7925–7930 (2015).
[12]S. Anzellini, A. Dewaele, M. Mezouar, P. Loubeyre, and G. Morard, "Melting of iron at Earth's inner core boundary based on fast X-ray diffraction," Science **340**, 464 (2013).
[13]Z. Konôpková, R. S. McWilliams, N. Gómez-Pérez, and A. F. Goncharov, "Direct measurement of thermal conductivity in solid iron at planetary core conditions," Nature **534**, 99–101 (2016).
[14]G. Morard, S. Boccato, A. D. Rosa, S. Anzellini, F. Miozzi, L. Henry, G. Garbarino, M. Mezouar, M. Harmand, F. Guyot, E. Boulard, I. Kantor, T. Irifune, and R. Torchio, "Solving controversies on the iron phase diagram under high pressure," Geophys. Res. Lett. **45**, 11,074, https://doi.org/10.1029/2018GL079950 (2018).

[15]S. Boccato, R. Torchio, I. Kantor, G. Morard, S. Anzellini, R. Giampaoli, R. Briggs, A. Smareglia, T. Irifune, and S. Pascarelli, "The melting curve of nickel up to 100 GPa explored by XAS," J. Geophys. Res.: Solid Earth **122**, 9921–9930, https://doi.org/10.1002/2017JB014807 (2017).
[16]S. Boccato, R. Torchio, P. D'Angelo, A. Trapananti, I. Kantor, V. Recoules, S. Anzellini, G. Morard, T. Irifune, and S. Pascarelli, "Compression of liquid Ni and Co under extreme conditions explored by X-ray absorption spectroscopy," Phys. Rev. B **100**, 180101 (2019).
[17]A. Lévy, P. Audebert, R. Shepherd, J. Dunn, M. Cammarata, O. Ciricosta, F. Deneuville, F. Dorchies, M. Fajardo, C. Fourment, D. Fritz, J. Fuchs, J. Gaudin, M. Gauthier, A. Graf, H. J. Lee, H. Lemke, B. Nagler, J. Park, O. Peyrusse, A. B. Steel, S. M. Vinko, J. S. Wark, G. O. Williams, D. Zhu, and R. W. Lee, "The creation of large-volume, gradient-free warm dense matter with an X-ray free-electron laser," Phys. Plasmas **22**, 030703 (2015).
[18]H.-P. Liermann, Z. Konôpková, W. Morgenroth, K. Glazyrin, J. Bednarčik, E. E. McBride, S. Petitgirard, J. T. Delitz, M. Wendt, Y. Bican, A. Ehnes, I. Schwark, A. Rothkirch, M. Tischer, J. Heuer, H. Schulte-Schrepping, T. Kracht, and H. Franz, "The extreme conditions beamline P02.2 and the extreme conditions science infrastructure at PETRA III," J. Synchrotron Radiat. **22**, 908–924 (2015).
[19]B. Nagler, U. Zastrau, R. R. Fäustlin, S. M. Vinko, T. Whitcher, A. J. Nelson, R. Sobierajski, J. Krzywinski, J. Chalupsky, E. Abreu, S. Bajt, T. Bornath, T. Burian, H. Chapman, J. Cihelka, T. Döppner, S. Düsterer, T. Dzelzainis, M. Fajardo, E. Förster, C. Fortmann, E. Galtier, S. H. Glenzer, S. Göde, G. Gregori, V. Hajkova, P. Heimann, L. Juha, M. Jurek, F. Y. Khattak, A. R. Khorsand, D. Klinger, M. Kozlova, T. Laarmann, H. J. Lee, R. W. Lee, K.-H. Meiwes-Broer, P. Mercere, W. J. Murphy, A. Przystawik, R. Redmer, H. Reinholz, D. Riley, G. Röpke, F. Rosmej, K. Saksl, R. Schott, R. Thiele, J. Tiggesbäumker, S. Toleikis, T. Tschentscher, I. Uschmann, H. J. Vollmer, and J. S. Wark, "Turning solid aluminium transparent by intense soft X-ray photoionization," Nat. Phys. **5**, 693–696 (2009).
[20]U. Zastrau, C. Fortmann, R. R. Fäustlin, L. F. Cao, T. Döppner, S. Düsterer, S. H. Glenzer, G. Gregori, T. Laarmann, H. J. Lee, A. Przystawik, P. Radcliffe, H. Reinholz, G. Röpke, R. Thiele, J. Tiggesbäumker, N. X. Truong, S. Toleikis, I. Uschmann, A. Wierling, T. Tschentscher, E. Förster, and R. Redmer, "Bremsstrahlung and line spectroscopy of warm dense aluminum plasma heated by XUV free-electron-laser radiation," Phys. Rev. E **78**, 066406 (2008).
[21]U. Zastrau, P. Sperling, A. Becker, T. Bornath, R. Bredow, T. Döppner, S. Dziarzhytski, T. Fennel, L. B. Fletcher, E. Förster, C. Fortmann, S. H. Glenzer, S. Göde, G. Gregori, M. Harmand, V. Hilbert, B. Holst, T. Laarmann, H. J. Lee, T. Ma, J. P. Mithen, R. Mitzner, C. D. Murphy, M. Nakatsutsumi, P. Neumayer, A. Przystawik, S. Roling, M. Schulz, B. Siemer, S. Skruszewicz, J. Tiggesbäumker, S. Toleikis, T. Tschentscher, T. White, M. Wöstmann, H. Zacharias, and R. Redmer, "Equilibration dynamics and conductivity of warm dense hydrogen," Phys. Rev. E **90**, 013104 (2014).
[22]M. B. Boslough and T. J. Ahrens, "A sensitive time-resolved radiation pyrometer for shock-temperature measurements above 1500 K," Rev. Sci. Instrum. **60**, 3711–3716 (1989).
[23]K. K. M. Lee, L. R. Benedetti, R. Jeanloz, P. M. Celliers, J. H. Eggert, D. G. Hicks, S. J. Moon, A. Mackinnon, L. B. D. Silva, D. K. Bradley, W. Unites, G. W. Collins, E. Henry, M. Koenig, A. Benuzzi-Mounaix, J. Pasley, and D. Neely, "Laser-driven shock experiments on precompressed water: Implications for 'icy' giant planets," J. Chem. Phys. **125**, 014701 (2006).
[24]C. Dai, J. Hu, and H. Tan, "Hugoniot temperatures and melting of tantalum under shock compression determined by optical pyrometry," J. Appl. Phys. **106**, 043519 (2009).
[25]S. B. Kormer, "Optical study of the characteristics of shock-compressed condensed dielectrics," Sov. Phys. Usp. **11**, 229–254 (1968).
[26]R. Jeanloz, P. M. Celliers, G. W. Collins, J. H. Eggert, K. K. M. Lee, R. S. McWilliams, S. Brygoo, and P. Loubeyre, "Achieving high-density states through shock-wave loading of precompressed samples," Proc. Natl. Acad. Sci. U.S.A. **104**, 9172–9177 (2007).
[27]H. Cynn and C.-S. Yoo, "Equation of state of tantalum to 174 GPa," Phys. Rev. B **59**, 8526–8529 (1999).
[28]V. Prakapenka, G. Shen, and L. Dubrovinsky, "Carbon transport in diamond anvil cells," High Temp.-High Press. **35/36**, 237–249 (2003).
[29]R. J. Husband, R. S. McWilliams, E. J. Pace, A. L. Coleman, H. Hwang, J. Choi, T. Kim, G. C. Hwang, O. B. Ball, S. H. Chun, D. Nam, S. Kim, H. Cynn, V. B. Prakapenka, S.-H. Shim, S. Toleikis, M. I. McMahon, Y. Lee, and H.-P. Liermann, "X-ray free electron laser heating of water and gold at high static pressure," Commun. Mater. **2**, 61 (2021).
[30]Z. Jenei, H. P. Liermann, R. Husband, A. S. J. Méndez, D. Pennicard, H. Marquardt, E. F. O'Bannon, A. Pakhomova, Z. Konôpková, K. Glazyrin, M. Wendt, S. Wenz, E. E. McBride, W. Morgenroth, B. Winkler, A. Rothkirch, M. Hanfland, and W. J. Evans, "New dynamic diamond anvil cells for tera-pascal per second fast compression X-ray diffraction experiments," Rev. Sci. Instrum. **90**, 065114 (2019).
[31]J. Meza-Galvez, N. Gómez-Pérez, A. S. Marshall, A. L. Coleman, K. Appel, H. P. Liermann, M. I. McMahon, Z. Konôpková, and R. S. McWilliams, "Thermomechanical response of thickly tamped targets and diamond anvil cells under pulsed hard X-ray irradiation," J. Appl. Phys. **127**, 195902 (2020).
[32]W. Decking, S. Abeghyan, P. Abramian, A. Abramsky, A. Aguirre, C. Albrecht, P. Alou, M. Altarelli, P. Altmann, K. Amyan, V. Anashin, E. Apostolov, K. Appel, D. Auguste, V. Ayvazyan, S. Baark, F. Babies, N. Baboi, P. Bak, V. Balandin, R. Baldinger, B. Baranasic, S. Barbanotti, O. Belikov, V. Belokurov, L. Belova, V. Belyakov, S. Berry, M. Bertucci, B. Beutner, A. Block, M. Blöcher, T. Böckmann, C. Bohm, M. Böhnert, V. Bondar, E. Bondarchuk, M. Bonezzi, P. Borowiec, C. Bösch, U. Bösenberg, A. Bosotti, R. Böspflug, M. Bousonville, E. Boyd, Y. Bozhko, A. Brand, J. Branlard, S. Briechle, F. Brinker, S. Brinker, R. Brinkmann, S. Brockhauser, O. Brovko, H. Brück, A. Brüdgam, L. Butkowski, T. Büttner, J. Calero, E. Castro-Carballo, G. Cattalanotto, J. Charrier, J. Chen, A. Cherepenko, V. Cheskidov, M. Chiodini, A. Chong, S. Choroba, M. Chorowski, D. Churanov, W. Cichalewski, M. Clausen, W. Clement, C. Cloué, J. A. Cobos, N. Coppola, S. Cunis, K. Czuba, M. Czwalinna, B. D'Almagne, J. Dammann, H. Danared, A. de Zubiaurre Wagner, A. Delfs, T. Delfs, F. Dietrich, T. Dietrich, M. Dohlus, M. Dommach, A. Donat, X. Dong, N. Doynikov, M. Dressel, M. Duda, P. Duda, H. Eckoldt, W. Ehsan, J. Eidam, F. Eints, C. Engling *et al.*, "A MHz-repetition-rate hard X-ray free-electron laser driven by a superconducting linear accelerator," Nat. Photonics **14**, 391–397 (2020).
[33]J. Grünert, M. P. Carbonell, F. Dietrich, T. Falk, W. Freund, A. Koch, N. Kujala, J. Laksman, J. Liu, T. Maltezopoulos, K. Tiedtke, U. F. Jastrow, A. Sorokin, E. Syresin, A. Grebentsov, and O. Brovko, "X-ray photon diagnostics at the European XFEL," J. Synchrotron Radiat. **26**, 1422–1431 (2019).
[34]M. Ishino, N. Hasegawa, M. Nishikino, T. Pikuz, I. Skobelev, A. Faenov, N. Inogamov, T. Kawachi, and M. Yamagiwa, "Very low electron temperature in warm dense matter formed by focused picosecond soft X-ray laser pulses," J. Appl. Phys. **116**, 183302 (2014).
[35]E. Principi, C. Ferrante, A. Filipponi, F. Bencivenga, F. D'Amico, C. Masciovecchio, and A. D. Cicco, "A method for estimating the temperature in high energy density free electron laser experiments," Nucl. Instrum. Methods Phys. Res. Sect. A: Accel., Spectrom., Detect. Assoc. Equip. **621**, 643–649 (2010).
[36]H. Wallander and J. Wallentin, "Simulated sample heating from a nanofocused X-ray beam," J. Synchrotron Radiat. **24**, 925–933 (2017).
[37]E. J. Pace, A. L. Coleman, R. J. Husband, H. Hwang, J. Choi, T. Kim, G. Hwang, S. H. Chun, D. Nam, S. Kim, O. B. Ball, H.-P. Liermann, M. I. McMahon, Y. Lee, and R. S. McWilliams, "Intense reactivity in sulfur-hydrogen mixtures at high pressure under X-ray irradiation," J. Phys. Chem. Lett. **11**, 1828–1834 (2020).
[38]H. Hwang, T. Kim, H. Cynn, T. Vogt, R. J. Husband, K. Appel, C. Baehtz, O. B. Ball, M. A. Baron, R. Briggs, M. Bykov, E. Bykova, V. Cerantola, J. Chantel, A. L. Coleman, D. Dattlebaum, L. E. Dresselhaus-Marais, J. H. Eggert, L. Ehm, W. J. Evans, G. Fiquet, M. Frost, K. Glazyrin, A. F. Goncharov, Z. Jenei, J. Kim, Z. Konôpková, J. Mainberger, M. Makita, H. Marquardt, E. E. McBride, J. D. McHardy, S. Merkel, G. Morard, E. F. O'Bannon, C. Otzen, E. J. Pace, A. Pelka, C. M. Pépin, J. S. Pigott, V. B. Prakapenka, C. Prescher, R. Redmer, S. Speziale, G. Spiekermann, C. Strohm, B. T. Sturtevant, N. Velisavljevic, M. Wilke, C.-S. Yoo, U. Zastrau, H.-P. Liermann, M. I. McMahon,

R. S. McWilliams, and Y. Lee, "X-ray free electron laser-induced synthesis of ε-iron nitride at high pressures," J. Phys. Chem. Lett. **12**, 3246–3252 (2021).
[39]H. P. Liermann, Z. Konôpková, K. Appel, C. Prescher, A. Schropp, V. Cerantola, R. J. Husband, J. D. McHardy, M. I. McMahon, R. S. McWilliams, C. M. Pépin, J. Mainberger, M. Roeper, A. Berghäuser, H. Damker, P. Talkovski, M. Foese, N. Kujala, O. B. Ball, M. A. Baron, R. Briggs, M. Bykov, E. Bykova, J. Chantel, A. L. Coleman, H. Cynn, D. Dattelbaum, L. E. Dresselhaus-Marais, J. H. Eggert, L. Ehm, W. J. Evans, G. Fiquet, M. Frost, K. Glazyrin, A. F. Goncharov, H. Hwang, Z. Jenei, J.-Y. Kim, F. Langenhorst, Y. Lee, M. Makita, H. Marquardt, E. E. McBride, S. Merkel, G. Morard, E. F. O'Bannon, C. Otzen, E. J. Pace, A. Pelka, J. S. Pigott, V. B. Prakapenka, R. Redmer, C. Sanchez-Valle, M. Schoelmerich, S. Speziale, G. Spiekermann, B. T. Sturtevant, S. Toleikis, N. Velisavljevic, M. Wilke, C.-S. Yoo, C. Baehtz, U. Zastrau, and C. Strohm, "Novel experimental setup for megahertz X-ray diffraction in a diamond anvil cell at the high energy density (HED) instrument of the European X-ray free-electron laser (EuXFEL)," J. Synchrotron Radiat. **28**, 688–706 (2021).
[40]K. R. Beyerlein, H. O. Jönsson, R. Alonso-Mori, A. Aquila, S. Bajt, A. Barty, R. Bean, J. E. Koglin, M. Messerschmidt, D. Ragazzon, D. Sokaras, G. J. Williams, S. Hau-Riege, S. Boutet, H. N. Chapman, N. Timneanu, and C. Caleman, "Ultrafast nonthermal heating of water initiated by an X-ray free-electron laser," Proc. Natl. Acad. Sci. U.S.A. **115**, 5652–5657 (2018).
[41]S. H. Glenzer and R. Redmer, "X-ray Thomson scattering in high energy density plasmas," Rev. Mod. Phys. **81**, 1625–1663 (2009).
[42]A. M. Saunders, A. Jenei, T. Döppner, R. W. Falcone, D. Kraus, A. Kritcher, O. L. Landen, J. Nilsen, and D. Swift, "X-ray Thomson scattering measurements from hohlraum-driven spheres on the OMEGA laser," Rev. Sci. Instrum. **87**, 11E724 (2016).
[43]A. M. Saunders, B. Lahmann, G. Sutcliffe, J. A. Frenje, R. W. Falcone, and T. Döppner, "Characterizing plasma conditions in radiatively heated solid-density samples with X-ray Thomson scattering," Phys. Rev. E **98**, 063206 (2018).
[44]K. Falk, C. L. Fryer, E. J. Gamboa, C. W. Greeff, H. M. Johns, D. W. Schmidt, M. Smíd, J. F. Benage, and D. S. Montgomery, "X-ray Thomson scattering measurement of temperature in warm dense carbon," Plasma Physics and Controlled Fusion **59**(1), 014050 (2016).
[45]L. Fletcher, A. Kritcher, A. Pak, T. Ma, T. Döppner, C. Fortmann, L. Divol, O. Jones, O. Landen, H. Scott, J. Vorberger, D. Chapman, D. Gericke, B. Mattern, G. Seidler, G. Gregori, R. Falcone, and S. Glenzer, "Observations of continuum depression in warm dense matter with X-ray Thomson scattering," Phys. Rev. Lett. **112**, 145004 (2014).
[46]T. Dornheim, M. Böhme, D. Kraus, T. Döppner, T. R. Preston, Z. A. Moldabekov, and J. Vorberger, "Accurate temperature diagnostics for matter under extreme conditions," Nat. Commun. **13**, 7911 (2022).
[47]Z. Konôpková, W. Morgenroth, R. Husband, N. Giordano, A. Pakhomova, O. Gutowski, M. Wendt, K. Glazyrin, A. Ehnes, J. T. Delitz, A. F. Goncharov, V. B. Prakapenka, and H.-P. Liermann, "Laser heating system at the extreme conditions beamline, P02.2, PETRA III," J. Synchrotron Radiat. **28**, 1747–1757 (2021).
[48]P. Ni, M. Kulish, V. Mintsev, D. Nikolaev, V. Ternovoi, D. Hoffmann, S. Udrea, A. Hug, N. Tahir, and D. Varentsov, "Temperature measurement of warm-dense-matter generated by intense heavy-ion beams," Laser Part. Beams **26**, 583–589 (2008).
[49]E. Principi, R. Cucini, A. Filipponi, A. Gessini, F. Bencivenga, F. D'Amico, A. D. Cicco, and C. Masciovecchio, "Determination of the ion temperature in a stainless steel slab exposed to intense ultrashort laser pulses," Phys. Rev. Lett. **109**, 025005 (2012).
[50]A. Barducci and I. Pippi, "Temperature and emissivity retrieval from remotely sensed images using the "Grey body emissivity" method," IEEE Trans. Geosci. Remote Sens. **34**, 681–695 (1996).
[51]J. E. Miller, T. R. Boehly, A. Melchior, D. D. Meyerhofer, P. M. Celliers, J. H. Eggert, D. G. Hicks, C. M. Sorce, J. A. Oertel, and P. M. Emmel, "Streaked optical pyrometer system for laser-driven shock-wave experiments on OMEGA," Rev. Sci. Instrum. **78**, 034903 (2007).
[52]P. D. Asimow, "Melts under extreme conditions from shock experiments," in *Magmas Under Pressure* (Elsevier, 2018), pp. 396–397.
[53]E. Floyd, E. T. Gumbrell, J. Fyrth, J. D. Luis, J. W. Skidmore, S. Patankar, S. Giltrap, and R. Smith, "A high spatio-temporal resolution optical pyrometer at the ORION laser facility," Rev. Sci. Instrum. **87**, 11E546 (2016).
[54]L. R. Benedetti, N. Guignot, and D. L. Farber, "Achieving accuracy in spectror-adiometric measurements of temperature in the laser-heated diamond anvil cell: Diamond is an optical component," J. Appl. Phys. **101**, 013109 (2007).
[55]S. Rekhi, J. Tempere, and I. F. Silvera, "Temperature determination for nano-second pulsed laser heating," Rev. Sci. Instrum. **74**, 3820–3825 (2003).
[56]J. Deng, Z. Du, L. R. Benedetti, and K. K. Lee, "The influence of wavelength-dependent absorption and temperature gradients on temperature determination in laser-heated diamond-anvil cells," J. Appl. Phys. **121**, 025901 (2017).
[57]G. A. Lyzenga and T. J. Ahrens, "Multiwavelength optical pyrometer for shock compression experiments," Rev. Sci. Instrum. **50**, 1421–1424 (1979).
[58]A. Seifter, S. T. Stewart, M. R. Furlanetto, G. B. Kennedy, J. R. Payton, and A. W. Obst, "Post-shock temperature measurements of aluminum," AIP Conference Proceedings **845**(1), 139–142 (2006).
[59]R. S. McWilliams, "Femtosecond hard X-ray studies at high static pressure," EuXFEL Proposal 2292 (2019).
[60]G. Feng, I. Zagorodnov, T. Limberg, H. Jin, Y. Kot, M. Dohlusand, and W. Decking, "Beam Dynamics Simulations for European XFEL," TESLA-FEL Report 2013-04. DESY, Hamburg, Germany (2013).
[61]T. Maltezopoulos, F. Dietrich, W. Freund, U. F. Jastrow, A. Koch, J. Laksman, J. Liu, M. Planas, A. A. Sorokin, K. Tiedtke, and J. Grünert, "Operation of X-ray gas monitors at the European XFEL," J. Synchrotron Radiat. **26**, 1045–1051 (2019).
[62]J. D. McHardy, under review (2023).
[63]V. Cerantola, A. D. Rosa, Z. Konôpková, R. Torchio, E. Brambrink, A. Rack, U. Zastrau, and S. Pascarelli, "New frontiers in extreme conditions science at synchrotrons and free electron lasers," J. Phys.: Condens. Matter **33**, 274003 (2021).
[64]H.-P. Liermann, Z. Konopkova, K. Appel, H.-G. Damker, A. Schropp, R. S. Mcwilliams, A. Goncharov, and C. Beahtz, "Conceptual design report for diamond anvil cell setup (DAC) at the HED instrument of the European XFEL.; 2–5," Tech. Rep. (2016).
[65]M. Nakatsutsumi and T. Tschentscher, "Conceptual design report: Scientific instrument high energy density physics (HED)," (2013).
[66]U. Zastrau, K. Appel, C. Baehtz, O. Baehr, L. Batchelor, A. Berghäuser, M. Banjafar, E. Brambrink, V. Cerantola, T. E. Cowan, H. Damker, S. Dietrich, S. D. D. Cafiso, J. Dreyer, H.-O. Engel, T. Feldmann, S. Findeisen, M. Foese, D. Fulla-Marsa, S. Göde, M. Hassan, J. Hauser, T. Herrmannsdörfer, H. Höppner, J. Kaa, P. Kaever, K. Knöfel, Z. Konôpková, A. L. García, H.-P. Liermann, J. Mainberger, M. Makita, E.-C. Martens, E. E. McBride, D. Möller, M. Nakatsutsumi, A. Pelka, C. Plückthun, C. Prescher, T. R. Preston, M. Röper, A. Schmidt, W. Seidel, J.-P. Schwinkendorf, M. O. Schoelmerich, U. Schramm, A. Schropp, C. Strohm, K. Sukharnikov, P. Talkovski, I. Thorpe, M. Toncian, T. Toncian, L. Wollenweber, S. Yamamoto, and T. Tschentscher, "The high energy density scientific instrument at the European XFEL," J. Synchrotron Radiat. **28**, 1393–1416 (2021).
[67]R. S. McWilliams, Z. Konôpková, and A. F. Goncharov, "A flash heating method for measuring thermal conductivity at high pressure and temperature: Application to Pt," Phys. Earth Planet. Inter. **247**, 17–26 (2015).
[68]W. Haynes, *Handbook of Chemistry and Physics*, 101st Ed., edited by J. R. Rumble (CRC Press, Taylor & Francis Group, Boca Raton, FL, 2020).
[69]K. Minuro, *Test Report for high dynamic streak camera: Model C13410-01A*, Hamamatsu Photonics K.K. (2018).
[70]J. J. Moré, "The Levenberg-Marquardt algorithm: Implementation and theory," in *Numerical Analysis*, edited by G. A. Watson (Springer Berlin Heidelberg, Berlin, Heidelberg, 1978), pp. 105–116.
[71]C. R. Harris, K. J. Millman, S. J. van der Walt, R. Gommers, P. Virtanen, D. Cournapeau, E. Wieser, J. Taylor, S. Berg, N. J. Smith, R. Kern, M. Picus, S. Hoyer, M. H. van Kerkwijk, M. Brett, A. Haldane, J. Fernández del Río, M. Wiebe, P. Peterson, P. Gérard-Marchant, K. Sheppard, T. Reddy, W. Weckesser, H. Abbasi, C. Gohlke, and T. E. Oliphant, "Array programming with NumPy," Nature **585**, 357-362 (2020).

[72]P. Virtanen, R. Gommers, T. E. Oliphant, M. Haberland, T. Reddy, D. Cournapeau, E. Burovski, P. Peterson, W. Weckesser, J. Bright, S. J. van der Walt, M. Brett, J. Wilson, K. J. Millman, N. Mayorov, A. R. J. Nelson, E. Jones, R. Kern, E. Larson, C. J. Carey, İ. Polat, Y. Feng, E. W. Moore, J. VanderPlas, D. Laxalde, J. Perktold, R. Cimrman, I. Henriksen, E. A. Quintero, C. R. Harris, A. M. Archibald, A. H. Ribeiro, F. Pedregosa, and P. van Mulbregt, and SciPy 1.0 Contributors, "SciPy 1.0: Fundamental algorithms for scientific computing in python," Nat. Methods **17**, 261–272 (2020).
[73]J. M. Montgomery, M. J. Lipp, Z. Jenei, Y. Meng, and W. J. Evans, "A simple and portable multi-channel pyrometer allowing temperature measurements down to 800 K on the microsecond scale," Rev. Sci. Instrum. **89**, 125117 (2018).
[74]L. R. Benedetti and P. Loubeyre, "Temperature gradients, wavelength-dependent emissivity, and accuracy of high and very-high temperatures measured in the laser-heated diamond cell," High Pressure Res. **24**, 423–445 (2004).
[75]R. S. McWilliams, D. A. Dalton, M. F. Mahmood, and A. F. Goncharov, "Optical properties of fluid hydrogen at the transition to a conducting state," Phys. Rev. Lett. **116**, 255501 (2016).
[76]P. R. Bevington, *Data Reduction and Error Analysis for the Physical Sciences*, 3rd ed. (McGraw-Hill, New York, 2003).
[77]G. Shen, Y. Wang, A. Dewaele, C. Wu, D. E. Fratanduono, J. Eggert, S. Klotz, K. F. Dziubek, P. Loubeyre, O. V. Fatâyanov, P. D. Asimow, T. Mashimo, and R. M. M. Wentzcovitch, and other members of the IPPS task group, "Toward an international practical pressure scale: A proposal for an IPPS ruby gauge (IPPS-Ruby2020)," High Pressure Res. **40**, 299–314 (2020).
[78]V. B. Prakapenka, N. Holtgrewe, S. S. Lobanov, and A. F. Goncharov, "Structure and properties of two superionic ice phases," Nat. Phys. **17**, 1233–1238 (2021).
[79]L. B. Fletcher, H. J. Lee, B. Barbrel, M. Gauthier, E. Galtier, B. Nagler, T. Döppner, S. LePape, T. Ma, A. Pak, D. Turnbull, T. White, G. Gregori, M. Wei, R. W. Falcone, P. Heimann, U. Zastrau, J. B. Hastings, and S. H. Glenzer, "Exploring Mbar shock conditions and isochorically heated aluminum at the matter in extreme conditions end station of the linac coherent light source (invited)," Rev. Sci. Instrum. **85**, 11E702 (2014).
[80]J. A. Montoya and A. F. Goncharov, "Finite element calculations of the time dependent thermal fluxes in the laser-heated diamond anvil cell," J. Appl. Phys. **111**, 112617 (2012).
[81]I. V. Savchenko and S. V. Stankus, "Thermal conductivity and thermal diffusivity of tantalum in the temperature range from 293 to 1800 K," Thermophys. Aeromechanics **15**, 679–682 (2008).
[82]P. W. Bridgman, "The resistance of 72 elements, alloys and compounds to 100,000 Kg/Cm^2," Proc. Am. Acad. Arts Sci. **81**, 165–251 (1952).
[83]Y. Xu, T. J. Shankland, S. Linhardt, D. C. Rubie, F. Langenhorst, and K. Klasinski, "Thermal diffusivity and conductivity of olivine, wadsleyite and ringwoodite to 20 GPa and 1373 K," Phys. Earth Planet. Inter. **143–144**, 321–336 (2004).
[84]Z. Lin, L. V. Zhigilei, and V. Celli, "Electron-phonon coupling and electron heat capacity of metals under conditions of strong electron-phonon nonequilibrium," Phys. Rev. B **77**, 075133 (2008).
[85]C. Su, Y. Liu, W. Song, D. Fan, Z. Wang, and H. Tang, "Thermodynamic properties of San Carlos olivine at high temperature and high pressure," Acta Geochim. **37**, 171–179 (2018).
[86]A. Dewaele, P. Loubeyre, and M. Mezouar, "Equations of state of six metals above 94 GPa," Phys. Rev. B **70**, 094112 (2004).
[87]W. Liu and B. Li, "Thermal equation of state of $(Mg_{0.9}Fe_{0.1})_2SiO_4$ olivine," Phys. Earth Planet. Inter. **157**, 188–195 (2006).
[88]B. Henke, E. Gullikson, and J. Davis, "X-ray interactions: Photoabsorption, scattering, transmission, and reflection at E = 50–30,000 eV, Z = 1–92," At. Data Nucl. Data Tables **54**, 181–342 (1993).
[89]K. D. Timmerhaus and T. M. Flynn, *Cryogenic Process Engineering* (Springer US, 1989).
[90]A. F. Goncharov, M. Wong, D. A. Dalton, J. G. O. Ojwang, V. V. Struzhkin, Z. Konôpková, and P. Lazor, "Thermal conductivity of argon at high pressures and high temperatures," J. Appl. Phys. **111**, 112609 (2012).
[91]P. Andersson, "Thermal conductivity under pressure and through phase transitions in solid alkali halides. I. Experimental results for KCl, KBr, KI, RbCl, RbBr and RbI," J. Phys. C: Solid State Phys. **18**, 3943 (1985).
[92]S. Stackhouse, L. Stixrude, and B. B. Karki, "Thermal conductivity of periclase (MgO) from first principles," Phys. Rev. Lett. **104**, 208501 (2010).
[93]D. A. Dalton, W.-P. Hsieh, G. T. Hohensee, D. G. Cahill, and A. F. Goncharov, "Effect of mass disorder on the lattice thermal conductivity of MgO periclase under pressure," Sci. Rep. **3**, 2400 (2013).
[94]M. W. Chase and, N. I. S. O. (US), *NIST-JANAF Thermochemical Tables* (American Chemical Society Washington, DC, 1998), Vol. 9.
[95]A. Dewaele, F. Datchi, P. Loubeyre, and M. Mezouar, "High pressure-high temperature equations of state of neon and diamond," Phys. Rev. B **77**, 094106 (2008).
[96]P. I. Dorogokupets and A. Dewaele, "Equations of state of MgO, Au, Pt, NaCl-B1, and NaCl-B2: Internally consistent high-temperature pressure scales," High Pressure Res. **27**, 431–446 (2007).
[97]A. Dewaele, A. B. Belonoshko, G. Garbarino, F. Occelli, P. Bouvier, M. Hanfland, and M. Mezouar, "High-pressure–high-temperature equation of state of KCl and KBr," Phys. Rev. B **85**, 214105 (2012).
[98]Y. Akahama and H. Kawamura, "Diamond anvil Raman gauge in multimegabar pressure range," High Pressure Res. **27**, 473–482 (2007).
[99]J. H. Eggert, K. A. Goettel, and I. F. Silvera, "Elimination of pressure-induced fluorescence in diamond anvils," Appl. Phys. Lett. **53**, 2489–2491 (1988).
[100]M. Moszyński, T. Ludziejewski, D. Wolski, W. Klamra, and L. Norlin, "Properties of the YAG:Ce scintillator," Nucl. Instrum. Methods Phys. Res. Sect. A: Accel., Spectrom., Detect. Assoc. Equip. **345**, 461–467 (1994).
[101]H. K. Mao and R. J. Hemley, "Optical transitions in diamond at ultrahigh pressures," Nature **351**, 721–724 (1991).